Nuclear structure of Cu isotopes studied with collinear laser spectroscopy

Pieter Vingerhoets

Examination committee:
Prof. Dr. Mark Huyse[1], president
Prof. Dr. Gerda Neyens[1], promotor
Prof. Dr. Nathal Severijns [1]
Prof. Dr. Riccardo Raabe [1]
Prof. Dr. Peter Lievens [2]
Prof. Dr. Jonathan Billowes [3]

Dissertation presented in partial fulfillment of the requirements for the degree of Doctor in Science

[1] Instituut voor Kern- en Stralingsfysica, K.U. Leuven, Celestijnenlaan 200D, B-3001 Leuven, Belgium
[2] Laboratorium voor Vaste-Stoffysica en Magnetisme, K.U. Leuven, Celestijnenlaan 200D, B-3001 Leuven, Belgium
[3] School of Physics and Astronomy, The University of Manchester, Manchester, M13 9PL, United Kingdom

March 2011

ISBN number 978-90-8649-404-0
D/2011/10.705/22

Acknowledgements

Wanneer ik terugkijk op de vier jaren van mijn doctoraat, lijken deze te zijn voorbijgevlogen. Voor mij geldt dit als een bewijs dat het niet alleen op wetenschappelijk maar ook op sociaal gebied mooie jaren zijn geweest. Hierbij wil ik enkele mensen uitdrukkelijk bedanken die zowel het eindwerk als de weg ernaartoe extra glans hebben gegeven.

Gerda, eerst en vooral bedankt om me de kans te geven mijn doctoraat te beginnen. Ik heb altijd je eerlijke en open manier van werken geapprecieerd, en bovendien stond je deur altijd open voor vragen of problemen.

I thank the members of the jury Jon Billowes, Mark Huyse, Peter Lievens, Riccardo Raabe and Nathal Severijns for their valuable comments on this thesis work and the enlightening discussion during my first defense.

Kieran, thanks for introducing me to the magical world of laser spectroscopy, and tackling the copper isotope chain together. Also thanks for a hilarious April 1st 2008...

The experimental data discussed in this thesis were measured with the help of many people. The COLLAPS team in CERN, Deyan, Mark, Kim, Christopher, Magda, Rainer, Wilfried, Klaus, Jon, Kieran, Bradley, Dave, Iain, Ernesto, Michael. Thanks for teaching me details about the setup, and the nice atmosphere during the night shifts!

Een ferme dankjewel gaat naar de vele collega's die ervoor zorgden dat ik steeds met plezier naar het IKS vertrok. In het bijzonder de Leuvense kernmomenten groep: Nele, Rady, Deyan, Jasna, Mustafa. En

ook alle andere collega's, dank aan de 'moete' bende voor de gezellige middagpauzes, Dzjelli voor de dagelijkse invasies in ons bureau, en niet te vergeten de vele trouwe klanten van de broodjesdag.

Onze ondertussen ex-masterstudenten hebben me meermaals verrast door als volwaardig teamlid mee te draaien in de groep. Maarten, Wannes, Jeffrey en Quinten, tof dat jullie nog altijd langskomen en veel succes met jullie latere job!

De vijf dames van het secretariaat die de laatste vier jaar mijn leven hebben vereenvoudigd zijn Katia, Josee, Sally, Martine en Isabelle. Bedankt! En ook de computermannen Bert en Luc, altijd paraat en met een leuke babbel erbovenop. Nancy, na vier jaar mag je eindelijk mijn bureau afkuisen, goed he!

Weinigen weten het, maar het instituut voor kern-en stralingsfysica zit in werkelijkheid vol sportievelingen. Hierbij denk ik aan de vele glansrijke overwinningen van onze voetbalploeg, met als hoogtepunt het binnenhalen van de science cup in 2009! Ook onthoud ik de gezellige middagloopjes, de hilarische ijshockey match en uiteraard de massale opkomst voor de bike&run.

Bram, oftewel de populairste assistent van de KULeuven, bedankt voor de vele gezamenlijke didactische momenten bij de medicastudenten...

En dan hebben we nog ons Marie, ondanks het feit dat mijn mopjes soms aan de groffe kant zijn[A] hebben we toch heel wat afgelachen in den bureau. Als ik al onze fijne momenten uit de voorbije vier jaar moet gaan opnoemen kan ik beter mijn thesis in het voorwoord zetten. Bedankt voor je hulp bij het componeren van het NMR clublied, de gratis vijfgangenmenu, het heropvoeden van onze Fritz, de schoolreis met onze Japanse kindjes en de MASHkes in Ganil... Veel succes in la douche France en au recevoir!

Alleen thuis zijn vind ik maar niks. Gelukkig is dit bijna nooit voorgevallen dankzij mijn sfeervolle kotgenoten op Groenveld: Jos, Jozef, Ivau, 2BNele,

[A] *M. Derydt, private communication*

Dolf en Wim en de Tervuursestraat 81 Kobe, Mich, Bram, Charlotte, Marijn, Riki, Mathias en Eline. Ik ga jullie missen!

Niks leuker dan je eens goed af te reageren na een dag thesissen. Daarom was ik blij dat ik "s avonds of in het weekend eens naar de judo of de voetbal kon. Volgend jaar spelen zowel judoteam Duffel als de Visboys kampioen!

Mijn vrienden in het Duffel-Kontichse, bedankt om mij van mijn werk te houden als het nodig was en de vele hilarische feestjes en festivals.

Tot slot wil ik de mensen bedanken die het begrip 'thuis' een extra dimensie geven. Ma, pa, Lies, Geert, Jokelien en heel de rest van de familie, bedankt voor jullie steun. Vrienden kan je kiezen, familie niet, maar met jullie heb ik toch geluk gehad.

Abstract

This work presents the nuclear spins, magnetic moments, quadrupole moments and differences in mean square radii of the Cu isotopes $^{58-75}$Cu. The collinear laser spectroscopy technique was used. The experiments were performed at the collinear laser spectroscopy setup COLLAPS at ISOLDE, CERN. A detailed overview of the setup and the analysis procedure of laser spectroscopy data is given in this work. A recent technical improvement was the installation of the RFQ beam cooler, which allowed to extend the measurements toward more exotic isotopes. The ground-state spin inversion for the odd-A Cu isotopes from spin $3/2$ to $5/2$ is established to occur at ^{75}Cu. This result presents a breakthrough in experimental and theoretical investigations in this region. The spin-parity of the odd-odd Cu isotopes $^{72-74}$Cu is determined to be 2^-. The resulting magnetic moments and quadrupole moments are compared with theoretical calculations in a $f_{5/2}pg_{9/2}$ model space and a pf shell model space.

The magnetic moments of the odd-A Cu isotopes clearly show that excitations across the $Z = 28$ and $N = 28$ shell gaps need to be included in the model space to reproduce the experimental trend, providing another evidence of the softness of the ^{56}Ni core. The odd-A as well as the odd-odd A Cu isotopes illustrate the sensitivity of the magnetic moment to the detailed composition of the wave function, which makes magnetic moments crucial parameters to evaluate shell model calculations.

The quadrupole moments show a minimum in collectivity at $N = 40$. However, this is not entirely related to the magnitude of the $N = 40$ subshell gap but largely induced by the opposite parity of the $g_{9/2}$ orbit compared to the pf shell orbits, which blocks single-particle excitations across $N = 40$. The experimental quadrupole trend does not support an increase of collectivity beyond $N = 40$. Theoretical calculations in a pf

model space appear to underestimate the experimental core polarization for the neutron-deficient Cu nuclei.
The procedure of extracting the differences in mean square charge radii from the measured isotope shifts is given in detail. Comparison of the mean square charge radii with the droplet model prediction suggests a significant collectivity in the Cu isotope chain. A small structural effect at $N = 40$ is observed.

Korte samenvatting

Dit werk bevat de kernspins, magnetische momenten, kwadrupoolmomenten en verschillen in gemiddelde kwadratische kernstraal van de koperisotopen $^{58-75}$Cu. Er werd gebruik gemaak van de collineaire laserspectroscopie techniek. De metingen werden verricht aan de laser spectroscopie opstelling COLLAPS in ISOLDE, CERN. Een gedetailleerde beschrijving van de opstelling en de analyseprocedure voor laserspectroscopie data wordt gegeven in dit werk. Een recente technische ontwikkeling was de installatie van een RFQ bundelkoeler, die toeliet metingen te verrichten op meer exotische isotopen. Een belangrijk resultaat voor verdere theoretische en experimentele studies was de meting van de spin van de grondtoestand van ^{75}Cu. Deze bleek 5/2 te zijn, in vergelijking met de spin 3/2 grondtoestand van ^{71,73}Cu. De spin-pariteit van de oneven-oneven koperisotopen ^{72,74}Cu werd bepaald op 2^-.
De resulterende magnetische- en kwadrupoolmomenten worden vergeleken met theoretische berekeningen in een $f_{5/2}pg_{9/2}$ modellenruimte en een pf schil modellenruimte.
De magnetische momenten van de oneven koperisotopen tonen duidelijk aan dat excitaties over de $Z = 28$ en $N = 28$ schilsluitingen tot de modellenruimte moeten behoren om de experimentele trend te reproduceren. Dit is een duidelijk bewijs van de polariseerbaarheid van de ^{56}Ni kern. De magnetische momenten van zowel oneven als oneven-oneven koperisotopen blijken essentiële parameters om shillenmodeltheorieën te evalueren, gezien de grote gevoeligheid voor de exacte samenstelling van de golffunctie.
De kwadrupoolmomenten vertonen een minimum aan collectiviteit bij $N = 40$. Dit kan echter niet beschouwd worden als een indicatie voor een aanzienlijke $N = 40$ subschilsluiting, aangezien eendeeltjesexcitaties over $N = 40$ geblokkeerd worden door het verschil in pariteit tussen het

$g_{9/2}$ niveau en de pf schil orbitalen. De experimentele kwadrupoolmomenten vertonen geen indicatie van toegenomen collectiviteit na $N = 40$. Theoretische berekeningen in een pf modellenruimte blijken de experimentele kernpolarisatie te onderschatten voor neutronarme koperkernen. De procedure om uit de gemeten isotopenverschuivingen de verschillen in gemiddelde kwadratische kernstraal te bepalen wordt in dit werk uitvoerig besproken. Een vergelijking van de verschillen in gemiddelde kwadratische kernstraal met het 'droplet' model toont een aanzienlijke collectiviteit aan in de isotopenreeks van koper. Een klein structureel effect bij $N = 40$ werd waargenomen.

Contents

List of Tables

List of Figures

Chapter 1

Introduction

Everything we know is composed of atoms, which exhibit a wide variety of shapes and sizes and are physically indivisible.
To this conclusion came the Greek philosopher Democritos in the 5th century BC. Although his atomic theory was centuries ahead of his time, one of the points he was wrong about was the indivisible nature of atoms. Nowadays the atom is known to have an internal structure, consisting of a very massive compact core, called the nucleus, and light negatively charged particles (electrons) orbiting around the core. The nucleus itself consists of positively charged protons and uncharged neutrons. Understanding the complex structure of nuclei is one of the open challenges 21st century scientists face.

More than 3600 different species of nuclei have been known to exist, displaying a wide variety of fascinating phenomena. A huge milestone in the understanding of the complex nuclear many-body problem was the nuclear shell model, as proposed by Mayer and Jensen in 1955. The assumption that every nucleon was moving in an average potential generated by the other nucleons led to an enormous simplification of the many-body problem. This implied the discovery of so-called magic numbers, proton and neutron numbers at which the nucleus appears to be more stable. Today, still the same idea of the average potential is used to reproduce and predict the behavior of nuclei. A complete calculation starting from the pure nucleon-nucleon interaction is numerically too involved for the computers nowadays. However, by accounting for a residual two-body interaction between the nucleons on top of the force

created by the average potential, more and more intriguing nuclear properties in various regions of the nuclear chart have been revealed. Phenomena such as the appearance of new magic numbers for nuclei far off stability, the onset of deformation in nuclei and the exact composition of the wavefunctions are questions which are currently raised and investigated by nuclear physicists. Excellent observables to test the predictions made by nuclear structure calculations are magnetic moments and quadrupole moments, which are increasingly the subject of experimental and theoretical research over the last two decades. Magnetic moments are very sensitive probes of the exact composition of the nuclear wavefunction, whereas quadrupole moments are indicators of the collectivity and core polarization in nuclei. Together with other parameters such as mean square charge radii, binding energies and transition probabilities they bring us closer to the complete picture of a nuclear system.

Measuring nuclear moments of nuclei far off stability (also known as 'exotic isotopes') requires a reliable experimental technique. Collinear laser spectroscopy is a high-resolution technique well suited for this purpose. A spectacular increase of results obtained with laser spectroscopy has been triggered by the development of ion beam facilities worldwide. Technical developments have pushed the limits of feasible measurements toward the more exotic isotopes.

This work presents an illustration of the tremendous experimental and theoretical advances in nuclear physics. The nuclear moments of Cu isotopes and their differences in mean square charge radii were measured at the 'isotope separator online device'(ISOLDE) ion beam facility using the technique of laser spectroscopy. Several articles were already published, while some sections present an outline for future publications. The following papers have been published:

- **paper I:**
  Nuclear spins and magnetic moments of ^{71,73,75}Cu: Inversion of $2p_{3/2}$ and $1f_{5/2}$ levels in ^{75}Cu
  K.T. Flanagan, P. Vingerhoets, M. Avgoulea, J. Billowes, M.L. Bissell, K. Blaum, B. Cheal, M. De Rydt, V.N. Fedosseev, D.H. Forest, Ch. Geppert, U. Köster, M. Kowalska, J. Krämer, K.L. Kratz, A. Krieger, E. Mané, B.A. Marsh, T. Materna, L. Mathieu, P.L. Molkanov, R. Neugart, G. Neyens, W. Nörtershauser, M.D. Seliverstov, O. Serot, M. Schug, M.A. Sjoedin, J.R. Stone, H.H.

Stroke, G. Tungate, D.T. Yordanov, and Yu. M. Volkov.
Physical Review Letters ***103****, 142501 (2009)*

- **paper II:**
  Experimental determination of an $I^{\pi} = 2^{-}$ ground state in ^{72,74}Cu
  K.T. Flanagan, P. Vingerhoets, M.L. Bissell, K. Blaum, B.A. Brown, B.Cheal, M. De Rydt, D.H. Forest, Ch. Geppert, M. Honma, M. Kowalska, J. Krämer, A. Krieger, E. Mané, R. Neugart, G. Neyens, W. Nörtershauser, M. Schug, H.H. Stroke, and D.T. Yordanov
  Physical Review C ***82****, 041302 (2010)*

- **paper III:**
  Nuclear spins, magnetic moments and quadrupole moments from $N = 28$ to $N = 46$, probes for core polarization effects
  P. Vingerhoets, K.T. Flanagan, M. Avgoulea, J. Billowes, M.L. Bissell, K. Blaum, B.A. Brown, B. Cheal, M. De Rydt, D.H. Forest, Ch. Geppert, M. Honma, M. Kowalska, J. Krämer, A. Krieger, E. Mané, R. Neugart, G. Neyens, W. Nörtershauser, T. Otsuka, M. Schug, H.H. Stroke, G. Tungate, and D.T. Yordanov.
  Physical Review C ***82****, 064311 (2010)*

The outline of this work is as follows. In the first chapter, the physics case of the Cu isotopes is presented, illustrating the importance of moment measurements in that region of the nuclear chart. In section 2, the essential information about moments and radii is given, as well as an explanation how these nuclear parameters can be extracted using the technique of laser spectroscopy. A detailed description of the experimental setup is given in chapter 3. Chapter 4 focuses on the analysis of the measurements. A selection of important results is given as well, including papers I and II. The impact of the results on the shell model calculations is discussed in chapter 5 ,where first a short introduction to shell model theories is presented. A comparison of the nuclear moments with two interactions active in a $\pi\nu(p_{3/2}f_{5/2}p_{1/2}g_{9/2})$ model space is thoroughly discussed in paper III. A next section focuses on the results of the neutron-deficient Cu nuclei compared with calculations using a ^{40}Ca core and active nucleons in the full pf shell. The last part of the

discussion explains how mean square charge radii can be extracted from a laser spectroscopy experiment, and the physical information that can be derived from this parameter. Finally, a conclusion and outlook for the future is presented.

Chapter 2

Motivation

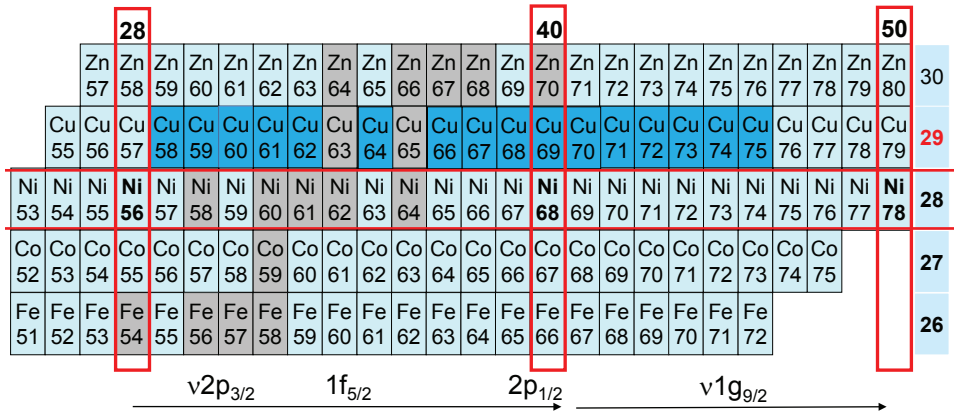

Figure 2.1: The region of the nuclear chart around the semi-magic nickel isotope chain. The number of protons is indicated on the right, the magic numbers are indicated with red lines. Below, the shell model orbits which are filled by neutrons are given. The isotopes with a gray color are stable, the copper nuclei in blue are measured, analyzed and discussed in this work.

In this chapter, the importance of studying the nuclear structure of copper isotopes is illustrated, and some physics cases are highlighted. The region of the nuclear chart around the Cu isotope chain is given in Fig. 2.1. The copper isotopes have only one proton more than the magic $Z = 28$ nickel nuclei. Furthermore, they straddle two neutron shell closures, at $N = 28$ and at $N = 50$. The magic character of the

subshell closure at $N = 40$ has attracted a lot of research interest the past decade.

The structure of the odd-A Cu isotopes is dominated by a proton in the $2p_{3/2}$ orbit, while the odd-odd Cu isotopes are ideal probes for investigating the proton-neutron coupling. From ^{57}Cu up to ^{79}Cu, the neutron levels $2p_{3/2}, 1f_{5/2}, 2p_{1/2}$, and $1g_{9/2}$ are subsequently filled up, as shown in Fig. 2.1. The $Z = 28$ shell gap is the first shell gap that arises from the spin-orbit coupling, while 40 is a harmonic oscillator magic number. Note that the $g_{9/2}$ orbital has opposite parity compared to the pf shell orbitals, which has a profound impact on nuclear structure in this region.

2.1 Evolution of single-particle energies

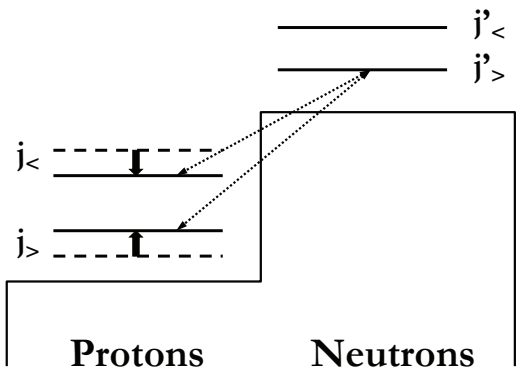

Figure 2.2: Schematic diagram of the tensor component of the monopole proton-neutron residual interaction, taken from [1].

Single-particle energies evolve as a function of the number of protons/neutrons occupying a single-particle level, leading to the appearance or disappearance of magic numbers. As these changes in single-particle energies cannot be predicted exactly, it is crucial to probe experimentally the properties of nuclei far off stability. Experimental observables are a key ingredient in developing a theory with a high predictive power for all isotopes in a specific region of the nuclear chart.

In the nickel region, beta decay studies revealed a sharply lowered position of the $\pi 1f_{5/2}$ orbital as the occupancy of the $\nu 1g_{9/2}$ increased [2]. This effect was ascribed to the monopole term of the residual proton-neutron interaction [3]. A particle-core coupling model provided an interesting alternative to the standard large-scale shell model calculations [4]. However, the parameters of this model required experimental data, yielding a high descriptive power but limited predictive power. Using the particle-core coupling model, the lowering of the $\pi 1f_{5/2}$ orbital for the odd-A copper isotopes beyond $N = 40$ was reproduced. The existence of a low-lying $1/2^-$ state was predicted as well, which was later confirmed by beta decay studies [5].

The experimental observations of changing shell structure triggered theoretical investigations, which showed that the origin of evolving single-particle energies was the spin-isospin dependent part of the nucleon-nucleon interaction [6]. This effect was later attributed to the tensor part of the monopole component [1]. Recently, novel properties of monopole interactions were presented [7]. Fig. 2.2 shows the effect of the tensor proton-neutron monopole interaction in an intuitive way. A proton orbit with total angular momentum $j_> = l + 1/2$ will lower the single particle energy of a neutron orbit with $j'_< = l - 1/2$ and vice versa. The effect is especially significant if the wave functions of the interacting orbits have a large radial overlap. For the copper isotopes, the experimentally observed lowering of the $\pi 1f_{5/2}$ orbital with the increasing occupancy of the $\nu 1g_{9/2}$ was reproduced by theoretical calculations. However, the spin inversion of the ground state from $3/2^-$ to $5/2^-$ was predicted by different theories between ^{73}Cu and ^{79}Cu [1, 8–11].

The experimental determination of the ground-state spin inversion of the copper isotopes was one of the results from this thesis work, and presented a breakthrough for new theoretical and experimental investigations in the region. This achievement is described in paper I [12]. The lowering of the $\pi 1f_{5/2}$ orbital has also a profound impact on the level structure of the odd-odd copper isotopes. Beta decay studies assigned the ground-state spin of (2) for ^{72}Cu. The firm assignment of a spin-parity 2^- for the ^{72,74}Cu isotopes and its shell model implications are discussed in paper II.

2.2 Magicity of (sub)shell gaps

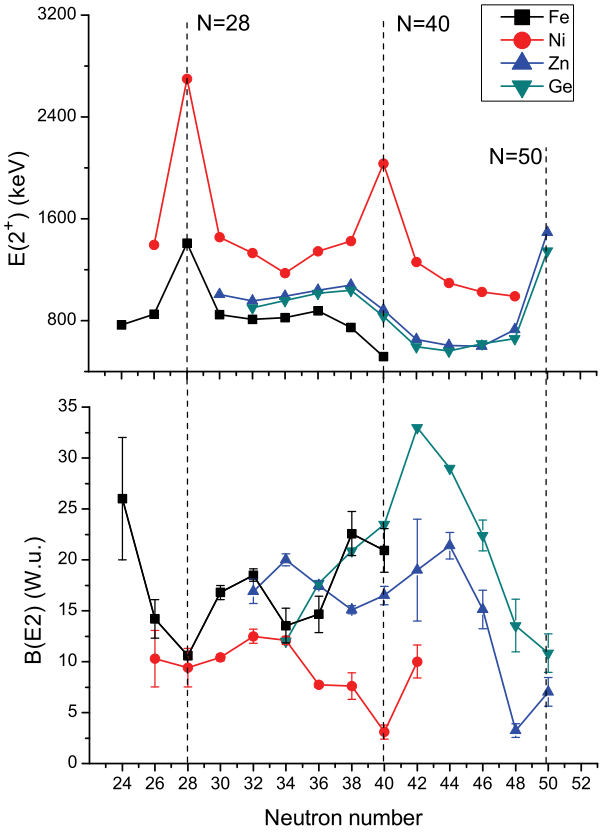

Figure 2.3: Systematics of 2^+ excitation energies and $B(E2, 2^+ \rightarrow 0^+)$ values for the even-even nuclei around nickel. Data taken from [13–21].

The first suggestion of the magic character of ^{68}Ni was based on the experimental observation that its first excited state had a spin-parity of 0^+ instead of 2^+, comparable with other known magic nuclei like ^{40}Ca [25]. Especially during the past decade, a lot of experimental and theoretical studies shed light on the magic character of ^{68}Ni and the $N = 40$ subshell closure in general [26–32]. Different observables such as excitation energies [15, 25–27, 30, 33–39], B(E2) values [5, 16, 19, 20, 32, 40–44], magnetic moments [43–50] and nuclear masses [22–24] were

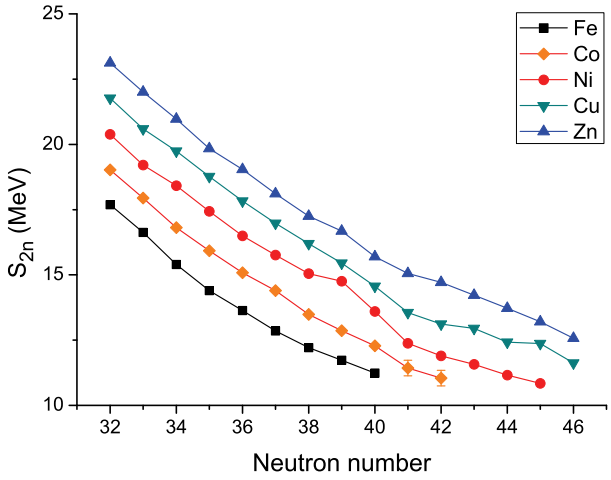

Figure 2.4: Two-neutron separation energies as a function of neutron number. Data taken from [13, 22–24]

measured to test the magic behavior of the $N = 40$ subshell gap for various nuclei. In Fig. 2.3, the excitation energies of the first excited 2^+ states and $B(E2, 2^+ \rightarrow 0^+)$ are shown. At $N = 40$, a clear increase in excitation energy of the 2+ state was observed, which was interpreted as an indication of magicity [33]. However, the stabilizing effect of the $N = 40$ subshell gap was found to disappear already when adding or removing a single nucleon or a pair of nucleons from the ^{68}Ni core [30, 34]. Coulomb excitation studies revealed an unexpectedly low $B(E2, 2^+ \rightarrow 0^+)$ value for ^{68}Ni [20], however shell model studies argued that only a fraction of the $B(E2)$ strength populated the first excited 2^+ state [29]. Furthermore, the high-lying 2^+ state should be related to the parity change between the $g_{9/2}$ orbital and the pf shell, which prohibits mixing of single-particle quadrupole excitations across $N = 40$ in the ground-state wavefunction.

A better observable to probe the magicity of nuclei is the two-neutron separation energy S_{2n}, given in Fig. 2.4. This parameter is derived from mass measurements as the difference in binding energy when removing two neutrons from a nucleus. Generally, two-neutron separation energies decrease smoothly with increasing neutron numbers, and any discontinuity in the trend indicates shell effects. The isotopes ^{67,68}Ni appear to

be slightly more bound than their neighbors, while ^{70,71}Cu are clearly less bound. However, this deviation is smaller than 1 MeV, which is in line with the assumption that $N = 40$ is only a weak subshell closure [23].

In paper III the stabilizing effect of the $N = 40$ is tested for magnetic moments and quadrupole moments, and the ability of shell model calculations to reproduce these peculiar features is discussed in detail. Magnetic moments will prove to be very sensitive to the exact composition of the wavefunction, and together with energy levels they provide a stringent test for theoretical calculations in the entire region. Differences in mean square charge radii are excellent parameters to test the magic character of the $N = 40$ subshell gap, which is discussed in section 6.4.

The $Z = 28$ gap was found to exhibit magic properties such as a high-lying 2^+ state and a low $B(E2, 2^+ \rightarrow 0^+)$ value as well [13, 51]. But in contrast with the $N = 40$ subshell gap, mass measurements revealed that this gap was sizeable in energy for pf shell nuclei [23, 52]. However, experimental observations [42, 45, 53–58] as well as theoretical calculations [55, 59, 60] suggested that the ^{56}Ni core is rather soft, which implies that excitations across the $Z, N = 28$ shell gap have to be taken into account. Two-neutron separation energies provided evidence of a reduction of the $N = 50$ energy gap for proton-deficient pf shell nuclei towards ^{82}Ge, and a subsequent increase for ^{81}Ga [61]. This suggests the persistence of the $N = 50$ shell gap for ^{78}Ni. The low energy structure of ^{72,74,76}Ni showed no indication of excitations across $N = 50$, however significant $Z = 28$ core breaking could be present [62]. Unfortunately, due to the high neutron-to-proton ratio for isotopes near ^{78}Ni, no direct experimental data are currently available about the size of the $N = 50$ shell gap for nickel, copper or zinc.

2.3 Onset of collectivity?

A compelling question in this region of the nuclear chart is the onset of collectivity when adding or removing nucleons from the ^{68}Ni core. In the nickel isotopes the low-lying energy structure is well described by single-particle excitations coupled to vibrations of the core. For the cobalt isotopes however, strong proton-neutron correlations give rise to a prolate deformed $1/2^-$ isomer at low excitation energy in ^{67}Co [36].

Beta-decay studies suggested a significant deformation in the low-lying levels for iron and chromium isotopes near $N = 40$ as well [21, 30, 37, 63, 64]. For the zinc and germanium isotopes, a more gradual onset of collectivity beyond $N = 40$ can be observed [17, 18], which disappears when the $N = 50$ shell closure is approached, indicating the persistence of the $N = 50$ shell gap. g-factor and lifetime measurements on ^{70}Zn suggested a vibrational structure mixed with single-particle excitations for this nucleus [43]. A strong influence of the fractional filling of the $g_{9/2}$ orbit on the collectivity in the germanium isotopes was suggested [40]. Transition probabilities and 2^+ excitation energies of Zn isotopes were reasonably well reproduced by shell model calculations [17]. A very recent calculation employing a $pfg_{9/2}d_{5/2}$ model space successfully described the onset of collectivity in neutron-rich even-even nuclei around $N = 40$ [65]. The quadrupole moments of the odd-A gallium isotopes (Z=31) show a strong oblate core polarization in ^{75,77}Ga, dominated by one proton in the $2\pi(p_{3/2})$ orbit, while ^{79}Ga shows a prolate core polarization, dominated by three protons in the $f_{5/2}$ orbit [50].

For the copper isotopes, the measured excitation energies and $B(E2)$ transition probabilities are shown in Fig. 2.5 [5]. On the left side, the results for the $3/2^-$ and the $5/2^-$ states are given. The energy of the $1/2^-$ and the $5/2^-$ states decreases drastically when adding neutrons to the $g_{9/2}$ orbit, however the B(E2) values to the ground state suggest that the collectivity of the two states is fundamentally different. The $5/2^-$ state appears to be rather pure single-particle like, while the $1/2^-$ shows a surprisingly collective character. On the right side of Fig. 2.5, a core-coupled $7/2^-$ state follows the trend of the 2^+ state of the underlying nickel core.

These results clearly show that for the copper isotopes, single-particle and collective effects coexist at low excitation energy [5]. Located between the semi-magic Ni isotope chain and the more deformed Zn isotopes, an open question is related to the magnitude of the core polarization of the Cu ground states, and if an onset of collectivity beyond $N = 40$ can be observed. An excellent parameter to probe the collectivity is the spectroscopic quadrupole moment. The quadrupole moment trend reveals the core polarization of the ground state copper nuclei and provides a stringent test for shell model theories in the region. This will be discussed in paper III.

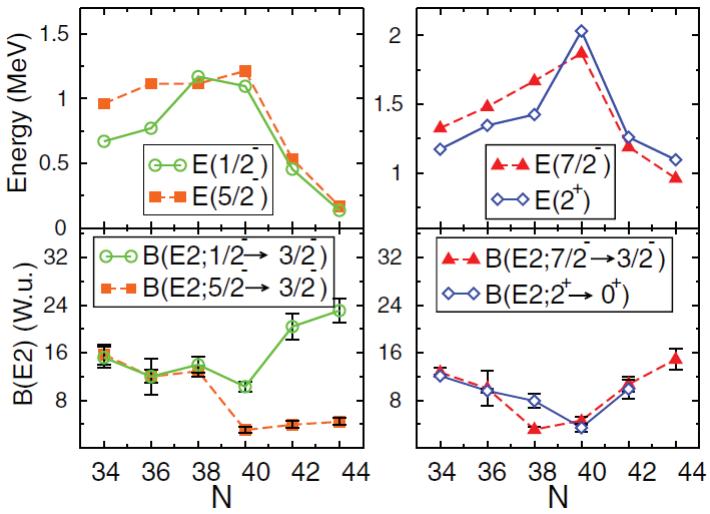

Figure 2.5: (left) Excitation ernergy and $B(E2, 2^+ \rightarrow 0^+)$ values of the $5/2^-$ and $1/2^-$ states in Cu. (right) A collective core-coupled $7/2^-$ state compared with the 2^+ state of the underlying Ni core. Taken from [5].

Chapter 3

Measurement of electromagnetic moments and charge radii

Electromagnetic moments and charge radii are very sensitive to nuclear structure and are good parameters to test the nuclear shell model theories. In this chapter, the theoretical background about these nuclear observables is introduced. A second part of this chapter explains how electromagnetic moments and differences of mean square charge radii can be extracted using the collinear laser spectroscopy technique.

3.1 The nuclear charge radius

A well-known first approximation of the magnitude of the nuclear radius is given by [66]:

$$r = r_0 A^{1/3} \tag{3.1}$$

with r_0 a proportionality constant of about 1.2 fm and A the mass number of the atom. However, as in the atomic case, the nuclear radius is not a well-defined quantity. For electromagnetic experimental methods, like measurements of optical transitions, elastic electron scattering experiments and determination of transition energies in muonic atoms, the experimentally accessible observable is the 'mean squared charge radius' (MSCR), which is given by [67]:

$$\langle r^2 \rangle = \frac{\int \rho_N(r) r^2 d\tau}{\int \rho_N(r) d\tau} \tag{3.2}$$

where $\rho_N(r)$ is the charge distribution over the nuclear volume, and the denominator of the equation is a normalization factor given by Ze, with Z the proton number and e the fundamental electron charge. In a first approach, the nucleus could be described by a perfect solid sphere, like in the liquid drop model. This would give a sharp edge of $\rho_N(r)$ at r. In a more realistic situation, for spherical nuclei the two-parameter Fermi charge distribution function is often used, given by:

$$\rho_N(r) = \rho_0 (1 + e^{\frac{r-c}{a}})^{-1} \tag{3.3}$$

where c is the half-density radius, and a is defined in terms of the skin thickness parameter t:

$$t = 4a\ln 3. \tag{3.4}$$

This parameter is the distance over which the charge density falls from 90% of its central value to 10% of its central value. The skin thickness is roughly constant throughout the nuclear chart with a value of about 2.3 fm.

3.2 The magnetic moment

The magnetic moment arises from orbiting charged particles which generate a magnetic field. In the quantummechanical description of the nucleus, another contribution to the magnetic moment is caused by the so-called intrinsic spin $s = 1/2$, where the nucleon generates its own magnetic field. The definition of the magnetic dipole operator is commonly given by [68]:

$$\boldsymbol{\mu} = \sum_{i=1}^{A} g_L^{(i)} \mathbf{L}^{(i)} + \sum_{i=1}^{A} g_S^{(i)} \mathbf{S}^{(i)} \tag{3.5}$$

where the $\mathbf{L}^{(i)}$ and the $\mathbf{S}^{(i)}$ are orbital and spin angular momentum of the (i)th nucleon, and the sum ranges over all nucleons. $g_L^{(i)}$ and $g_S^{(i)}$ are the orbital and spin g-factors. For a proton $g_L^{(i)} = 1$ and for a neutron $g_L^{(i)} = 0$. The spin g-factors are given by [68]:

$$g_S^{(\pi)} = 5.587, \quad g_S^{(\nu)} = -3.826 \tag{3.6}$$

Note that the uncharged neutron has a nonzero magnetic moment, which is an indication that it is not a point particle but has an internal structure. The magnetic moment is given by:

$$\mu = gI\mu_N \tag{3.7}$$

with g the nuclear g-factor and I the total angular momentum of the state. μ_N is called the nuclear magneton, and is given by:

$$\mu_N = \frac{e\hbar}{2m_p} = 5.05084 \cdot 10^{-27} J/T \tag{3.8}$$

where e is the electronic charge, $\hbar = 1.054589 \cdot 10^{-34} J \cdot s$ and m_p the proton mass. Magnetic moments are usually expressed in units of nuclear magneton. The magnetic moment of a composite state can be expressed in terms of the magnetic moments of its constituents. This is known as the addition theorem [69]:

$$\mu = I\left[\frac{1}{2}(\frac{\mu_1}{I_1} + \frac{\mu_2}{I_2}) + \frac{1}{2}(\frac{\mu_1}{I_1} - \frac{\mu_2}{I_2})\frac{I_1(I_1+1) - I_2(I_2+1)}{I(I+1)}\right] \tag{3.9}$$

or analogously with g-factors:

$$g = \frac{1}{2}(g_1 + g_2) + \frac{1}{2}(g_1 - g_2)\frac{I_1(I_1+1) - I_2(I_2+1)}{I(I+1)} \tag{3.10}$$

with $\mu_{1,2}$ and $g_{1,2}$ the magnetic moments and g-factors, and $I_{1,2}$ the nuclear spins of the constituents. Assuming weak coupling between protons and neutrons, this formula can be used to calculate moments from odd-odd isotopes using the magnetic moments of neighboring odd isotopes in the nuclear chart. The resulting moment is called the empirical magnetic moment. Examples of this for the Cu isotopes are given in paper III. A special case of the addition theorem is a single nucleon orbiting in a shell model orbital. This can be regarded as the coupling of an orbital part l and a spin part $s = 1/2$ coupled to the total angular momentum j. Equation 3.10 becomes:

$$g(j = l \pm \frac{1}{2}) = g_L \pm \frac{g_S - g_L}{2l + 1} \tag{3.11}$$

This expression can be rewritten as [68]:

$$\mu = \left[(j - \frac{1}{2}) g_L + \frac{1}{2} g_S \right] \mu_N \quad \text{for j} = \text{l} + 1/2 \tag{3.12}$$

$$\mu = \frac{j}{j+1} \left[(j + \frac{3}{2}) g_L - \frac{1}{2} g_S \right] \mu_N \quad \text{for j} = \text{l} - 1/2 \tag{3.13}$$

$$\tag{3.14}$$

These magnetic moments of a free proton(neutron) orbiting in a single shell model orbital are called the Schmidt moments. For a given spin, almost all observed magnetic moments are between the two Schmidt estimates for $j = l \pm 1/2$. The agreement is often poor, as the picture of an odd particle orbiting a single shell model orbit is only an approximation, and other contributions to the ground-state wave function have to be taken into account.

3.3 The quadrupole moment

The quadrupole moment arises from a non-spherical charge distribution of the nucleus. The electric quadrupole operator is defined as:

$$\mathbf{Q}_z = \sum_{i=1}^{A} e_{free}^{(i)} (3z_i^2 - r_i^2) \tag{3.15}$$

with $e_{free}^{(i)}$ the free nucleon charge, equal to the fundamental charge e for protons and 0 for neutrons. So, the quadrupole moment arises entirely from the motion of the protons. The spectroscopic quadrupole moment Q_s is the expectation value of $\mathbf{Q}_z$. Using the Wigner-Eckart theorem it can be expressed as:

$$Q_s(I) \equiv \langle I, m = I | \mathbf{Q}_z | I, m = I \rangle = \sqrt{\frac{I(2I-1)}{(2I+1)(2I+3)(I+1)}} \langle I || \mathbf{Q}_z || I \rangle \tag{3.16}$$

The quadrupole moment operator is often expressed in terms of spherical tensor components:

$$\mathbf{Q}_z = \sqrt{\frac{16\pi}{5}} \sum_{i=1}^{A} e_{free}^{(i)} r_i^2 Y_2^0(\theta_i, \phi_i) \tag{3.17}$$

with r_i^2 the squared radius of the orbital of the nucleon and $Y_2^0(\theta_i, \phi_i)$ the zero-order component of the spherical tensor of rank 2 in the polar angles θ_i and ϕ_i. The spectroscopic quadrupole moment of a system consisting of a single valence proton outside a closed shell can then be evaluated as:

$$Q_{s.p.} = -e\frac{2j-1}{2(j+1)}\langle r^2 \rangle. \tag{3.18}$$

The minus sign in this equation shows that the quadrupole moment is negative for a single particle orbiting a closed shell. The core polarization induced by the particle will lead to an oblate or disc-shaped ellipsoid. Likewise, a single hole in a closed shell will lead to a positive quadrupole moment, and a prolate charge distribution.

3.4 Hyperfine structure

The free atomic nucleus is not an isolated many-body system, but is constantly interacting with its surrounding electron cloud. Different contributions to the nucleus-electron interactions are separated out by making a multipole expansion of the interaction Hamiltonian [70, 71]:

$$H_{int} = H(E0) + H(M1) + H(E2) + ... \tag{3.19}$$

with $H(E0)$ the electric monopole, $H(M1)$ the magnetic dipole, and $H(E2)$ the electric quadrupole term. Interactions between the nucleus and the electron cloud which depend on the shape and/or size of the nucleus, like the latter two terms in equation 3.19, are called hyperfine interactions. In absence of an externally applied field, an atomic state of a free atom can be described by the quantum numbers I, J, F, and m_F, where m_F is the z-component of the vector $\vec{F}$, which arises from the coupling of the nuclear and electronic angular momenta:

$$\vec{F} = \vec{I} + \vec{J}. \tag{3.20}$$

The possible values of F range from $|I - J|$ to $|I + J|$.

3.4.1 The magnetic dipole interaction

The Hamiltonian of the magnetic dipole interaction can be written as:

$$H(M1) = -\hat{\mu} \cdot \hat{B}(0) \tag{3.21}$$

with $\hat{\mu}$ the nuclear magnetic moment operator interacting with the magnetic field operator of the electrons at the position of the nucleus $\hat{B}(0)$. This can also be written as:

$$-\hat{\mu} \cdot \hat{B}(0) = -A\hat{I} \cdot \hat{J} \tag{3.22}$$

where the magnetic hyperfine coupling constant A is given by:

$$A = \frac{\mu B(0)}{IJ} \tag{3.23}$$

Experimentally, transition frequencies are determined, and the observable hyperfine coupling constant A_ν is measured in frequency units (typically MHz):

$$A_\nu = \frac{\mu B(0)}{hIJ} \tag{3.24}$$

Using the well known relation

$$2\hat{I} \cdot \hat{J} = \hat{F}^2 - \hat{I}^2 - \hat{J}^2 \tag{3.25}$$

one can evaluate the Hamiltonian of equation 3.22 in a state characterized by the quantum numbers (I, J, F, m_F) and obtain the energy difference with the unperturbed state due to the magnetic dipole interaction:

$$E_{F,magn} = \langle I, J, F, m_F | H(M1) | I, J, F, m_F \rangle = \frac{AC}{2} \tag{3.26}$$

with

$$C = F(F+1) - I(I+1) - J(J+1). \tag{3.27}$$

3.4.2 The electrostatic quadrupole interaction

The deviation from spherical symmetry of the nuclear and electronic charge distributions will cause a shift in the energy levels as well [70, 71]:

$$E_{F,quad} = B\frac{\frac{3}{4}C(C+1) - 2I(I+1)J(J+1)}{2I(2I-1)J(2J-1)} \tag{3.28}$$

where C is given by equation 3.27 and B the quadrupole coupling constant or shortly B-factor. It is related to the spectroscopic quadrupole moment by:

$$B = eQ_s V_{zz}(0) \tag{3.29}$$

where Q_s is the spectroscopic quadrupole moment, given in barns and $V_{zz}(0)$ the Z-component of the electric field gradient of the orbital electrons at the position of the nucleus. Analogous to the A-factor, the B-factor is measured in experiments as a frequency:

$$B_\nu = \frac{B}{\hbar} \tag{3.30}$$

Note that levels with angular momentum $I < 1$ or $J < 1$ do not exhibit a hyperfine splitting due to the electrostatic quadrupole interaction. Therefore, the $3d^{10}4s\ ^2S_{1/2} \rightarrow 3d^{10}4p\ ^2P_{3/2}$ $J = 1/2$ to $J = 3/2$ transition is used to study the copper nuclei with collinear laser spectroscopy. The $3d^{10}4s\ ^2S_{1/2} \rightarrow 3d^{10}4p\ ^2P_{1/2}$ transition is used by in-source experiments for studies of the magnetic moment only, as the resolution of this technique is anyway too low to resolve the small quadrupole splitting.

3.5 Collinear laser spectroscopy

Collinear laser spectroscopy is a very powerful high-resolution technique to measure electromagnetic moments and differences in charge radii. It makes use of laser-induced excitations between hyperfine split electronic levels to deduce properties of the nucleus. It is performed on an accelerated beam in order to obtain a high resolution. Indeed, the energy spread of an ion beam remains constant under acceleration and is given by:

$$\delta E = \delta(\frac{mv^2}{2}) = mv\delta v = \text{constant}. \tag{3.31}$$

It is clear that if δE is constant and if the velocity of the beam is increased, the velocity spread is consequently reduced. A typical example of a hyperfine spectrum measured with collinear laser spectroscopy is given in Fig. 3.1. The upper part of the figure shows two hyperfine split electronic states according to the quantum number **F** (see Eq. 3.20), $^2S_{1/2}$ and $^2P_{3/2}$. For a nucleus with spin 3/2, there are six allowed transitions between the different hyperfine levels, as indicated by the arrows in Fig. 3.1. The frequency of these transitions can be determined by scanning a laser, and when the laser frequency matches a transition frequency resonant excitations can be made and the consequent de-excitations can be observed. The X-scale of the hyperfine structure in the lower part of Fig. 3.1 represents the frequency relative to the transition frequency of a reference isotope, usually a stable and strongly produced isotope.

In fact, a much easier method to scan across the resonances is by scanning the laser frequency via the Doppler effect, by varying the ac-

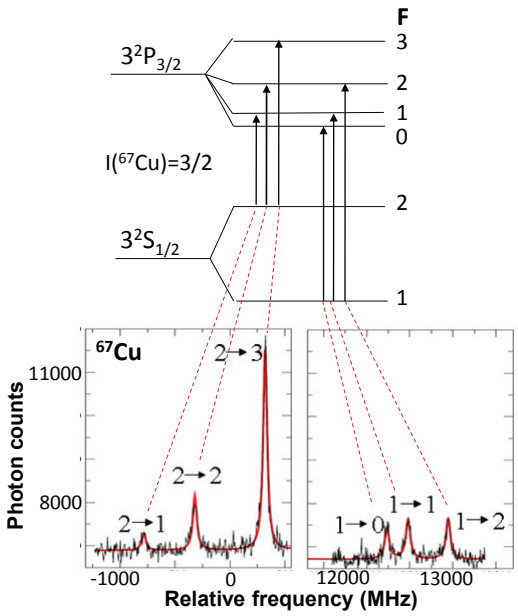

Figure 3.1: An example of a spectrum obtained with laser spectroscopy for the $^2S_{1/2}$-$^2P_{3/2}$ transition in ^{67}Cu. The A-and B-factors are deduced from the relative peak positions according to equation 3.34.

celeration potential. The relation between the acceleration voltage and the frequency is given by:

$$\beta = \sqrt{1 - \frac{M^2c^4}{(Mc^2 + q \cdot V_{tot})^2}} \tag{3.32}$$

$$\nu_{transition} = \nu_{laser}\sqrt{\frac{1-\beta}{1+\beta}} \tag{3.33}$$

where β is the ratio of the speed of the beam to the speed of light, V_{tot} the total acceleration voltage, q the charge state of the atom and M the mass of the isotope. With an acceleration voltage of 50kV, the value of β is around 0.0013 for ^{65}Cu.

In order to extract physical information from a spectrum like in Fig. 3.1, one can use equation 3.34 to obtain the dependence on the A and B hyperfine structure parameters (also called A- and B-factors):

$$\nu_F = \frac{E_F}{h} = \frac{1}{2}A_\nu C + B_\nu \frac{\frac{3}{4}C(C+1) - I(I+1)J(J+1)}{2I(2I-1)J(2J-1)} \tag{3.34}$$

with C given by Eq. 3.27, and E_F the energy difference of the hyperfine states with the unperturbed state due to the magnetic dipole and electric quadrupole interaction. The hyperfine structure constants A_ν and B_ν can be used to obtain magnetic and quadrupole moments, respectively. This is done according to equations 3.35 and 3.36:

$$\mu = \frac{A_\nu I}{A_{\nu,ref} I_{ref}} \mu_{ref} \tag{3.35}$$

$$Q = \frac{B_\nu}{B_{\nu,ref}} Q_{ref} \tag{3.36}$$

where μ_{ref}, Q_{ref} is the magnetic and quadrupole moment of a reference nucleus, measured with a different technique.

Each of the above-mentioned steps, conversion of the acceleration voltage into a frequency scale, extraction of A and B factors by fitting a spectrum, and determination of magnetic and quadrupole moments, will be discussed in detail in chapter 5.

3.6 Nuclear information from isotope shifts

Atomic energy levels of two isotopes of any element are shifted relative to each other. If ν^A is the frequency of an atomic transition (for example the $3d^{10}4s\ ^2S_{1/2} \rightarrow 3d^{10}4s\ ^2P_{3/2}$ transition in Cu), the isotope shift between two elements of mass number A and A' for that specific transition is given by [70, 72]:

$$\delta\nu^{A,A'} = \nu^{A'} - \nu^{A}. \tag{3.37}$$

The isotope shift is positive when the frequency of the transition of the heavier isotope is higher. The two main contributions to the isotope shift are the mass shift and the field shift:

$$\delta\nu^{A,A'} = \delta\nu_{MS}^{A,A'} + \delta\nu_{FS}^{A,A'} \tag{3.38}$$

where the mass shift $\delta\nu_{MS}^{A,A'}$ arises from the mass difference between the lighter and the heavier nucleus, and the field shift $\delta\nu_{FS}^{A,A'}$ originates from the fact that the energies of atomic levels depend on the size of the nuclear charge distribution.

In collinear laser spectroscopy experiments, the value of the isotope shift between two isotopes is determined by subtracting the center of gravity of their respective hyperfine structures. Unfortunately, extraction of the differences in mean square charge radii from the measured isotope shifts is more complicated compared to magnetic and quadrupole moment evaluation, where we could just use equations 3.35 and 3.36.

3.6.1 The mass shift

The two terms contributing to the mass shift are the 'normal mass shift' $\delta\nu_{NMS}^{AA'}$ and the 'specific mass shift' $\delta\nu_{NMS}^{AA'}$:

$$\delta\nu_{MS}^{AA'} = \delta\nu_{NMS}^{AA'} + \delta\nu_{SMS}^{AA'}. \tag{3.39}$$

The normal mass shift arises from the reduced mass correction of the system nucleus + electrons and can be calculated in a straightforward way:

$$\delta\nu_{NMS}^{AA'} = \frac{A' - A}{AA'} m_e \nu_A \tag{3.40}$$

with m_e the electron mass and ν_A the frequency of the transition. The normal mass shift is always positive, shifting the heavier isotope to higher frequencies. For heavy isotopes, this contribution is very small due to the factor AA' in the denominator. The specific mass shift originates from the influence of correlations in the motion of electrons on the recoil energy of the nucleus and can have either sign, depending on correlations between all the electrons in the atom. It is very hard to calculate and often the specific mass shift has to be estimated. For $ns \rightarrow np$ transitions, the specific mass shift is ususally in the range [73]:

$$\delta\nu_{SMS}^{AA'} = (0.3 \pm 0.9)\delta\nu_{NMS}^{AA'} \tag{3.41}$$

3.6.2 The field shift

The field shift, which originates from the difference in nuclear charge distribution between isotopes, contains the mean square charge radius information. For a given transition it can be written as [74]:

$$\delta\nu_{FS}^{AA'} = F\lambda^{AA'} \tag{3.42}$$

where F is called the field shift constant and $\lambda^{AA'}$ a parameter given in terms of the radial nuclear charge parameters:

$$\lambda^{AA'} = \delta < r^2 >^{AA'} + \frac{C_2}{C_1}\delta < r^4 >^{AA'} + ... \tag{3.43}$$

The coefficients C_n are tabulated in [75]. For elements of light and medium mass, the higher charge moments are much smaller than the error in evaluation of $\lambda^{AA'}$. The coefficient $\frac{C_2}{C_1}$ is calculated to be of the order of 10^{-4}fm^{-2} [76]. Therefore, to a good approximation

$$\lambda^{AA'} \approx \delta < r^2 > . \tag{3.44}$$

There are different methods to calculate the field shift constant in order to estimate the specific mass shift and extract the difference in mean square charge radius between isotopes. This will be explained in section 6.4 , where we work out the formula for the example of the Cu nuclei.

Chapter 4

Laser spectroscopy at the ISOLDE facility

The Cu campaign discussed in this thesis includes three different experimental beamtimes performed in 2006, 2007 and 2008. The analysis of a new run in 2010 is still ongoing and will be discussed elsewhere. Preliminary values for the deduced observables of $^{58-61}$Cu are used in the discussion. In this section, the experimental conditions during the first three beamtimes will be discussed.

4.1 Experimental setup

The beamtimes in 2006 and 2007 were performed in an experimentally similar way. The 2008 experiment could benefit from the installation of the RFQ beam cooler/buncher (as explained below) and was therefore performed in a slightly different way.

4.1.1 Ion beam production at ISOLDE

The experiment was performed at the CERN online isotope separator (ISOLDE) facility. Radioactive isotopes were produced by 1.4GeV protons impinging on a uranium carbide target, 45g/cm^2 thick. The average beam current was around 1.8μA. After diffusion out of the target, the RILIS laser ion source was used to stepwise ionize the element of interest via a 327.4nm $^2S_{1/2}$-$^2P_{1/2}$ transition followed by a 287.9 nm transition

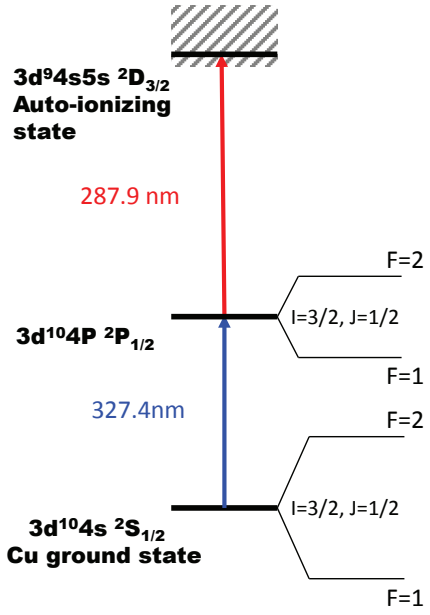

Figure 4.1: Excitation scheme of the RILIS lasers. The hyperfine structures of the ground $^2S_{1/2}$ and the $^2P_{1/2}$ intermediate state(not to scale) are given on the right.

into an auto-ionizing state. This scheme, given in Fig. 4.1 was studied by Köster et al. [77]. Afterwards the ions were accelerated to an energy of 50 keV and mass separated by the general-purpose separator (GPS). For the experiment in 2008 however, the target station connected with the high-resolution separator (HRS) was used, because behind it a linear gas-filled Paul trap ISCOOL (ISOLDE COOLer) [78, 79] is installed. Ions were accelerated to 30keV and inserted into ISCOOL. A more detailed description of this device is given in section 4.1.5. The beam is then transported via electrostatic deflection to the COLLAPS beamline.

4.1.2 The COLLAPS beamline, detection and electronics

As seen in Fig. 4.2, the copper ion beam, sent through either HRS (and the ISCOOL beam cooler/buncher) or GPS, is overlapped with the laser beam through a 10° bend by electrostatic deflectors. The ions

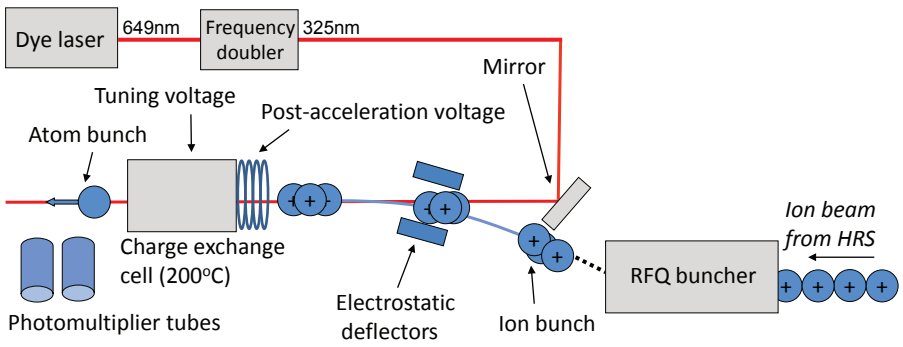

Figure 4.2: Experimental setup of the COLLAPS collinear laser spectroscopy beamline.

pass through a sodium vapor cell, which was heated to approximately 200°C, where they are neutralized. Afterwards the atom beam can interact resonantly with the laser light in the light collection region. The fluorescent decay is observed with two photomultiplier tubes. At the charge exchange cell, an extra offset voltage of ±10kV can be applied, which further accelerates or decelerates the ion beam. This offset voltage allows measurements along the complete isotope chain without having to alter the laser frequency or the initial acceleration voltage of the ions. In order to scan the total acceleration voltage across the resonances, a tuning voltage with a maximal range of ±500V can be applied as well. The signal of the photomultiplier tubes is amplified and sent through a constant fraction discriminator, which converts the signal into a logic pulse. This pulse is passed to the computer using a scaler module. The number of signals from both photomultiplier tubes are counted simultaneously.

4.1.3 The laser system

The laser system consisted of an Ar^+ pump laser and a Coherent 699 ring dye laser, and for the most recent beamtime the Ar^+ was replaced by a Verdi pump laser. In 2006-2007, the frequency of the laser was not locked. In order to keep track of drifts in voltage and laser frequency, the reference isotope was constantly monitored during measurement of a radioactive isotope by fast switching the mass selection of the GPS magnet. The laser wavenumber was around 15411.2 cm^{-1} for 2006 and

15411.6 cm^{-1} for 2007. As the HRS magnets cannot cycle fast enough to constantly monitor the reference isotope, the frequency of the laser had to be locked for the 2008 experiment. The locking was done relative to an I_2 line using frequency modulation saturation spectroscopy. The wavenumber of the line was 15406.9373cm^{-1}, as measured with a Menlo System FC1500 frequency comb. The long term drift of the laser was less than 500kHz. The fundamental laser frequency was doubled using a Spectra-Physics Wavetrain external cavity.

4.1.4 Yields

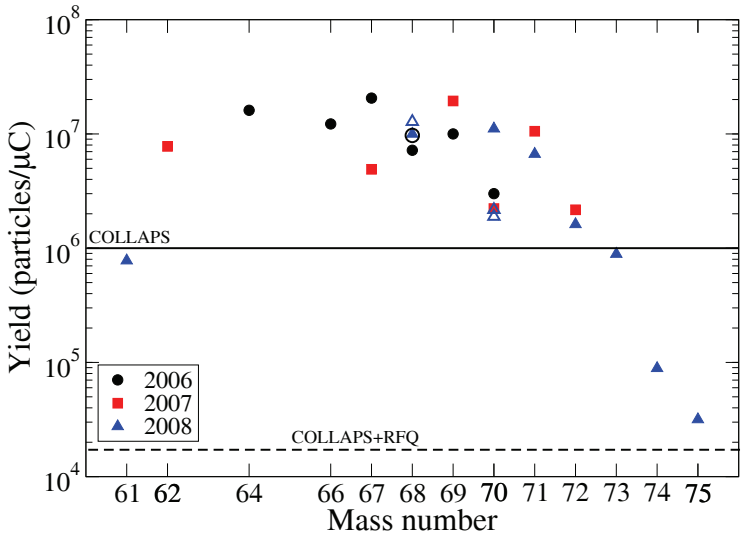

Figure 4.3: Production yield of radioactive isotopes during the experiments without ion bunching (black and red dots) and with ion bunching (blue triangles). The limit for laser spectroscopy measurements before installation of the ISCOOL device is indicated with a solid line, the current limit is given with a dashed line.

A crucial aspect for almost every experiment is the rate at which the radioactive ions are produced. This drastically influences the beamtime needed to perform the measurements. The yield of the Cu isotopes for the three experiments is given in Fig. 4.3, and has been determined as follows.

The ion beam current can be recorded on a Faraday cup after the mass separation area. However, direct determination of the production yield is not possible for most radioactive beams, as they are hardly or not observable with the Faraday cup. In order to determine the production for the radioactive beams, the photopeak intensity in the most intense transition is measured. The experimental efficiency is first determined for ^{65}Cu, and with this efficiency the production yield is calculated back for the radioactive isotope. An example with realistic values is given below. A typical value for the stable ^{65}Cu beam current after the mass separation area is 50pA, or $50{\cdot}10^{-12}$C/s. The amount of ions per second hitting the Faraday cup is then given by:

$$\frac{50 \cdot 10^{-12} C/s}{1.6 \cdot 10^{-19} C} \approx 3.1 \cdot 10^{8} \text{ions/s}$$

The efficiency for ^{65}Cu is then obtained by dividing the counts observed with the photomultiplier tubes by the ion rate seen by the Faraday cup:

$$\epsilon_{COLLAPS} = \frac{3.1 \cdot 10^{4} \text{cts/s}}{3.1 \cdot 10^{8} \text{ions/s}} = 1 : 10000$$

where $3.1 \cdot 10^4$ is a typical value for the amount of photon counts per second observed by the photomultiplier tubes for the highest peak of the ^{65}Cu hyperfine structure. For the radioactive isotopes, the yield is then determined by dividing the observed photon counts in the highest hyperfine peak by the experimental efficiency, for example:

$$yield(^{71}Cu) = \frac{\text{photoncounts}}{\epsilon_{COLLAPS}} = 1.2 \cdot 10^{7} \text{ions/s} = 6.7 \cdot 10^{6} \text{ions}/\mu\text{C}$$

In the last step the production yield is normalized with the beam current of the proton beam on the target, which had a typical value of 1.8μA The use of the RFQ beam cooler/buncher had only a minor effect on the efficiency. Indeed, offline tests showed a transmission of more than 70% [78] even for elements lighter than Cu. The production yield depends on the RILIS lasers and on the target. The experimental runs in 2006, 2007 and 2008 were preceded by a different experiment using the same target, due to which the production yield was never optimal.

4.1.5 The RFQ beam cooler/buncher

Design and offline specifications

The ISCOOL device is a gas-filled linear Paul trap, which enables trapping a certain number of ions using RF electric fields. A prototype of this device and its application for laser spectroscopy was already pioneered at the IGISOL facility in Jyväskylä [80, 81]. ISCOOL has two different modes of operation: It can deliver the beam as a continuous flux of particles (continuous mode), or accumulate ions for a certain amount of time and release the ion beam in bunches (bunched mode). A schematic diagram of the ISCOOL device is given in Fig. 4.4. It is located at the focal point of the HRS magnets, where the beam is injected in the radiofrequency quadrupole trap using injection electrodes. The ions are axially confined to the center of the trap by a potential generated by four quadrupole rods, on which an RF electric field is applied in such a way that the fields on opposite rods are in phase and on adjacent rods in anti-phase. A segmented structure of 25 electrode rings surrounds the quadrupole rods. These electrode rings are used to apply a DC voltage gradient to guide the ions more rapidly to the exit nozzle. A He gas flow with a pressure of about 0.1mbar is used to slow down and cool the ion beam via thermal collisions. A differential pumping system keeps the pressure on either side of the RFQ beam cooler/buncher below 10^{-7}mbar [79]. The cooled ions are trapped in the potential well and prevented from exiting the cooler/buncher by a stopping potential of around 50V. In extraction mode, this stopping potential is switched to 0V, which allows the ions to be extracted from the ISCOOL device. Offline tests showed an emittance of less than 3mm mrad[A], compared to an emittance of 7-14 mmmrad for the high resolution separator[82]. A transmission of 69% through the ISCOOL was observed for an element as light as K(Z=19) [78] .

Application for laser spectroscopy

The first online commissioning of the RFQ beam cooler/buncher is described in [79]. Experiments using the RFQ buncher benefit from the

[A] In literature, the unit of emittance is often given in π mm mrad. However, π is not included in the number quoted, it is there for historical reasons only. Hence I choose to remove π from the unit definition.

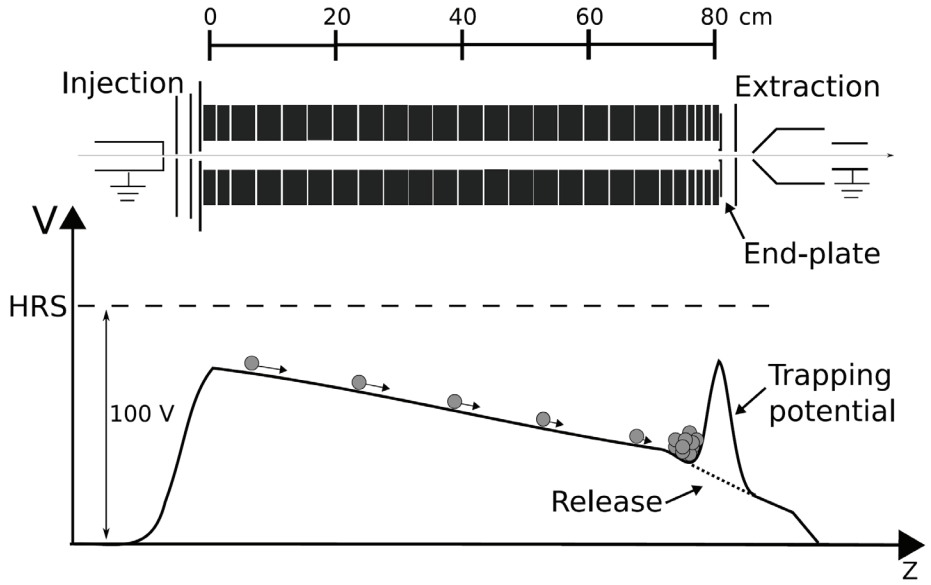

Figure 4.4: Schematic overview of the ISCOOL cooler/buncher. Taken from [79].

reduced emittance of the ion beam. Moreover, laser spectroscopy performed on a bunched beam allows a reduction of the scattered photon background, improving the signal to noise ratio dramatically. By accepting counts only when a bunch is passing in front of the photomultiplier tubes, the detected background photons can be drastically reduced. A multi-channel scaler (MCS) is used to monitor the time when bunches are passing the PMT's. The amount of the background reduction is then the ratio of accumulation time set on the RFQ cooler/buncher to the time window in which counts are accepted. During the online commissioning of the RFQ buncher a typical time window of 7-12μs was set, allowing a background reduction by a factor of 4×10^4 [79]. For the Cu experiment in 2008, the time window was 25μs, and the background was reduced by a factor of 4×10^3. Typical accumulation times were 5-100ms, dependent on the production yield of the isotope. The effect on the signal to noise ratio of the obtained hyperfine spectra and hence the scanning time is shown in Fig. 4.5, where ^{72}Cu was measured without the RFQ buncher in 2007 and remeasured with the RFQ buncher in 2008. The

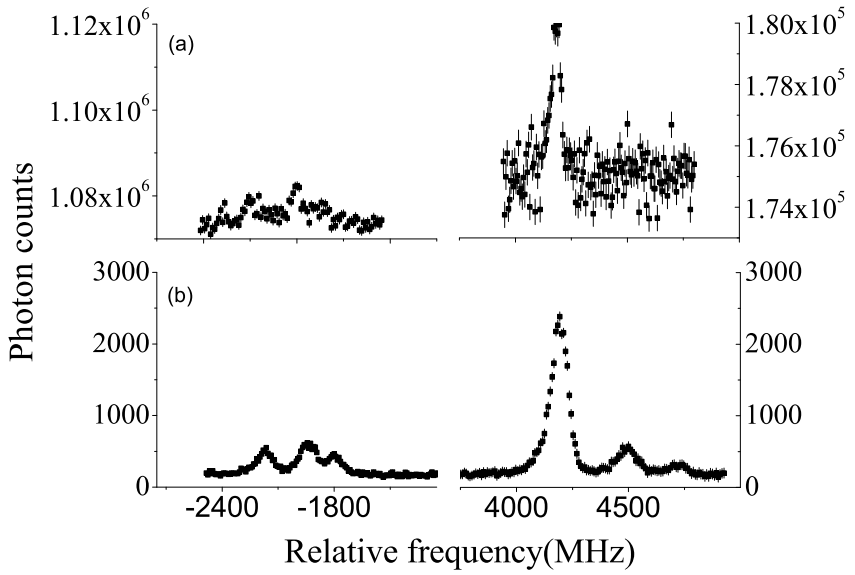

Figure 4.5: Collinear laser spectroscopy spectra for ^{72}Cu. (a) Before installation of the RFQ cooler/buncher. (b) With a bunched ion beam and photon gating, all 6 peaks are clearly resolved after 2 hours of measurement.

former spectrum took more than 10 hours to scan, while not all of the 6 peaks are resolved. In 2008, only 2 hours were needed to fully resolve the hyperfine structure. In 2007, the scanning time on each point was 30s/channel and 250s/channel for left and right multiplet respectively, while in 2008 only 3s/channel were needed.

4.1.6 Voltage calibrations

For collinear laser spectroscopy, knowledge of the ion acceleration voltage is essential for extracting reliable data. Indeed, as can be seen in Eq. 3.32, the frequency is not linearly dependent of the applied voltage. In order to make a proper conversion to frequency, the total acceleration voltage has to be known.

The ions are accelerated(decelerated) by three different voltages:

$$V_{tot} = V_{ISOLDE} + V_{offset} + Ampfactor \cdot V_{scan} \tag{4.1}$$

where V_{ISOLDE} represents the ISOLDE acceleration voltage, V_{offset}

is an extra offset voltage between 0V and ±10kV, and V_{scan} is the scanning voltage of ±10V, multiplied by an amplification factor of about 50.4. This amplification factor is calibrated regularly during the experiment and has a negligible contribution to the error on the deduced frequency (and thus on the error of the extracted fit results). For the beamtime in 2008, V_{ISOLDE} has to be replaced by V_{ISCOOL} as all ions are stopped in the cooler and reaccelerated from that point. The value of V_{ISCOOL} was 30221V in 2008. Two different voltage supplies were used for the beamtimes in 2006 and 2007, called ASTEC-1 and ASTEC-2. Laser spectroscopy analysis revealed a clear discrepancy between the results of the two experimental runs, consistent with a voltage difference of 47V at 50kV. The calibrations of the ISOLDE acceleration voltage are described in [83]. Considering the long-term stability of both power supplies mentioned in [83], an uncertainty of 2V and 3V was assumed for the power supplies ASTEC-1 and ASTEC-2, respectively. Taking into account these calibrations, consistent laser spectroscopy results were obtained for the beamtimes in 2006 and 2007.

The ISCOOL voltage has been calibrated several times. The deviation of the standard ISOLDE measurement equipment using the Keithley multimeter with a calibrated high-precision voltage divider is given in Fig. 4.6. Calibration 1 was performed before the experiment, and in very poor conditions. The device was switched on for the first time and the calibration had to be performed very rapidly. The second and third calibration, performed one month before and more than a year after the experiment, should be more reliable. However, conflicting results were obtained, even a change in polarity was observed over time. The actual voltage during the 2008 experiment was derived from laser spectroscopy results as explained in section 5.1.4. The value of the resulting voltage was found to be 30221(7)V instead of the reading 30199V, which would appear on Fig. 4.6 at -22(7)V, in clear discrepancy with the two 'reliable' calibrations. One reason for this could be the poor specifications of the ISCOOL voltage divider, which has an accuracy of only 0.2%, corresponding to 60V at 30kV! Unfortunately these specifications are inadequate to perform laser spectroscopy experiments. How this problem is circumvented for the Cu 2008 experiment is explained in section 5.1.4. The stability of the divider was sufficient for the analysis of the laser spectroscopy experiment, with a drift of less than 1V over a week.

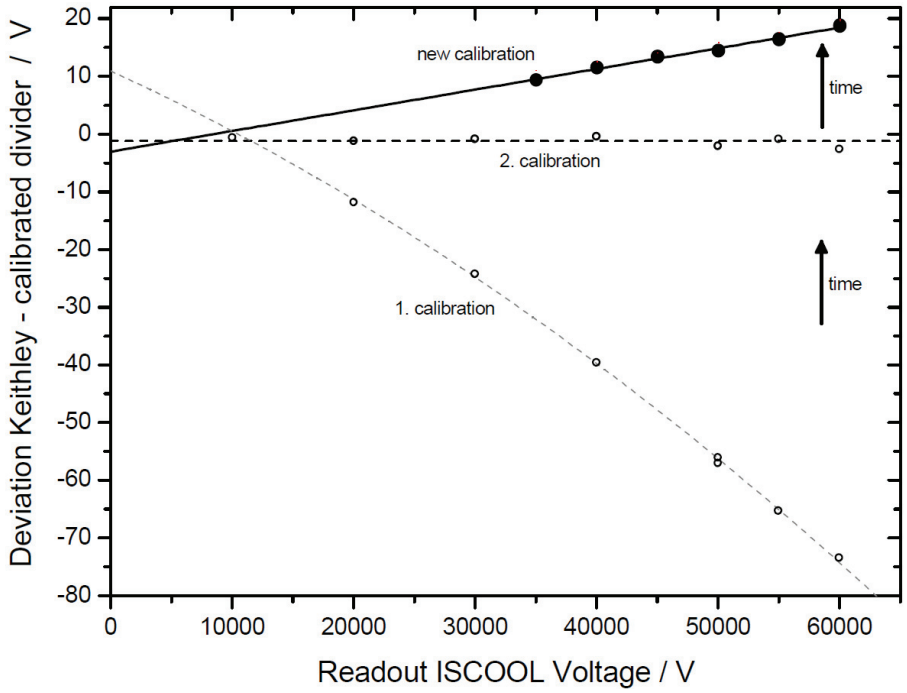

Figure 4.6: Figure taken from [84]. Three different calibrations of the ISCOOL voltage divider using a Keithley multimeter with respect to a calibrated high-precision voltage divider. A clear discrepancy over time is observed.

Chapter 5

Results

This section will focus on how the A, B parameters and isotope shifts are extracted from the data recorded during the experiments. First we will describe different aspects of the analysis procedure like the fitting routine and how the errors on the fit results are obtained. This will be done for the 2006/7 experiments. For the 2008 experiment, the use of the RFQ beamcooler/buncher implied certain changes in the determination of the isotope shifts and the acceleration voltage. These changes in analysis procedure will be explained afterwards. Finally, an overview in tables of all results obtained during the different experiments is presented.

5.1 Analysis procedure

5.1.1 Conversion of the spectra

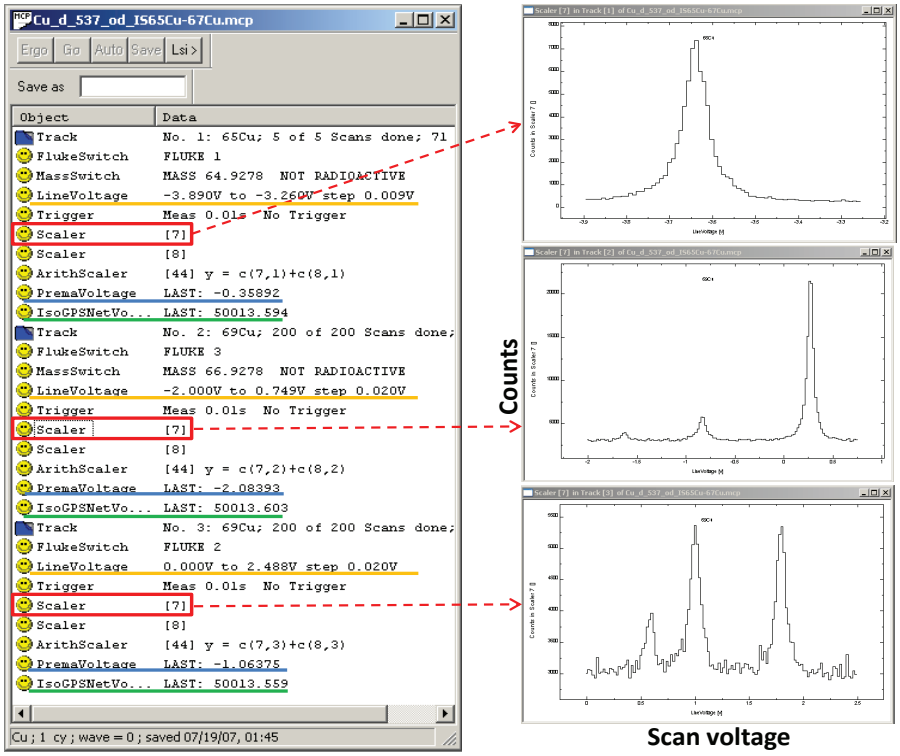

Figure 5.1: A typical MCP file, recorded during the 2007 experiment. There is fast switching between three tracks: in the upper track a peak of ^{65}Cu is monitored in order to measure the isotope shift, and in tracks 2 and 3 the left and right multiplet of the ^{67}Cu hyperfine structure is recorded. Each of these spectra is shown to the right, two scaler channels (red rectangles) communicate the signal of the photomultiplier tubes to the computer. Different values for the scan voltage (orange line) and offset voltage (blue line) can be set for every track. The Isolde voltage is indicated by the green line.

As already explained in the previous chapter, the ions are accelerated by three different voltages, the Isolde voltage V_{Isolde}, the offset voltage V_{offset} and the scan voltage V_{scan} (see equation 4.1). The scan voltage V_{scan} is used to scan across the resonances, while the Isolde voltage V_{Isolde} and the extra offset voltage V_{offset} remain constant during one scan. There are three different power supplies available for the offset voltage, which can be used to fast switch between them. The analysis program which is used to set the scan voltage and monitor the scans is referred to as MCP (Measurement and Control Program). An example of a typical 'raw' data file obtained during a COLLAPS experiment is given in Fig. 5.1. Three different tracks are recorded by fast switching the GPS magnets, a first track monitors a peak of the ^{65}Cu spectrum. Without this reference it would be impossible to determine isotope shifts due to laser and voltage drifts during the experiment. A second and third track monitors the left and right hyperfine structure of ^{67}Cu. Scan voltages are set separately for every track. A switch determines which of the three power supplies is used for the offset voltage. The Isolde voltage is the same for every track, however a non-physical jitter of 0.3V on the readout was observed.

The spectra are recorded as a function of scan voltage. The following step is to convert the scan voltage in the X axis to frequency. The relation between the total acceleration voltage and the transition frequency is given in equations 3.32 and 3.33. The mass of the isotopes used for the conversion is given in table 5.1[85]. With an acceleration voltage of 50kV, the value of β is around 0.0013 for ^{65}Cu. The fundamental frequency of the laser was around 15411.22 cm^{-1} in 2006 and around 15411.64cm^{-1} in 2007. The transition frequency is 9.229 10^8MHz, corresponding to 30783.63 cm^{-1}, or 324.848nm. As the error on the hyperfine parameters is typically a few MHz, this unit is the most convenient to work with. The obtained frequency spectra are usually plotted relative to the center of gravity of the reference isotope.

After converting the spectra as described above, one gets a spectrum like in Fig. 5.2 for ^{65}Cu. The next step is fitting the spectrum in order to extract the parameters containing the nuclear information. This procedure is described below.

Isotope	Mass	Isotope	Mass
^{61}Cu	60.9334578(11)	^{69}Cu	68.9294293(15)
^{62}Cu	61.932584(4)	^{70}Cu	69.9323923(17)
^{63}Cu	62.9295975(6)	^{71}Cu	70.9326768(16)
^{64}Cu	63.9297642(6)	^{72}Cu	71.9358203(15)
^{65}Cu	64.9277895(7)	^{73}Cu	72.936675(4)
^{66}Cu	65.9288688(7)	^{74}Cu	73.939875(7)
^{67}Cu	66.9277303(13)	^{75}Cu	74.9419(10)
^{68}Cu	67.9296109(17)		

Table 5.1: Masses used for the conversion to frequency. Taken from [85].

Fit routine	$A(^2S_{1/2})$ (MHz)
Lorentz one width	6284.3(2)
Lorentz free width	6285.1(3)
Voigt fixed width	6284.2(2)
Lorentz satellite peak	6284.3(2)

Table 5.2: Results for ^{65}Cu using different line shapes. The influence of the lineshape on the results is negligible, except when the width is left as a free parameter for every peak.

5.1.2 The fit routine

The fit routine is a self made ROOT script, based on the well known MINUIT fit package. The positions of the hyperfine structure peaks are restricted based on the known correlation between them, given by equation 3.34.

The most important parameters of the fit are the A factors of the lower and upper state, the B factor of the upper state (the lower state has no quadrupole splitting since it is an S state), and the center of gravity of the structure, which determines the isotope shift. The background of every structure is left as a free parameter, as well as the different peak intensities. In order to determine which lineshape to use and whether to leave the linewidth as a free parameter for every peak, tests were performed on ^{65}Cu using different line shapes. The result is given in Fig. 5.3 and table 5.2. The fit routines include a Lorentzian lineshape where every peak has the same width, a Lorentzian lineshape but where the peak width is a free parameter for every peak, and a Voigt lineshape

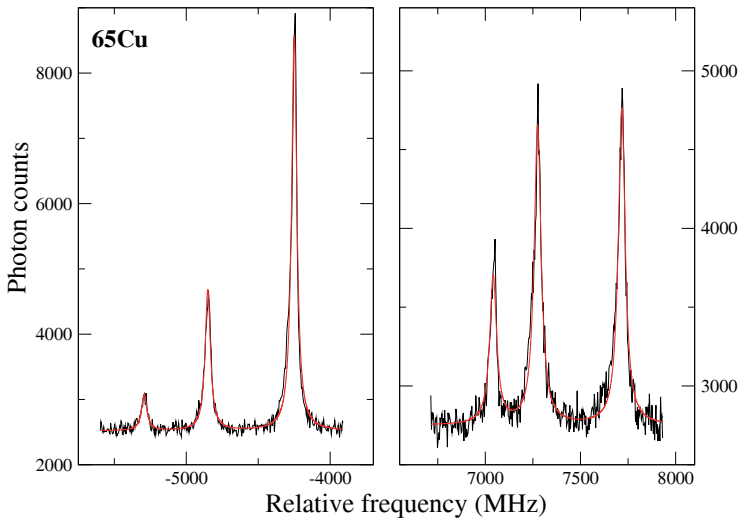

Figure 5.2: Example of a ^{65}Cu hyperfine spectrum converted to frequency.

again with one fixed width. A Lorentzian lineshape with a satellite peak has been considered as well. This satellite peak arises from nonresonant charge exchange in the charge exchange cell. The example given in Fig. 5.2 shows that it is not observed as a separate peak but merely a slight shoulder on the existing peak. The result of the test shows that every lineshape with or without satellite peak yields equivalent results, as long as only one parameter is used for the width of every peak. Indeed it is clear that the results using a Lorentz lineshape with a free width deviate significantly and yield the wrong A factor. Other lineshapes, like a Voigt with a satellite peak or a Voigt with free widths had too many parameters to perform a reliable fit.

In conclusion, a simple Lorentzian lineshape with a fixed width is selected to fit the hyperfine structure spectra. Another option is to fix the ratio of hyperfine parameters $A(^2S_{1/2})/A(^2P_{3/2})$, which is known [86, 87]. This ratio should be constant across the isotope chain in absence of a hyperfine anomaly. The hyperfine anomaly was estimated to be an order of magnitude less than our measurement accuracy for the stable isotopes [88]. Furthermore, a study of hyperfine fields for copper impurities in iron suggests an upper limit of 10^{-3} for the isotopes ^{59,69,71}Cu [**?**].

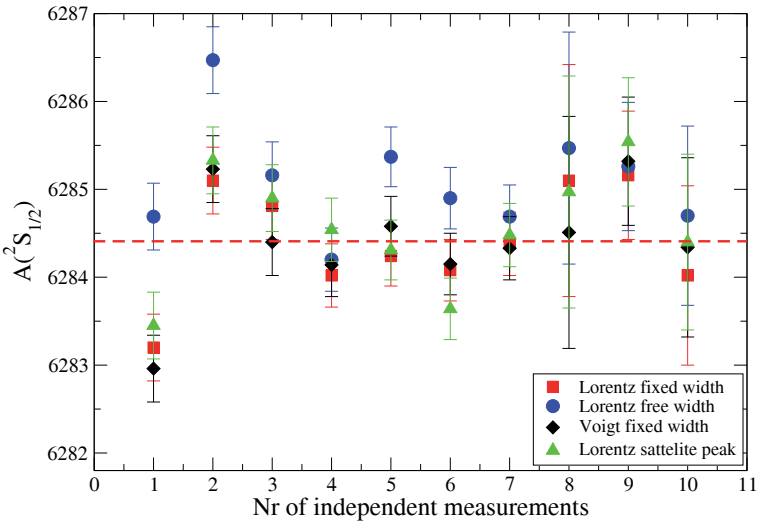

Figure 5.3: A test of different fitting routines on the $A(^2S_{1/2})$ factor of ^{65}Cu. The dashed line corresponds to the literature value of 6284.405(5)MHz [86]. All fitting routines yield equivalent results, except when the width of every peak is left as a free parameter. Hence, the most simple fitting routine, a Lorentzian lineshape with one width for all peaks, is chosen to fit the rest of the hyperfine structure spectra.

We therefore neglect the possible effects of a hyperfine anomaly in the present study. If the ratio of hyperfine parameters is left free, then a deviation of the literature ratio can be used as an argument to assign spin values. For extraction of the A factor and isotope shift, we fix the ratio $A(^2S_{1/2})/A(^2P_{3/2})$. For B parameter determination, the ratio of A factors was left as a free parameter.

5.1.3 Error determination

A and B hyperfine structure parameters

A chi square minimization procedure performed by the MINUIT fit package yields a statistical error on the fit parameters, and a chi square value χ^2 which gives information about the quality of the fit. The statistical error obtained from the fit is multiplied by the square root of the reduced chi square of the fit to get the real statistical error:

$$\sigma_i = \sigma_{fit} \cdot \sqrt{\chi^2_{red}} \tag{5.1}$$

$$\chi^2_{red} = \frac{\chi^2}{d.o.f.} = \frac{\sum_{i=1}^{n}(counts_{fit,i} - counts_{exp,i})^2/\sigma_i^2}{d.o.f.} \tag{5.2}$$

where σ_i is the statistical error on the fit parameter and $d.o.f.$ is the degrees of freedom, given by the number of experimental points minus the number of parameters. Typical values for reduced chi squares range from 1 to 4, depending on the individual measurement. When different *independent* measurements have been performed, the weighted average is taken for the obtained parameters:

$$\mu = \frac{\sum_{i=1}^{n}(x_i/\sigma_i^2)}{\sum_{i=1}^{n}(1/\sigma_i^2)} \tag{5.3}$$

where the errors from the individual spectra σ_i serve as weight factors to calculate the weighted average. Two different errors are considered on the weighted mean: The statistical error, and the error due to the scattering of the fit results. The statistical error can simply be calculated by:

$$\sigma^2_{stat} = \frac{1}{\sum_{i=1}^{n}(1/\sigma_i^2)} \tag{5.4}$$

This error only depends on the size of the error bars of the individual measurements. The error which arises from the scattering of the individual measurements is given by:

$$s^2_{scatter} = \frac{1}{1 - \sum_{i=1}^{n}(1/\sigma^4_{i,norm})} \sum_{i=1}^{n} \frac{1}{\sigma^2_{i,norm}}(x_i - \mu)^2 \tag{5.5}$$

where $s^2_{scatter}$ is called the weighted variance of the sample and $s_{scatter}$ the standard deviance. $\sigma_{i,norm}$ are the normalized error bars so that the weights $(1/\sigma^2_{i,norm})$ sum up to 1. The first factor in $s^2_{scatter}$ is a correction factor which is only significant for cases where few individual measurements are available. The error on the weighted mean is then given by the standard deviation divided by the square root of the number of independent measurements:

$$\sigma_{scatter} = \frac{s_{scatter}}{\sqrt{N}} \tag{5.6}$$

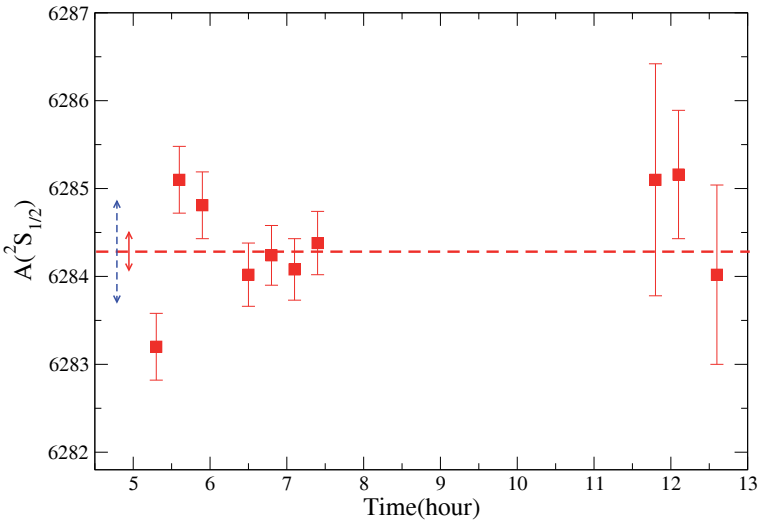

Figure 5.4: The independent measurements of the A($^2S_{1/2}$) factor for ^{65}Cu during the 2006 experiment. The weighted average of 6284.29(19)MHz (dashed line) agrees well with the literature value of 6284.405(5)MHz [86]. The vertical dashed arrow corresponds to the standard deviation $s_{scatter}$, the red full arrow to the error on the weighted average $\sigma_{scatter}$.

In Fig. 5.4 the independent measurements of the A($^2S_{1/2}$) factor of ^{65}Cu during the 2006 experiment are given. The weighted average calculated with equation 5.3 yields A($^2S_{1/2}$)=6284.29MHz. In order to determine the error on this result, we calculate the statistical error with equation 5.4 and the standard deviation with equation 5.5. We get:

$$\begin{aligned} \sigma_{stat}(A^2S_{1/2}(^{65}\mathrm{Cu})) &= 0.13\mathrm{MHz} \\ s_{scatter}(A^2S_{1/2}(^{65}\mathrm{Cu})) &= 0.60\mathrm{MHz} \\ \sigma_{scatter}(A^2S_{1/2}(^{65}\mathrm{Cu})) &= 0.19\mathrm{MHz} \end{aligned}$$

The total error on the A factor of ^{65}Cu is then taken as the maximum of the statistical error and the scattering error. For the ^{65}Cu A factor in 2006 we get:

$$\begin{aligned} \sigma_{tot}(A(^{65}\mathrm{Cu})) = \mathrm{MAX}(\sigma_{\mathrm{stat}}, \sigma_{\mathrm{scatter}}) = 0.19\mathrm{MHz} \\ A^2S_{1/2}(^{65}\mathrm{Cu}) = 6284.29(19)\mathrm{MHz} \end{aligned} \tag{5.7}$$

with σ_{tot} the total error. Usually, the error due to the scattering is smaller than the statistical error. In this case both errors are extremely

small since the high quality ^{65}Cu spectrum was measured repeatedly. For radioactive isotopes however, taking a lot of independent measurements can be very time consuming. In cases where only few independent scans are available, a minimum systematic error on the A factor should be taken into account. The data in Fig. 5.4 illustrate that the standard deviation of the scattering of the ^{65}Cu A factors is 0.6MHz. So for a single radioactive measurement, which is only a snapshot in time, this error should be taken as a minimum error for all data in 2006. We get:

$$\sigma_{tot}(A(^2S_{1/2})) = MAX(\sigma_{stat}, \sigma_{scatter} \text{ or } \mathrm{s_{scatter}}(^{65}\mathrm{Cu})) \tag{5.8}$$

This is how the errors on the A factors are determined. For the B factors, exactly the same procedure is applied.

Isotope shifts

The isotope shift for an isotope X is given by the difference in 'center of gravity' with the reference isotope:

$$IS = c.o.g.(X) - c.o.g.(^{65}\mathrm{Cu}) \tag{5.9}$$

In 2006-2007, the strongest resonance of ^{65}Cu is recorded regularly during every radioactive measurement by fast switching the mass selection of the GPS magnets (see Fig. 5.1). In this way, not only the isotope shift can be determined, also laser frequency or voltage drifts are cancelled out. The isotope shift is then determined by:

$$IS(65, X) = c.o.g.(X) - peak(^{65}\mathrm{Cu}) + \Delta[(\mathrm{peak}^{65}\mathrm{Cu}), \mathrm{c.o.g.}(^{65}\mathrm{Cu})] \tag{5.10}$$

where $\Delta[(peak^{65}\mathrm{Cu}), \mathrm{c.o.g.}(^{65}\mathrm{Cu})]$ represents the distance between the strongest resonance of ^{65}Cu and its center of gravity, equal to 4250.5(2)MHz. The error on the isotope shift in equation 5.10 is taken as a quadratic sum of the following sources of error:

- The statistical error on the center of gravity of the radioactive spectrum.
- The statistical error on the peak of ^{65}Cu.

- Error on $\Delta[(peak^{65}\mathrm{Cu}), \mathrm{c.o.g.}(^{65}\mathrm{Cu})]$.
- Error on the weighted average, calculated in the same way as for the A factors by equations 5.5 and 5.6. In case only one measurement is available, a minimal error of 2MHz is taken.
- Error due to the uncertainty on the voltage calibration.

The second and third errors are usually very small, around 0.5MHz. For the error on the calibration an uncertainty of 2V was taken into account for 2006, and 3V for 2007. The resulting error is mass dependent, corresponding to 0.17% on the isotope shift.

5.1.4 Differences in 2008

Isotope shift determination

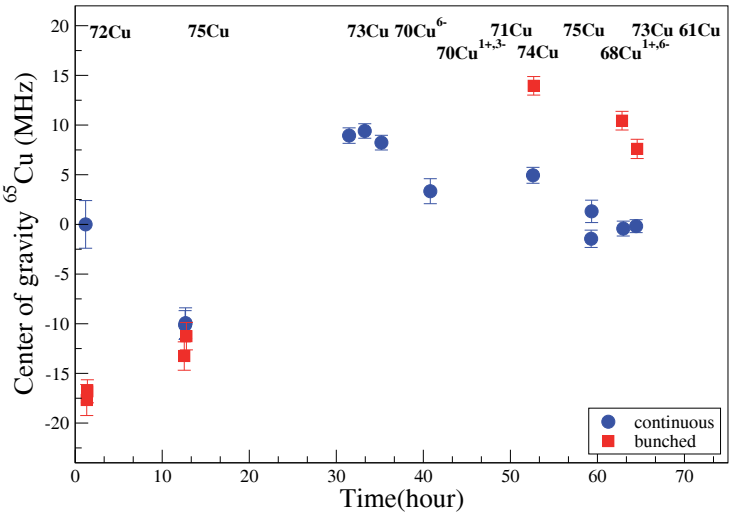

Figure 5.5: Center of gravity of ^{65}Cu, given in frequency relative to an arbitrary reference point, as a function of time. The top of the graph indicates when every isotope was measured. There is no consistent way in which the bunched results scatter with respect to the continuous. Therefore, the continuous spectra are taken as a reference for isotope shift determination.

For the experiment in 2008 the RFQ beamcooler/buncher was used, see section 4.1.5. As a consequence the ions were cooled and reaccelerated by a different voltage V_{ISCOOL}. Using the RFQ beamcooler also implied the use of the 'high resolution separator'(HRS) instead of the 'general purpose separator'(GPS). As the HRS magnets are not able to cycle fast enough, it was no longer possible to record a reference peak in the same file, like the example in Fig. 5.1. Instead, before and after every measurement of a radioactive isotope a spectrum of the ^{65}Cu reference was measured. The center of gravity of the reference measurements is given in Fig. 5.5. The upper part of the figure indicates roughly when every isotope was measured. The isotope shift was determined relative to a time interpolation of the ^{65}Cu c.o.g.'s before and after the radioactive scan. The error on the isotope shift is now taken as the quadratic sum

of the following contributions:

- The statistical error on the radioactive center of gravity.
- The statistical error on the ^{65}Cu center of gravity.
- The frequency difference between the time interpolation and the closest ^{65}Cu measurement.
- Error on the weighted average, in case few independent scans are available a minimum of 2MHz is taken.
- Error due to the uncertainty on the voltage calibration.

Also the comparison between continuous and bunched spectra is seen in Fig. 5.5. There doesn't seem to be a consistent way in which the bunched center of gravity scatters with respect to the continuous. This inconsistency could be due to overloading the trap, however it is not entirely understood. In addition, the scattering of the bunched c.o.g.'s is larger while there is less data available. Therefore, the continuous ^{65}Cu spectra were always taken as a reference to determine the isotope shift.

Voltage determination

As seen in section 4.1.6, different voltage calibrations of the ISCOOL voltage have been performed, which yielded inconsistent results. However, the voltage is an essential parameter for extracting reliable physical information. In this section we will explain how this voltage problem is dealt with.

Initially, the data were analyzed using the second calibration of Fig. 4.6, which was at that time believed to be the correct one. The results are given in Fig. 5.6. A clear discrepancy was observed when comparing the isotope shifts of 2008 and 2006/7. Also, the A factor of ^{65}Cu scattered consistently around the wrong value. Two options are considered to explain the inconsistency for the isotope shifts:

- The voltage calibration could be wrong.
- As we take the bunched spectra as a reference, we compare bunched radioactive measurements with the continuous reference. Possibly, the ions are not cooled sufficiently in continuous mode and hence are extracted with a larger energy.

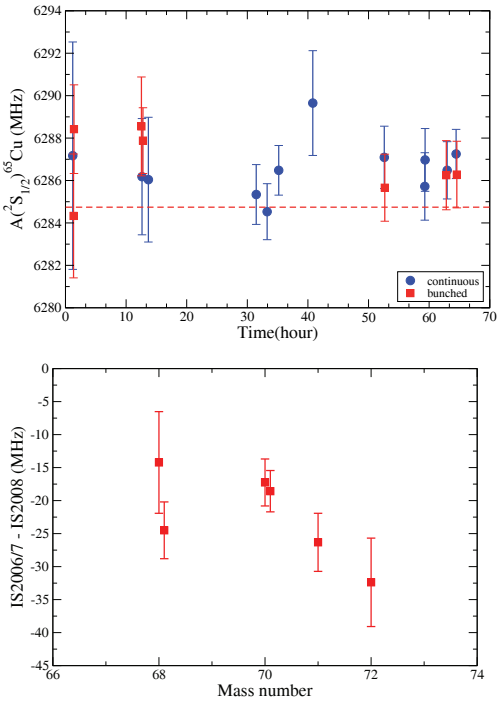

Figure 5.6: The A factors of the ^{65}Cu clearly scatter around the wrong value. The average is 6286.4(5)MHz for the continuous and 6286.7(7)MHz for the bunched spectra, in clear discrepancy with the literature value of 6284.405MHz [86]. Also the isotope shifts are not in agreement with the isotope shifts determined in 2006/2007. These discrepancies are attributed to an incorrect voltage calibration.

The first option is supported by the performed calibrations of the Isolde voltage divider, which all failed to reproduce. The second option could be the cause of deviating isotope shifts, but it cannot explain the deviation on the A factors. For these reasons, the first option is believed to be the correct one. In order to determine the correct voltage, the data were reanalyzed with a different value of the acceleration voltage that removed the inconsistency on the isotope shifts. The result is given in Fig. 5.7. The new Isolde voltage is chosen so that the weighted average of the difference in isotope shifts between 2006/7 and 2008 is now zero. A value of 30021(7)V was adopted. The error corresponding to the 7V

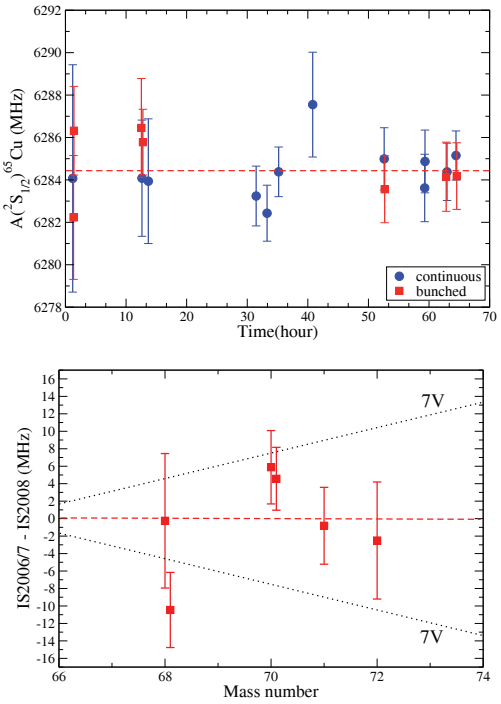

Figure 5.7: (bottom) The correct voltage was determined to be 30221(7)V based on the isotope shift analysis, which now overlaps the measured data with previous years. The dotted lines represent the mass-dependent error on the isotope shifts due to the uncertainty of 7V. The A factors of ^{65}Cu are now 6284.3(8)MHz, in excellent agreement with the literature value of 6284.405MHz [86].

uncertainty is given by the dotted lines, increasing towards the more exotic isotopes. The A factors of ^{65}Cu now scatter perfectly around the literature value, illustrating the validity of the approach presented.

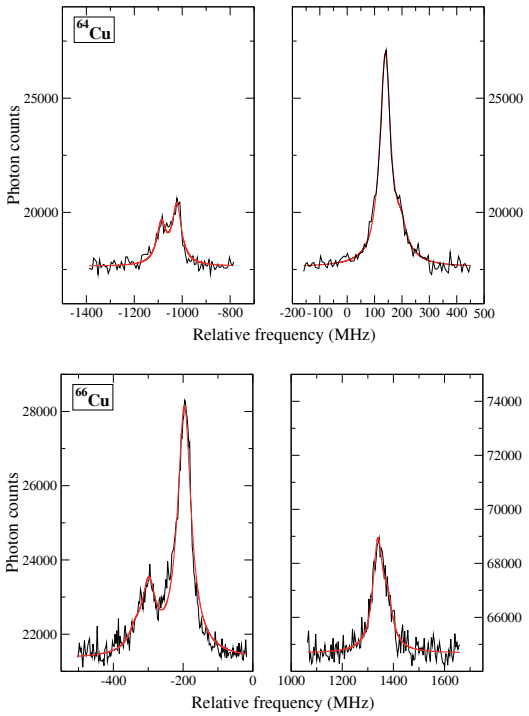

Figure 5.8: Hyperfine structure for ^{64}Cu and ^{66}Cu.

5.2 Some specific examples

5.2.1 ^{64}Cu-^{66}Cu: Magnetic moment sign determination

Previous sections explained how the magnitude of A and B factors is extracted from the laser spectroscopy data. But not only the magnitude of these parameters is obtained, also the sign can be unambiguously determined. If the sign of the hyperfine structure parameter A is reversed, the ordering of the hyperfine structure levels also reverses according to equation 3.34. The impact on the hyperfine spectrum is given in Fig. 5.8. Clearly, the largest peak is on the right side for ^{64}Cu, which means a negative magnetic moment, and on the left side for ^{66}Cu, which has a positive magnetic moment. For ^{66}Cu, the sign of the magnetic moment was previously incorrectly assigned in the literature.

5.2.2 Measurements on the ($^2S_{1/2}$)-($^2P_{1/2}$) transition

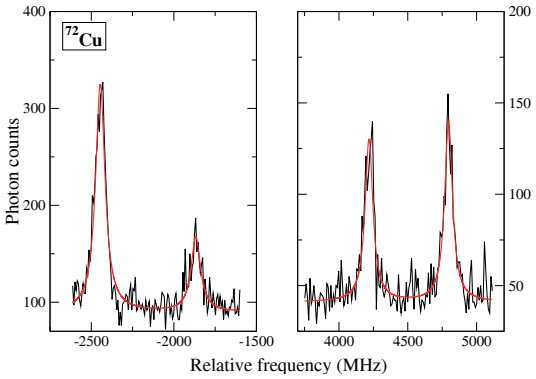

Figure 5.9: Full hyperfine spectrum of ^{72}Cu for the $^2S_{1/2}$-$^2P_{1/2}$ transition.

Previous results have always been measured using the $^2S_{1/2}$-$^2P_{3/2}$ transition. However, it is also possible to use the $^2S_{1/2}$-$^2P_{1/2}$ transition. The reason why the $^2S_{1/2}$-$^2P_{3/2}$ transition is preferred for collinear laser spectroscopy is that it allows extraction of the quadrupole information. On the other hand, the hyperfine spectrum of the $^2S_{1/2}$-$^2P_{1/2}$ transition has only 4 peaks, which makes it more efficient for in-source experiments, as their resolution is anyway too low to extract quadrupole moments. In laser spectroscopy experiments, measurements with the $^2S_{1/2}$-$^2P_{1/2}$ transition can be used to have an independent measurement of the A($^2S_{1/2}$) factor. In this way, there can be no doubt about the spin assignment. The initial goal of changing the laser frequency to the $^2S_{1/2}$-$^2P_{1/2}$ transition was to fix the spin of ^{75}Cu. However, due to proton and laser problems there was not enough time left to scan ^{75}Cu, so a number of less exotic isotopes were measured. An example is given for ^{72}Cu in Fig. 5.9.

5.2.3 New spin determinations

In this section, paper I and II are inserted.

Nuclear spins and magnetic moments of ^{71,73,75}Cu: inversion of $\pi p_{3/2}$ and $f_{5/2}$ levels in ^{75}Cu

K. T. Flanagan,[1,2] P. Vingerhoets,[1] M. Avgoulea,[1] J. Billowes,[3] M. L. Bissell,[1] K. Blaum,[4] B. Cheal,[3] M. De Rydt,[1] V. N. Fedosseev,[5] D. H. Forest,[6] Ch. Geppert,[7,8] J. Krämer,[9] A. Krieger,[9] U. Köster,[10] M. Kowalska,[11] K. L. Kratz,[9] E. Mané,[3] B. A. Marsh,[5] T. Materna,[10] L. Mathieu,[12] P. L. Molkanov,[13] R. Neugart,[9] G. Neyens,[1] W. Nörtershäuser,[9,7] J. Rikovska Stone,[14,15] M. D. Seliverstov,[13,16] O. Serot,[12] M. Schug,[4] M. A. Sjoedin,[17] N. J. Stone,[14,15] H. H. Stroke,[18] G. Tungate,[6] D. T. Yordanov,[4] and Yu. M. Volkov[13]

[1]*Instituut voor Kern- en Stralingsfysica, K. U. Leuven, Celestijnenlaan 200D, B-3001 Leuven, Belgium*
[2]*I.P.N. Orsay, F-91940 Orsay Cedex, France*
[3]*School of Physics and Astronomy, The University of Manchester, Manchester, M13 9PL, UK*
[4]*Max-Planck-Institute für Kernphysik, D-69117 Heidelberg, Germany*
[5]*Engineering Department, CERN, CH-1211 Geneva 23, Switzerland*
[6]*School of Physics and Astronomy, The University of Birmingham, Birmingham, B15 2TT UK*
[7]*GSI Helmholtzzentrum für Schwerionenforschung GmbH, D-64291 Darmstadt, Germany*
[8]*Physikalisches Institut, Universität Tübingen, D-72076 Tübingen, Germany*
[9]*Institut für Kernchemie, Universität Mainz, D-55128 Mainz, Germany*
[10]*Institut Laue Langevin, 6 rue Jules Horowitz, F-38042 Grenoble Cedex 9, France*
[11]*Physics Department, CERN, CH-1211 Geneva 23, Switzerland*
[12]*CEA Cadarache, DEN/DER/SPRC/LEPh F-13108 Saint Paul lez Durance, France*
[13]*Petersburg Nuclear Physics Institute, RU-188300 Gatchina, Russia*
[14]*Department of Physics and Astronomy, University of Tennessee, Knoxville, Tennessee 37996, USA*
[15]*Oxford Physics, University of Oxford, Oxford OX1 3PU, UK*
[16]*Institut für Physik, Universität Mainz, D-55099 Mainz, Germany*
[17]*KTH-Royal Institute of Technology, SE-10044 Stockholm, Sweden*
[18]*Department of Physics, New York University, New York, NY 10003, USA*

We report the first confirmation of the predicted inversion between the $\pi 2p_{3/2}$ and $\pi 1f_{5/2}$ nuclear states in the $\nu g_{9/2}$ mid-shell. This was achieved at the ISOLDE facility, by using a combination of in-source laser spectroscopy and collinear laser spectroscopy on the ground states of ^{71,73,75}Cu, which measured the nuclear spin and magnetic moments. The obtained values are $\mu(^{71}\mathrm{Cu}) = +2.2747(8)\mu_N$, $\mu(^{73}\mathrm{Cu}) = +1.7426(8)\mu_N$, and $\mu(^{75}\mathrm{Cu}) = +1.0062(13)\mu_N$ corresponding to spins $I = 3/2$ for ^{71,73}Cu and $I = 5/2$ for ^{75}Cu. The results are in fair agreement with large-scale shell-model calculations.

PACS: 21.10.Ky 21.10.Pc 21.10.Hw 27.50.+e 32.10.Fn 42.61.Fi

Much of the current effort in nuclear physics is focussed on determining how the nuclear shell structure is changing in neutron-rich nuclei. This has been triggered by the observation of unexpected phenomena in several neutron-rich isotopes, once radioactive ion beams of such nuclei became available more than three decades ago. In the lighter elements (e.g. He, Li, Be) neutron halos and skins were observed. Around the neutron-rich ^{32}Mg region an "island of inversion" was discovered. In the neutron-rich region towards doubly-magic ^{78}Ni, a sudden drop in the position of the first excited $5/2^-$ state in ^{71,73}Cu isotopes was observed more than a decade ago [1]. The lowering of the $5/2^-$ energy from above 1 MeV in ^{69}Cu to 166 keV in ^{73}Cu suggested that this state might become the ground state in ^{75}Cu. The migration of this level, associated with the occupation of the $\pi 1f_{5/2}$ single-particle orbital, was attributed to a strong attractive monopole interaction that becomes active when neutrons occupy the $\nu 1g_{9/2}$ orbital [2]. Such monopole interactions exist also in near-stable nuclei, but their impact on the evolution of shell structure and shell gaps in far-from-stability nuclei remained unnoticed until recently [3]. Also in other neutron-rich regions dramatic monopole shifts were observed when valence neutrons and protons are occupying orbits having their orbital and spin angular momentum respectively aligned and anti-aligned. It is now understood that one of the physics mechanisms driving these monopole shifts is the tensor part of the residual nucleon-nucleon interaction [4]. A steep lowering of the $1/2^-$ level from about 1 MeV in ^{69}Cu down to 135 keV in ^{73}Cu has also been observed [5, 6]. Thus this level is also a potential ground-state candidate in ^{75}Cu. While most shell-model interactions do reproduce a lowering of the $5/2^-$ level and predict an inversion with the normal $3/2^-$ ground state somewhere between ^{73}Cu and ^{79}Cu [4, 7–10], none of them reproduces the lowering of the $1/2^-$ state. Some significant physics mechanism is either omitted or seriously underestimated in each of the recently developed shell-model interactions. Therefore, experimental establishment of ground- and excited-state

nuclear spins and the properties of their wave function (through spectroscopic factors, magnetic moments, transition moments, ...) is a crucial step in the study of the shell evolution. In ^{75}Cu two microsecond isomeric states have been observed below 130 keV [11], but their structure was never interpreted. Knowing the ground-state spin is crucial for assigning spins to these isomeric levels in order to investigate a further lowering of the $5/2^-$ and $1/2^-$ levels as the $\nu 1g_{9/2}$ gets half filled. Comprehensive understanding of the evolution of the low-energy structure is important for the development of robust nucleon-nucleon interactions that can be more widely applied in broad regions of the nuclear chart.

This Letter reports on in-source [12, 13] and collinear [14] laser spectroscopy measurements of the hyperfine structure (hfs) of neutron-rich Cu isotopes up to ^{75}Cu, from which the nuclear ground-state spins I and magnetic moments μ are determined. The radioactive ^{71,73,75}Cu isotopes were produced at the ISOLDE facility using far-asymmetric fission reactions induced by 1.4 GeV protons on a thick uranium carbide target (45 g/cm^2). The radioactive atoms diffused out of the target to a thin ionizer tube. Both target and tube were heated to approximately 2000 °C to reduce transport time. The RILIS (Resonance Ionization Laser Ion Source) was used to stepwise resonantly laser ionize the atoms within the ionizer tube. A two-step ionization scheme used the 327.4 nm $^2S_{1/2} - {}^2P_{1/2}$ transition followed by the 287.9 nm $^2P_{1/2} - {}^2D_{3/2}$ transition to an autoionizing state [12]. For the in-source spectroscopy stage of this work, the first step RILIS laser was operated in a narrow bandwidth (1.2 GHz) mode [13], allowing the $^2S_{1/2}$ hyperfine splitting of ^{75}Cu to be resolved. The resonantly produced ^{75}Cu ions were accelerated to 30 keV and mass separated. They were implanted into the Mainz neutron long counter where their β-delayed neutron emission was detected. This provided excellent discrimination against the ^{75}Ga isobaric contamination, since the β-delayed neutron channel is absent there. The $^2S_{1/2}$ hfs was measured by recording the neutron rate as a function of the first-step laser frequency. The observed splitting in the hfs (upper section of Fig.1) equals $A(^2S_{1/2})(I + 1/2)$, with the hyperfine A factor depending on the nuclear g factor. Fitted as described in [15] and used in [16], these data showed a preference for I = 5/2 and yielded a value $A(^2S_{1/2}) = 1.55(7)$ GHz. With the ^{65}Cu reference values given further, this corresponds to a moment of $0.99(4)\mu_N$. These results greatly reduced the scanning region for the high-resolution collinear laser spectroscopy measurements.

The second stage of this experiment used the collinear laser spectroscopy setup [14] to perform high-resolution studies which allowed both the atomic ground- and excited-state hyperfine structures of ^{71,73,75}Cu to be resolved. With the recent installation of a linear gas-filled radiofrequency quadrupole (RFQ) Paul trap (named ISCOOL) [17, 18], radioactive ions can be cooled and bunched at ISOLDE. Its application for collinear laser spectroscopy has been

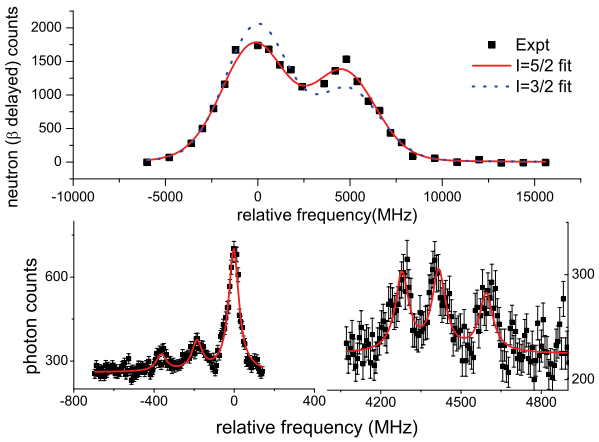

Figure 1: (Color on-line) In-source and collinear laser spectroscopy hfs spectra for ^{75}Cu. Top: in-source spectrum showing the best fits for $I = 3/2$ and $I = 5/2$ using the resonant ionization model [15]. Bottom: resonance fluorescence spectra of ^{75}Cu with best fit for $I = 5/2$. The left and right spectra are separated by the ground-state hfs, observed as two peaks in the upper spectrum.

demonstrated in Jyväskylä (Finland) where rare isotopes with yields down to 150 s^{-1} have been studied with fluorescent photon detection on a bunched ion beam [19, 20]. The ISCOOL device is located after the high-resolution separator (HRS) on a high-voltage platform floated at 30 kV. A trapping potential was applied for up to 100 ms to the end plate of ISCOOL while radioactive ions were collected. Then, by fast-switching the end plate to the platform voltage, the ionic ensemble is released as a bunch with a typical time width of 25 μs. In a continuous mode, where the end plate was held at the platform voltage, a transmission efficiency through the device of 70% has been observed. The ion bunch was transported to the collinear laser spectroscopy beam line where the laser beam was overlapped in the co-propagating direction. The Cu^+ bunch was sent through a sodium vapour cell, heated to approximately 230 °C, which neutralized the ions through charge-exchange collisions. A voltage was applied to the vapour cell for tuning the velocity of the ions and bringing them onto resonance with the laser. The resonances were located by measuring the photon yield as a function of the tuning voltage with two photomultiplier tubes (PMT). The signal from the PMT was gated so that photons were recorded only when an atom bunch was within the light collection region. This reduced the background photon counts associated with scattered laser light by a factor

Table I: Summary of the measured nuclear ground-state spins, magnetic moments and hyperfine parameters. The magnetic moment of ^{71}Cu agrees well with previous β-NMR measurements $\mu = 2.28(1)$ [21].

Isotope	I	μ_{exp} (μ_N)	$A(^2S_{1/2})$ (MHz)	$A(^2P_{3/2})$ (MHz)	$B(^2P_{3/2})$ (MHz)
^{71}Cu	3/2	+2.2747(8)	+6002(2)	+199.6(8)	-25.3(14)
^{73}Cu	3/2	+1.7426(8)	+4598(2)	+152.4(3)	-26.5(10)
^{75}Cu	5/2	+1.0062(13)	+1593(2)	+53.0(9)	-36(2)

4×10^3, this being the ratio of the trapping time to the temporal length in the light collection region. A dye laser was locked to a laboratory frame wavenumber of 15406.9373 cm^{-1} using frequency modulation saturation spectroscopy of iodine. The fundamental wavelength was frequency doubled using an external build-up cavity.

In the lower panel of Fig. 1 the high-resolution hfs data are shown for ^{75}Cu, scanned over the $^2S_{1/2}$– $^2P_{3/2}$ transition (324.8 nm). The number of hfs transitions and their relative splitting depends on the nuclear spin I and the atomic ground- and excited-state hyperfine parameters. Since more than three hyperfine components are observed, a nuclear spin $I = 1/2$ is excluded. The nuclear spins of the ^{71,73,75}Cu isotopes were determined by finding the best fit for their hyperfine parameters, assuming nuclear spins $I = 3/2$, 5/2, and 7/2. For each tentative spin, the fitted ratios $A(^2S_{1/2})/A(^2P_{3/2})$ are compared to those of the stable ^{63,65}Cu isotopes in Fig. 2. Ignoring the negligibly small hyperfine anomaly [22], their ratio has to be constant across the isotope chain independent of the nuclear spin. In ^{71,73}Cu the ratio for $I = 3/2$ is consistent with the stable isotope ratio. In ^{75}Cu the ratio for $I = 3/2$ deviates by 5σ from the observed trend while the ratio for $I = 5/2$ is consistent with it. A summary of A and B factors is shown in Table I. The magnetic moments are deduced relative to ^{65}Cu, using $A(^2S_{1/2}) = +6284.405(5)$ MHz and $\mu(^{65}\text{Cu}) = +2.3817(3)\mu_N$ [23]. Quadrupole moments can be deduced from the B factors, and these will be discussed in a forthcoming paper.

The odd-A Cu isotopes have a simple structure, with one proton outside the $Z = 28$ closed shell. Their ground states with $I^\pi = 3/2^-$ up to ^{71}Cu, are dominated by the $\pi 2p_{3/2}$ odd-proton configuration, as deduced from their measured magnetic moments [21]. The same ground state spin/parity has been suggested for ^{73}Cu based on β-decay studies [2]. No prior spin assignment was made for ^{75}Cu. In this work we have established firm ground-state spins up to ^{75}Cu, illustrating the inversion from $I = 3/2$ to $I = 5/2$ in ^{75}Cu (upper panel of Fig. 3). With our spin/parity 5/2 for the ^{75}Cu ground state, we can assign

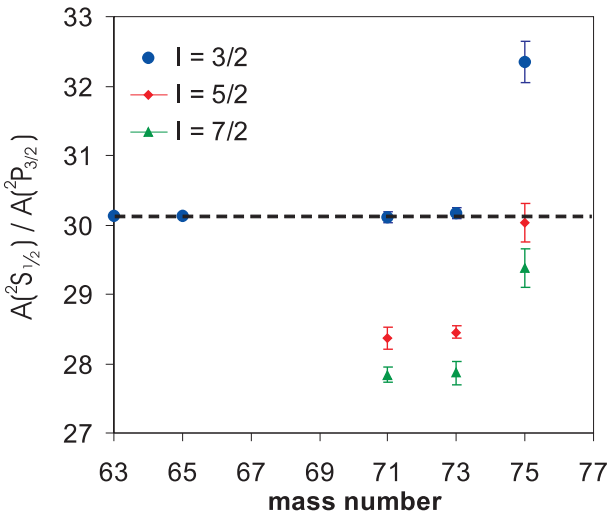

Figure 2: (Color on-line) Ratio of atomic g.s. and excited state A factors deduced from a best fit to the experimental hyperfine spectra, assuming different spins for the ^{71,73,75}Cu nuclear ground states.

tentatively spins and parities to the lowest levels. The levels at 62 and 128 keV are isomeric [11] and from their half-lives and γ-decay properties the multipolarity of the 62 keV and 66 keV γ-transitions was proposed to be most probably of mixed $E2/M1$ character. We therefore assign the level ordering $5/2^-$ (this hfs measurement), $3/2^-$, and $1/2^-$. This implies that the $\pi 2p_{3/2}$ and $\pi 1f_{5/2}$ single-particle levels are nearly degenerate at $N = 46$. It will be very interesting to study the excited states in the odd-odd Cu isotopes, where the coupling with the odd-neutron makes the level ordering very sensitive to the ordering of the proton single-particle levels.

Fig. 3 also presents the calculated level schemes [24] based on an effective shell-model interaction fitted to experimental data in the region, as described in [8, 9]. The calculation is performed in the fpg model space with ^{56}Ni as a core. The migration of the $5/2^-$ state in $^{69-75}$Cu and the inversion with the $3/2^-$ is correctly predicted. However, the lowering of the $1/2^-$ level is significantly underestimated in all of the available shell-model interactions for this region [4, 7–10]. While the migration of the $5/2^-$ state is understood and explained in terms of the tensor interaction between nucleons in the $\pi 1f_{5/2}$ and $\nu 1g_{9/2}$ orbitals [4], the dramatic migration of the $1/2^-$ state requires an alternative mechanism. A hint can be found by comparing the experimental and theoretical magnetic moments (Fig. 4). An effective single-nucleon g_s-factor ($g_s = 0.7 g_{s\text{free}}$) is used which closely reproduces the ^{69}Cu value [25]. An

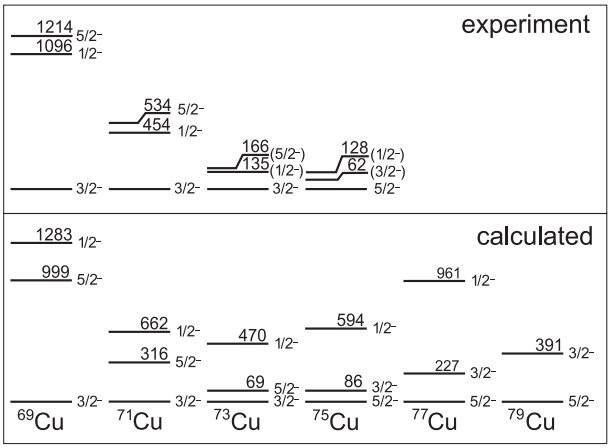

Figure 3: Energy of the lowest levels from experiment [2, 5, 6] compared to large-scale shell-model calculation [24].

increasing deviation between theory and experiment is found towards ^{73}Cu. A possible explanation could be an enhanced collectivity in the $3/2^-$ g.s. which is not properly accounted for. However, the small B(E2) values for the $5/2^-$ decay to the $3/2^-$ ground states in ^{71,73}Cu [5] suggest that these ground states are not extremely collective. In the present calculation a significant part (30%) of the ^{73}Cu wave function contains a coupling to $\nu(2^+, 4^+)$ vibrational excitations, with 83% of the protons in the $\pi 2p_{3/2}$ orbital. The overestimation of the calculated ^{73}Cu moment is more likely related to the overestimated $1/2^-$ energy. Indeed, a lowering of the $\pi 2p_{1/2}$ single-particle energy would lower the calculated $1/2^-$ level energy, and would at the same time lead to a larger fraction of the $p_{1/2} \otimes \nu(2^+)$ configuration in the ground-state wave function. This would significantly lower the calculated magnetic moment.

The shell-model magnetic moment for ^{75}Cu compares closely with its experimental value. The ground-state wave function of ^{75}Cu is dominated by a proton in the $\pi 1f_{5/2}$ orbital (90%) yet with a significant fraction of the wave function coupled to the $\nu(2^+)$ vibrational excitations (36%). The rather collective nature of the ground state is further highlighted by the deviation from the effective Schmidt estimate of the magnetic moment (Fig. 4).

In summary the magnetic moments and spins of ^{71,73,75}Cu have been measured using a combination of collinear and in-source laser spectroscopy. A further lowering of the $5/2^-$ energy is established as it becomes the g.s. in ^{75}Cu. The g.s. spin and magnetic moment of ^{75}Cu are very well reproduced by a large-scale shell-model calculation based on a ^{56}Ni core. With a spectroscopic factor of 90% for the $\pi 1f_{5/2}$ orbit, the inversion between the $\pi 1f_{5/2}$ and

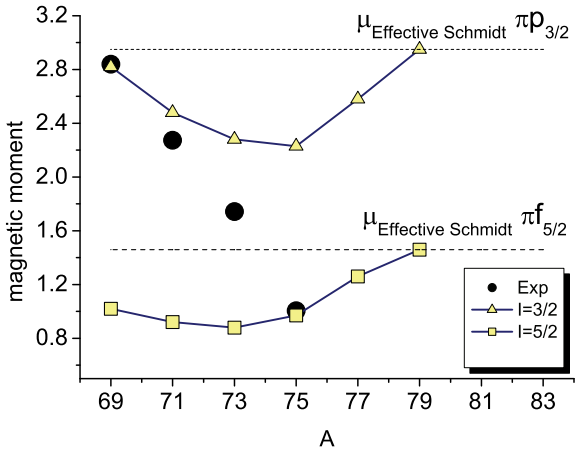

Figure 4: (Color on-line) Comparison of experimental $3/2^-$ and $5/2^-$ magnetic moments with shell-model calculations and effective Schmidt estimates using $g_{\text{effective}} = 0.7 g_{\text{free}}$ [24].

.

$\pi 2p_{3/2}$ single-particle states in ^{75}Cu is established. Tentative spin assignments are made to the isomeric levels in ^{75}Cu, suggesting a further lowering of the $1/2^-$ energy as well. This trend is not reproduced by the current shell-model interactions. Also the calculated $3/2^-$ magnetic moments of ^{71,73}Cu are deviating progressively from the experimental value. These features together may indicate an underlying mechanism not well accounted for in the present shell-model interactions and call for further theoretical and experimental studies to investigate which are the physics mechanisms driving the evolution of the proton single-particle levels as the doubly-magic ^{78}Ni is approached.

This work has been supported by the German Ministry for Education and Research (BMBF) under Contract No. 06TU263I and 06MZ215, the UK Science and Technology Facilities Council, the FWO-Vlaanderen (Belgium), the EU Sixth Framework through No. Eurons-506065, the BriX IAP Research Program No. P6/23 (Belgium) and the Helmholtz Association of German Research Centres (VH-NG-037 and VH-NG-148). M. Kowalska was supported by the EU (MEIF-CT-2006-042114). We would like to thank the ISOLDE

technical group for their support and assistance.

[1] S. Franchoo et al., Phys. Rev. Lett. **81**, 3100 (1998).
[2] S. Franchoo et al., Phys. Rev. C **64**, 054308 (2001).
[3] T. Otsuka et al., Phys. Rev. Lett. **87**, 082502 (2001).
[4] T. Otsuka et al., Phys. Rev. Lett. **95**, 232502 (2005).
[5] I. Stefanescu et al., Phys. Rev. Lett. **100**, 112502 (2008).
[6] I. Stefanescu et al., Phys. Rev. C **79**, 044325 (2009).
[7] N. A. Smirnova et al., Phys. Rev. C **69**, 044306 (2004).
[8] A. F. Lisetskiy et al., Phys. Rev. C **70**, 044314 (2004).
[9] A. F. Lisetskiy et al., Eur. Phys. J. A **25, s01**, 95 (2005).
[10] M. Honma et al., Phys. Rev. C , submitted (2009).
[11] J. M. Daugas, Ph.D. thesis, Caen University (1999).
[12] U. Köster et al., Nucl. Instr. Meth. B **160**, 528 (2000).
[13] V. N. Fedosseev et al., Nucl. Instr. Meth. B **204**, 353 (2003).
[14] A. Mueller et al., Nucl. Phys. A **403**, 234 (1983).
[15] S. Gheysen et al., Phys. Rev. C **69**, 064310 (2004).
[16] N. Stone et al., Phys. Rev. C **77**, 067302 (2008).
[17] H. Frånberg et al., Nucl. Instr. Meth. B **266**, 4502 (2008).
[18] E. Mané et al., Eur. Phys. J. A , DOI 10.1140/epja/i2009-10828-0 (2009).
[19] A. Nieminen et al., Phys. Rev. Lett. **88**, 094801 (2002).
[20] M.L. Bissell et al., Phys. Lett. B **645**, 330 (2007).
[21] N. Stone et al., Phys. Rev. C **77**, 014315 (2008).
[22] P. R. Locher, Phys. Rev. B **10**, 801 (1974).
[23] H. Figger et al., Colloq. Intern. CNRS **164**, 355 (1967).
[24] B. A. Brown and A. F. Lisetskiy, (priv. comm.) (2009).
[25] J. Rikovska et al., Phys. Rev. Lett. **85**, 1392 (2000).

Experimental determination of a $I^\pi = 2^-$ ground state in ^{72,74}Cu

K.T. Flanagan,[1,2] P. Vingerhoets,[1] M.L. Bissell,[1] K. Blaum,[3] B.A. Brown,[4] B. Cheal,[5] M. De Rydt,[1] D.H. Forest,[6] Ch. Geppert,[7,8] M. Honma,[9] M. Kowalska,[10] J. Krämer,[11] A. Krieger,[11] E. Mané,[5] R. Neugart,[11] G. Neyens,[1] W. Nörtershäuser,[11,7] M. Schug,[3] H.H. Stroke,[12] and D.T. Yordanov[3]

[1]*Instituut voor Kern- en Stralingsfysica, K. U. Leuven, B-3001 Leuven, Belgium*
[2]*IPN Orsay, F-91940 Orsay Cedex, France*
[3]*Max-Planck-Institute für Kernphysik, D-69117 Heidelberg, Germany*
[4]*National Superconducting Cyclotron Laboratory and Department of Physics and Astronomy, Michigan State University, East Lansing, Michigan 48824-1321, USA*
[5]*School of Physics and Astronomy, University of Manchester, Manchester, M13 9PL, UK*
[6]*School of Physics and Astronomy, University of Birmingham, Birmingham, B15 2TT UK*
[7]*GSI Helmholtzzentrum für Schwerionenforschung GmbH, D-64291 Darmstadt, Germany*
[8]*Physikalisches Institut, Universität Tübingen, D-72076 Tübingen, Germany*
[9]*Center for Mathematical Sciences, University of Aizu, Tsuruga, Japan*
[10]*Physics Department, CERN, CH-1211 Geneva 23, Switzerland*
[11]*Institut für Kernchemie, Johannes Gutenberg Universität Mainz, D-55128 Mainz, Germany*
[12]*Department of Physics, New York University, New York, NY 10003, USA*

This paper reports on the ground state spin and moments measured in ^{72,74}Cu using collinear laser spectroscopy at the ISOLDE facility. From the measured hyperfine coefficients, the nuclear observables $\mu(^{72}\text{Cu}) = -1.3472(10)\mu_N$, $\mu(^{74}\text{Cu}) = -1.068(3)\mu_N$, $Q(^{72}\text{Cu}) = +8(2)$ efm^2, $Q(^{74}\text{Cu}) = +26(3)$efm^2, $I(^{72}\text{Cu}) = 2$ and $I(^{74}\text{Cu}) = 2$ have been determined. Through a comparison of the measured magnetic moments with different models, the negative moment reveals a strong $\pi f_{5/2} \otimes \nu g_{9/2}$ component in the ground-state wave function. Consequently a negative parity has been assigned to the ground states of ^{72,74}Cu. Large scale shell-model calculations illustrate the strong sensitivity of the nuclear moments to configuration mixing and to the used effective

interaction.

PACS:21.10.Ky; 21.10.Pc; 21.10.Hw; 27.50.+e

The neutron-rich nuclei surrounding the $Z = 28$ and $N = 50$ shell closures have received a great deal of experimental and theoretical attention in the last decade. This region presents a key proving ground for the latest shell-model interactions, since it offers an attractively simple structure of the excited states in terms of particle-particle or particle-hole couplings. A compelling question in this region is related to the rapid reduction in energy of the $5/2^-$ state as the $\nu g_{9/2}$ orbital is filled in the Cu isotopes [1, 2]. Given that this state remains static at approximately 1 MeV as neutrons fill the fp shell, its abrupt change at $N = 40$ garnered a great deal of interest and motivated further experimental and theoretical attention [3–17]. A major step in understanding the evolution of nuclear structure in this region was the suggestion to include the monopole term from the tensor force interaction [18, 19]. This work predicted a reduction in energy of the $5/2^-$ state and an inversion with the $3/2^-$ state in the mid-shell region, which was recently confirmed to occur at $N = 46$ in the odd-Cu isotopes [20]. Effective shell-model interactions which include this effect have recently been developed in the fpg model space. Two of these interactions start from a ^{56}Ni core [21, 22], while the most recent one includes also excitations of protons from the $\pi f_{7/2}$ orbit across $Z = 28$ [23]. The odd-odd Cu isotopes are an ideal testing ground for these models, as their properties are extremely sensitive to the proton-neutron interaction.

Recent beta-decay studies of ^{72}Ni [8] have tentatively assigned a spin $I = 2$ to the ground state (gs) of ^{72}Cu. Shell-model calculations, based on effective and realistic interactions, could not reproduce such gs spin [8], but placed the 2^- and 2^+ states around 400 keV. A gs spin $I = 2$ is particularly interesting since the spins of ^{71,73}Cu now have been measured as $I = 3/2$ and their magnetic moments are compatible with a leading $\pi p_{3/2}$ configuration [20]. However, a $[\pi p_{3/2} \otimes \nu g^3_{9/2}, \sigma = 1]$ cannot couple to spin 2, so this configuration cannot be the leading term in the gs wave function of ^{72}Cu. Alternatively it could be dominated by $[\pi f_{5/2} \nu g^3_{9/2}]_{2-}$ or $[\pi p_{3/2} \nu p^{-1}_{1/2} \nu g^4_{9/2}]_{2+}$ or a collective $[\pi p_{3/2} \otimes \nu g^3_{9/2}, \sigma = 3]$ configuration. An observable that is particularly sensitive to which configuration dominates the gs wave function, is the magnetic moment. In this paper we report on laser spectroscopy measurements, which have unambiguously measured the gs spin and the nuclear moments of ^{72,74}Cu. From the results, firm conclusions are drawn about the main component in their wave functions and on the parity of their ground states. The experiment used the collinear laser spectroscopy setup [24] at ISOLDE-CERN for high-resolution studies to fully resolve the hfs of ^{72,74}Cu.

Table I: Summary of the measured gs hyperfine parameters of ^{72,74}Cu and deduced magnetic-dipole and electric-quadrupole moments.

Isotope	I	$A(^2S_{1/2})$ (MHz)	$A(^2P_{3/2})$ (MHz)	$B(^2P_{3/2})$ (MHz)	μ_{exp} (μ_N)	Q (efm^2)
^{72}Cu	2	-2666(2)	-89.8(6)	+10(2)	-1.3472(10)	+8(2)
^{74}Cu	2	-2113(5)	-71.6(11)	+34(4)	-1.068(3)	+26(3)

The $^2S_{1/2}-\ ^2P_{3/2}$ transition (324.8 nm) in Cu was used in order to be sensitive to the nuclear spin. The radioactive isotopes were produced using a far-asymmetric fission reaction induced by 1.4 GeV protons on a thick uranium carbide target (45 g/cm^2). The radioactive atoms diffused out of the target to a thin tube, both heated to approximately 2000 °C to reduce transport time. The RILIS laser ion source was used to stepwise resonantly laser ionize the Cu atoms within the ionizer tube [25]. The produced ions were accelerated through 30 kV and mass separated by the high resolution separator (HRS) before they were injected into an RFQ linear gas-filled Paul trap (ISCOOL) [26], which was floated at about 100 V below the ion source acceleration potential. The application of ion cooling and bunching in collinear laser spectroscopy has been demonstrated first in Jyväskylä (Finland) [27]. The ions were trapped in ISCOOL for up to 100 ms and released as a bunch with a temporal width of 25 μs. The ion bunch and laser beam were subsequently overlapped in a co-propagating direction. The ion bunch was neutralized by passing it through a sodium vapour cell, heated to approximately 200 °C. A continuous wave dye laser was locked to a laboratory frame wavenumber of 15406.9373 cm^{-1} and frequency doubled in an external cavity. The atomic fluorescence resonances were located by applying a scanning voltage to the vapour cell and Doppler tuning the ions before neutralization. Two photomultiplier tubes (PMT) were then used to measure the fluorescent photon yield as a function of the tuning voltage (see Fig. 1). By placing a gate on the signal, accepting photons only when an atom bunch was within the light collection region, the background count rate associated with scattered light was reduced by more than three orders of magnitude.

Typical fluorescence spectra for ^{72}Cu and ^{74}Cu are shown in Fig. 2. A χ^2 minimization routine was used to fit Lorentzian profiles to the data, from which the hfs A and B coefficients are obtained for different values of the nuclear spin I. The observation of 6 transitions in both ^{72}Cu and ^{74}Cu immediately excludes $I = 1$ through angular momentum considerations. The ratio of the ground- and excited-state hfs A coefficient remains constant across the Cu isotope chain and is independent of the nuclear spin [20]. This permits a comparison of different

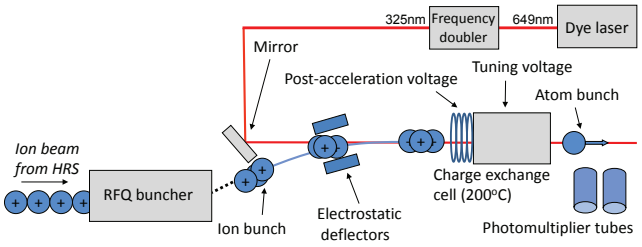

Figure 1: (Color on-line) A schematic of the bunched-beam laser spectroscopy experimental set-up at ISOLDE.

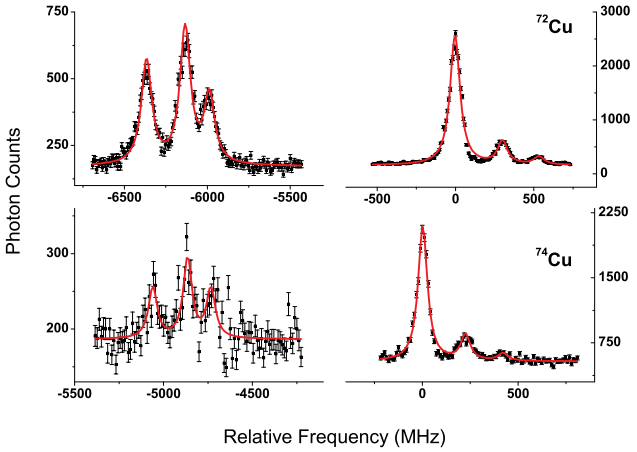

Figure 2: (Color on-line) Resonance fluorescence spectra of ^{72,74}Cu measured using the bunched beam technique that suppresses the background associated with scattered light and dark counts from the PMT.

spin options for ^{72}Cu and ^{74}Cu with the stable isotopes, which is shown in Fig. 3. In both ^{72}Cu and ^{74}Cu a nuclear spin of $I = 2$ results in a ratio that is consistent with the stable isotopes. A nuclear spin of $I = 3$ (or higher) can be excluded with a confidence level of 4σ or higher for both cases. A and B coefficients for $I = 2$, along with deduced moments, are shown in Table I. The moments were deduced relative to ^{65}Cu, using $A(^2S_{1/2}) = 6284.405(5)$ MHz, $B(^2P_{3/2}) = -25.9(6)$ MHz, $\mu(^{65}\text{Cu}) = +2.3817(3)\mu_N$ and $Q(^{65}\text{Cu}) = -19.5(4)$ efm^2 [28–30].

Considering the single particle proton and neutron orbits that play a role in this region, there are three possible configurations of protons and neutrons that

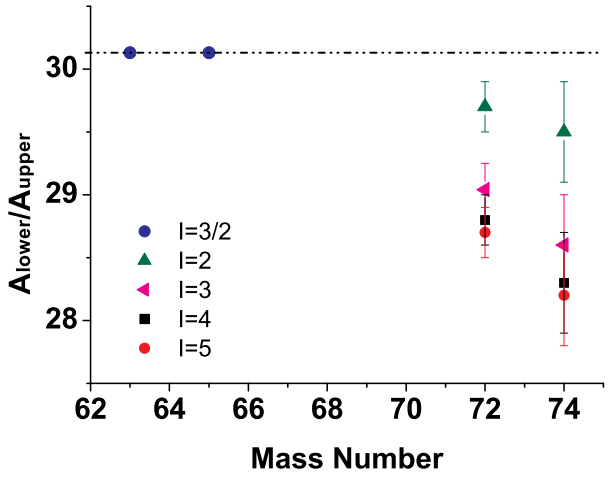

Figure 3: (Color on-line) Plot of the hfs A coefficient ratio of the $^2S_{1/2}$ and $^2P_{3/2}$ states. The values for the stable isotopes ^{63,65}Cu are compared to the values obtained for ^{72,74}Cu using nuclear spin options $I = 2, 3, 4$ and 5 to fit observed spectra.

can couple to form an $I = 2$ state in a seniority 1 scheme: $(\pi f_{5/2} \otimes \nu g_{9/2})_{2^-}$, $(\pi p_{3/2} \otimes \nu p^{-1}_{1/2})_{2^+}$ and $(\pi f_{5/2} \otimes \nu p^{-1}_{1/2})_{2^+}$. Interpretation of the measured magnetic moments can help to determine which of these three options is the leading configuration of the ground state, and consequently what its parity is. Assuming weak coupling of protons and neutrons, and using the additivity rule for moments [32], the magnitude and sign of the magnetic moment for these three configurations is calculated. For the single proton and neutron configurations, respectively free nucleon, effective and empirical moments are used and the results are presented in Table II. Empirical single particle moments are taken as the experimental moments of ^{73}Cu$(3/2^-)$, ^{75}Cu$(5/2^-)$, ^{71}Zn$(9/2^+)$ and ^{67}Ni$(1/2^-)$. Empirical moments of odd-odd isotopes closely agree with their experimental values if the proposed configuration forms the leading term in the wave function. For both of the positive-parity configurations the calculated moments have a positive sign. Therefore the negative sign of the experimental magnetic moment rules out a positive parity gs configuration dominated by a $\nu p_{1/2}$ excited across $N = 40$. Conversely, the sign and magnitude of the calculated empirical moments for the $\pi f_{5/2} \otimes \nu g_{9/2}$ configuration closely matches the measured moments for ^{72,74}Cu, and therefore a negative parity for

Table II: Summary of magnetic moments calculated using the additivity rule for free nucleon moments, effective moments (g_s=0.7g_s^{free}) and empirical moments, which are to be compared to the measured moments for ^{72}Cu(-1.347(1)μ_N) and ^{74}Cu(-1.068(3)μ_N)

Configuration	I	μ_{free} (μ_N)	$\mu_{effective}$ (μ_N)	$\mu_{empirical}$ (μ_N)
$\pi f_{5/2} \otimes \nu g_{9/2}^3$	2^-	-2.13	-2.06	-1.53 ($\langle^{75}$Cu,^{71}Zn$\rangle$)
$\pi p_{3/2} \otimes \nu p_{1/2}^{-1} g_{9/2}^4$	2^+	+4.43	+3.40	+2.35 ($\langle^{73}$Cu, ^{67}Ni$\rangle$)
$\pi f_{5/2} \otimes \nu p_{1/2}^{-1} g_{9/2}^4$	2^+	+0.380	+1.07	+0.536 ($\langle^{75}$Cu, ^{67}Ni$\rangle$)

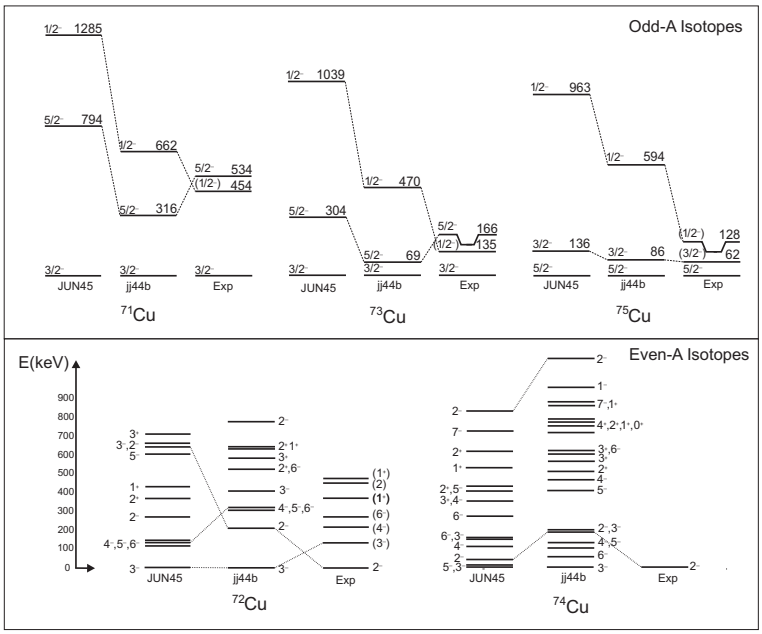

Figure 4: Comparison of the trend in energy of the lowest states between large scale shell-model calculations [21, 22] and experiment [2, 8, 12, 13, 31].

both ground states is proposed.

The parity and the composition of the gs wave function can be further investigated by comparing the measured moments to shell-model calculations. The effective interactions by Brown *et al.* (jj44b) [22] and Honma *et al.* (JUN45) [21]

Table III: Moments from shell-model calculations using the jj44b interaction for the lowest $I^\pi = 2^\pi$ compared to experimental moments.

Isotope	I^π	E(keV)	Leading proton configuration	%	μ (μ_N)	Q (efm^2)
^{72}Cu	2	0			-1.3472(10)	+8(2)
	2^-	**211**	$\pi f_{5/2}$	**72**	**-1.543**	**+15**
	2^-	784	$\pi p_{3/2}$	69	-2.058	-10
	2^+	538	$\pi f_{5/2}$	79	+1.027	-24
	2^+	640	$\pi p_{3/2}$	73	+1.616	-23
^{74}Cu	2	0			-1.068(3)	+26(3)
	2^-	**208**	$\pi f_{5/2}$	**67**	**-1.418**	**+20**
	2^-	1121	$\pi p_{3/2}$	58	-1.409	+11
	2^+	517	$\pi f_{5/2}$	80	+1.098	-18
	2^+	754	$\pi p_{3/2}$	49	+0.045	+21

have been used to perform Large Scale Shell-Model (LSSM) calculations for $^{71-75}$Cu. Both LSSM calculations start from a ^{56}Ni core with a proton and neutrons in the $f_{5/2}pg_{9/2}$ orbits. The calculated energy levels are compared to the experimentally known levels in Fig 4. Neither interaction predicts a gs $I^\pi = 2^+$ or 2^- in ^{72}Cu or ^{74}Cu, but both correctly reproduce the inversion of the $5/2^-$ and $3/2^-$ levels in the odd-Cu chain at ^{75}Cu. The two models predict the main features of the observed low energy level scheme in ^{72}Cu, having a high level density. The low-spin levels in ^{72}Cu have been observed via β-decay from ^{72}Ni [8] and the high-spin levels are seen in the decay from a suggested (6^-) isomer [31]. No data are available for ^{74}Cu. The multiplets of states arising from the coupling of $(\pi p_{3/2} \otimes \nu g_{9/2})_{(3,4,5,6)^-}$ and $(\pi p_{3/2} \otimes \nu p^{-1}_{1/2})_{(1,2)^+}$, responsible for the observed isomerism in ^{68,70}Cu [7, 33, 34], appear at low energy in the calculations for ^{72,74}Cu. The lowest 2^- level appears below 250 keV in both isotopes and with both interactions, while the 2^+ state appears a few 100 keV higher.

The calculated nuclear moments for the two lowest 2^+ and 2^- levels, along with their energy, are summarized in Table III for jj44b and in Table IV for JUN45. Magnetic moments have been calculated using the effective value $g_s = 0.7 g_s^{free}$ and for quadrupole moments the effective charges $e_\pi^{eff} = 1.5e$, $e_\nu^{eff} = 1.1e$ are used for JUNE45 [21] and $e_\pi^{eff} = 1.4e$, $e_\nu^{eff} = 1.0e$ for jj44b [35]. For each level, the occupancy of the leading proton configuration is given. All

Table IV: Moments from shell-model calculations using the JUN45 interaction compared to experiment.

Isotope	I^π	E(keV)	Leading proton configuration	%	μ (μ_N)	Q (efm^2)
^{72}Cu	2	0			-1.3472(10)	+8(2)
	2^-	263	$\pi p_{3/2}$	71	-2.47	-12
	2^-	**645**	$\pi f_{5/2}$	**69**	**-1.42**	**+5**
	2^+	367	$\pi p_{3/2}$	85	+2.29	-15
	2^+	978	$\pi p_{5/2}$	81	+0.76	-25
^{74}Cu	2	0			-1.068(3)	+26(3)
	2^-	**44**	$\pi f_{5/2}$	**63**	**-1.74**	**+15**
	2^-	859	$\pi p_{3/2}$	56	-1.63	+8
	2^+	408	$\pi p_{3/2}$	53	+1.73	-14
	2^+	621	$\pi f_{5/2}$	64	+1.25	-26

positive parity states have a positive magnetic moment, in disagreement with experiment (first line in each table). With the jj44b interaction, the calculated magnetic and quadrupole moment of the lowest 2^- state in ^{72}Cu and ^{74}Cu are in rather good agreement with experiment (bold), confirming that the wave function of these levels, calculated at about 200 keV in both isotopes, is close to the gs wave function. Both are dominated by a proton in the $\pi f_{5/2}$ orbit. The leading neutron term has an odd neutron in the $\nu g_{9/2}$ level, confirming our conclusion based on the weak coupling. With the JUN45 interaction, the lowest 2^- level in ^{72}Cu is dominated by a $\pi p_{3/2}$ and its moments do not agree with the observed values. The second 2^- state, calculated at 645 keV, has moments that both agree very well with the observed values, suggesting that its wave function very well represents the observed gs. Its proton occupation in the $\pi f_{5/2}$ orbit is similar as for the lowest 2^- from jj44b, thus it is small differences in the neutron occupation which lead to a slightly better agreement of the moments with experiment. Note that the calculated energy of this level is about 600 keV too high, which provides information on how to improve on the relative effective single particle proton energies. In the case of ^{74}Cu the agreement is best for the lowest 2^- state, also having a wave function dominated by protons in $\pi f_{5/2}$. In this case, the agreement is better for jj44b than for JUN45. These results show that nuclear moments are a very sensitive probe of the wave function of a nuclear state, allowing a calculated level to be assigned

to an observed state.

The less good agreement for the JUN45 ^{74}Cu moments with experiment might be associated with the $1/2^-$ state in ^{71,73,75}Cu (top of Fig. 4), which is calculated at too high energy. The experimentally observed rapid decrease of the $1/2^-$ energy [16, 20] is reasonably well reproduced with jj44b. Best agreement of the odd-Cu 1/2, 3/2, 5/2 energy levels with experiment has been obtained with a recently published effective interaction that includes excitations of protons across the $N = 28$ shell gap [23]. With this interaction, the steep decrease in the magnetic moments of the $3/2^-$ ground states from ^{69}Cu to ^{73}Cu is also well reproduced. It will be interesting to see how well this interaction reproduces the moments of the odd-odd Cu isotopes, in order to probe the importance of proton excitations in this region.

In conclusion, neither of the shell-model interactions nor the calculations based on the additivity rule for coupling nucleons, predict a $I^\pi = 2^+$ state with a negative magnetic moment for these isotopes. Conversely all the calculations for an $I^\pi = 2^-$ state reported in this paper predict a negative magnetic moment, with a value that is in rather good agreement with the experimentally observed one. Therefore it can be concluded that the ground states of ^{72}Cu and ^{74}Cu both have a negative parity, associated with a dominant $\pi f_{5/2} \otimes \nu g_{9/2}$ configuration. This shows that already from $N = 43$ onwards, the $\pi f_{5/2}$ level is playing a dominant role in the gs wave function of the odd-odd isotopes, due to the strong $\pi f_{5/2} \nu g_{9/2}$ interaction. The LSSM calculations with effective interactions starting from a ^{56}Ni core reproduce the observed magnetic and quadrupole moments reasonably well, but fail to get the 2^- level as the ground state.

This work has been supported by the German Ministry for Education and Research (BMBF) under Contract No. 06MZ215, the UK Science and Technology Facilities Council (STFC), the FWO-Vlaanderen (Belgium), EU Sixth Framework through No. Eurons-506065, BriX IAP Research Program No. P6/23 (Belgium), the Helmholtz Association of German Research Centres(VH-NG-037 and VH-NG-148), the Max-Planck Society and NSF grant PHY-0758099. M. Kowalska was supported by the EU (MEIF-CT-2006-042114). We would like to thank the ISOLDE technical group for their support and assistance during this project.

[1] S. Franchoo et al., Phys. Rev. Lett. **81**, 3100 (1998).
[2] S. Franchoo et al., Phys. Rev. C **64**, 054308 (2001).
[3] A. M. Oros-Peusquens and P. F. Mantica, Nuclear Physics A **669**, 81 (2000).

[4] N. A. Smirnova, A. De Maesschalck, A. Van Dyck, and K. Heyde, Phys. Rev. C **69**, 044306 (2004).
[5] A. F. Lisetskiy, B. A. Brown, M. Horoi, and H. Grawe, Phys. Rev. C **70**, 044314 (2004).
[6] A. Lisetskiy, B. Brown, and M. Horoi, Eur. Phys. J. A **25**, 95 (2005).
[7] J. Van Roosbroeck et al., Phys. Rev. Lett. **92**, 112501 (2004).
[8] J.-C. Thomas et al., Phys. Rev. C **74**, 054309 (2006).
[9] C. Guénaut et al., Phys. Rev. C **75**, 044303 (2007).
[10] S. Rahaman et al., Eur.Phys.J.ST **150**, 349 (2007).
[11] N. J. Stone et al., Phys. Rev. C **77**, 014315 (2008).
[12] I. Stefanescu et al., Phys. Rev. Lett. **100**, 112502 (2008).
[13] I. Stefanescu et al., Phys. Rev. C **79**, 044325 (2009).
[14] N. Patronis et al., Phys. Rev. C **80**, 034307 (2009).
[15] S. V. Ilyushkin et al., Phys. Rev. C **80**, 054304 (2009).
[16] J. M. Daugas et al., Phys. Rev. C **81**, 034304 (2010).
[17] B. Cheal et al., Phys. Rev. Lett. **104**, 252502 (2010).
[18] T. Otsuka et al., Phys. Rev. Lett. **95**, 232502 (2005).
[19] T. Otsuka et al., Phys. Rev. Lett. **104**, 012501 (2010).
[20] K. T. Flanagan et al., Phys. Rev. Lett. **103**, 142501 (2009).
[21] M. Honma, T. Otsuka, T. Mizusaki, and M. Hjorth-Jensen, Phys. Rev. C **80**, 064323 (2009).
[22] B. Brown and A. Lisetskiy, private Communication.
[23] K. Sieja and F. Nowacki, Phys. Rev. C **81**, 061303 (2010).
[24] A. Mueller et al., Nucl.Phys. **A403**, 234 (1983).
[25] U. Köster et al., Nucl. Instr. Meth. B **160**, 528 (2000).
[26] E. Mané et al., Euro. Phys. J. A **42**, 503 (2009).
[27] P. Campbell et al., Euro. Phys. J. A **15**, 45 (2002).
[28] Y. Ting and H. Lew, Phys. Rev. **105**, 581 (1957).
[29] J. Ney, Z. Phys. A **196**, 53 (1966).
[30] P. Raghavan, Atomic Data and Nuclear Data Tables **42**, 189 (1989).
[31] H. Mach, in *Proceedings of the International Symposium on Nuclear Structure Physics* (World Scientific, Singapore, 2001, Göttingen, Germany, 2001), p. 379.
[32] G. Neyens, Reports on Progress in Physics **66**, 633 (2003).
[33] L. Weissman et al., Phys. Rev. C **65**, 024315 (2002).
[34] K. Blaum et al., EPL (Europhysics Letters) **67**, 586 (2004).
[35] P. Vingerhoets et al., To be published (2010).

5.3 Overview results in tables

Isotope	I^π	$A(^2S_{1/2})$(MHz)	$B(^2P_{3/2})$(MHz)	Isotope shift (MHz)
^{63}Cu	$3/2^-$	+5867.40(34)	-28.50(44)	-576.7(15)
^{64}Cu	1^+	-856.6(15)	+9.6(12)	-249.4(22)
^{65}Cu	$3/2^-$	+6284.29(19)	-25.80(27)	
^{66}Cu	1^+	+1117.5(33)	+7.4(17)	+304.8(33)
^{67}Cu	$3/2^-$	+6632.4(11)	-22.7(17)	+556.9(26)
^{68}Cu	1^+	+9478.3(32)	-8.1(29)	+861.0(29)
^{68}Cu	6^-	+761.52(25)	-58.9(31)	+812.6(31)
^{69}Cu	$3/2^-$	+7487.7(19)	-20.5(27)	+1079.3(31)
^{70}Cu	6^-	+901.42(42)	-38.4(43)	+1345.7(28)

Table 5.3: Results from the 2006 experiment.

Isotope	I^π	$A(^2S_{1/2})$(MHz)	$B(^2P_{3/2})$(MHz)	Isotope shift (MHz)
^{62}Cu	1^+	-1511.8(26)	-0.6(28)	-825.0(39)
^{63}Cu	$3/2^-$	+5867.24(40)	-27.27(55)	-575.3(17)
^{65}Cu	$3/2^-$	+6281.9(14)	-23.5(20)	
^{67}Cu	$3/2^-$	+6634.2(16)	-23.13(91)	+561.4(35)
^{69}Cu	$3/2^-$	+7492.3(23)	-20.0(28)	+1078.8(26)
^{70}Cu	6^-	+901.54(23)	-37.4(28)	+1347.1(32)
^{71}Cu	$3/2^-$	+5999.7(39)	-23.4(41)	+1526.7(38)
^{72}Cu	2^-	-2663.7(42)	+25.5(79)	+1786.5(40)

Table 5.4: Results from the 2007 experiment.

The consistency between the different experiments is extremely good. In order to produce the final numbers, the weighted average has been taken, as explained in section 5.1.3. A few special cases/exceptions have to be mentioned. The result from 2007 on ^{65}Cu was not taken in the average, as the spectrum was only recorded once during this experiment and the laser was not stable at that time. Also for the $^2S_{1/2}$-$^2P_{1/2}$ transition in 2008, ^{65}Cu was disregarded as the voltage was unstable at the time of the single measurement that was performed. The ^{65}Cu results of 2006 and 2008 in the $^2S_{1/2}$-$^2P_{3/2}$ transition however represent more than ten independent scans each and are therefore much more reliable. Finally, the B-factor of ^{72}Cu in 2007 was not taken into account, as this measurement consisted of a lot of scans on each peak separately.

Isotope	I^π	$A(^2S_{1/2})$(MHz)	$B(^2P_{3/2})$(MHz)	Isotope shift (MHz)
^{61}Cu	$3/2^-$	+5562.5(18)	-28.4(31)	-1187.6(76)
^{65}Cu	$3/2^-$	+6284.27(81)	-26.55(75)	
^{68}Cu	1^+	+9474.9(18)	-11.4(12)	+850.5(58)
^{68}Cu	6^-	+761.62(28)	-58.4(20)	+812.3(71)
^{70}Cu	1^+	+7035.3(49)	-16.4(35)	+1307.1(83)
^{70}Cu	3^-	-4437.1(12)	-17.7(57)	+1334.6(84)
^{70}Cu	6^-	+901.19(42)	-37.9(19)	+1351.3(83)
^{71}Cu	$3/2^-$	+6001.4(14)	-25.3(20)	+1525.9(91)
^{72}Cu	2^-	-2663.76(97)	+9.9(23)	+1792(12)
^{73}Cu	$3/2^-$	+4597.8(12)	-26.5(11)	+1984(12)
^{74}Cu	2^-	-2109.3(22)	+36.0(52)	+2260(14)
^{75}Cu	$5/2^-$	+1591.5(17)	-35.7(20)	+2484(16)

Table 5.5: Results from the 2008 experiment for the $(^2S_{1/2})$-$(^2P_{3/2})$ transition.

Isotope	I^π	$A(^2S_{1/2})$(MHz)	$A(^2P_{1/2})$(MHz)	Isotope shift (MHz)
^{62}Cu	1^+	-1503.3(27)	-130.7(26)	-855.3(62)
^{63}Cu	$3/2^-$	5865.81(98)	505.20(79)	-581.0(57)
^{65}Cu	$3/2^-$	6280.4(13)	542.9(12)	
^{72}Cu	2^-	-2665.4(14)	-231.33(88)	1784(12)

Table 5.6: Results from the 2008 experiment for the $(^2S_{1/2})$-$(^2P_{1/2})$ transition.

The B factor is critically dependent on the exact peak positions within a hyperfine multiplet, whereas the $A(^2S_{1/2})$ factor and isotope shift are not so sensitive to this effect.

Isotope	I^π	$A(^2S_{1/2})$(MHz)	$B(^2P_{3/2})$(MHz)	Isotope shift (MHz)
^{61}Cu	$3/2^-$	+5562.5(18)	-28(3)	-1188(7)
^{62}Cu	1^+	-1508(5)	-1(3)	-825(4)
^{63}Cu	$3/2^-$	+5867.2(3)	-28.0(6)	-576.1(11)
^{64}Cu	1^+	-856.6(15)	+9.6(12)	-249(2)
^{65}Cu	$3/2^-$	+6284.29(19)	-25.9(4)	
^{66}Cu	1^+	+1118(3)	+7.4(17)	+305(3)
^{67}Cu	$3/2^-$	+6632.9(13)	-23.1(9)	+561(4)
^{68}Cu	1^+	+9475.8(16)	-10.9(17)	+859(4)
^{68}Cu	6^-	+761.6(3)	-58.5(17)	+813(3)
^{69}Cu	$3/2^-$	+7490(2)	-20(2)	+1079(2)
^{70}Cu	1^+	+7035(5)	-16(4)	+1307(8)
^{70}Cu	3^-	-4437.1(12)	-18(6)	+1335(8)
^{70}Cu	6^-	+901.4(3)	-37.8(14)	+1347(2)
^{71}Cu	$3/2^-$	+6001.4(14)	-25(2)	+1526(9)
^{72}Cu	2^-	-2664.3(8)	+10(2)	+1787(4)
^{73}Cu	$3/2^-$	+4597.8(12)	-26.5(11)	+1984(12)
^{74}Cu	2^-	-2109(2)	+36(5)	+2260(14)
^{75}Cu	$5/2^-$	+1591.5(17)	-36(2)	+2484(16)

Table 5.7: Final results for the Cu campaign 2006-2007-2008.

Chapter 6

Discussion

6.1 Short introduction to shell model theories

6.1.1 The nuclear shell model

The atomic nucleus cannot be described as a single static object, in fact it is a complex many-body system of constantly interacting particles, the nucleons. Due to the complexity of the nuclear many-body problem, describing the structure of atomic nuclei is not an easy task, and still attracts a lot of research interest nowadays. One of the most successful models used to describe nuclear structure is the shell model.

The strong nucleon-nucleon interaction which binds nucleons into a nucleus is known to be very short-ranged, charge independent and principally attractive in nature. This two-body interaction between nucleons is the basis of the nuclear Hamiltonian:

$$H = T + V = \sum_{i=1}^{A} \frac{\mathbf{p}_i^2}{2m_i} + \sum_{i>k=1}^{A} V_{ik}(\mathbf{r}_i - \mathbf{r}_k) \tag{6.1}$$

with A the mass number of the nucleus, T the kinetic energy term and V the interaction between the nucleons. As the sum in the interaction term V runs over more than $3A$ position coordinates, the hamiltonian of (6.1) is extremely difficult to deal with for all but the lightest elements. In order to simplify the problem, a one-body potential $U_i(\mathbf{r})$ can be added and subtracted:

$$H = \sum_{i=1}^{A} \left[\frac{\mathbf{p}_i^2}{2m_i} + U_i(\mathbf{r}) \right] + \sum_{i>k=1}^{A} V_{ik}(\mathbf{r}_i - \mathbf{r}_k) - \sum_{i=1}^{A} U_i(\mathbf{r}) \equiv H_0 + H_{res} \quad (6.2)$$

where the hamiltonian H_0 now describes the motion of the nucleons in an average field independent of each other, and the second term H_{res} accounts for the residual nucleon-nucleon interaction. The second term is treated as a perturbation on H_0 and is preferentially as small as possible. Hartree-Fock techniques can be used to make a self-consistent calculation of the potential $U_i(\mathbf{r})$ in order to minimize H_{res}. However, often the simple harmonic oscillator potential is chosen as well, which has the advantage that the wave functions can be calculated analytically. First we will investigate nuclear structure starting from a harmonic oscillator potential, without taking correlations between the nucleons into account (so neglecting H_{res}). This approach is called the single or independent particle model. In a subsequent section we investigate the influence of the residual interaction.

The independent particle model

The harmonic oscillator potential is given by:

$$U_i(\mathbf{r}) = \frac{m\omega^2}{2}\mathbf{r}^2 \quad (6.3)$$

with m the mass of the nucleon and ω the frequency of the oscillator. In the three-dimensional harmonic oscillator theory, the mean square charge radius can be calculated to be [89]:

$$\langle r^2 \rangle_{h.o.} = \frac{3\hbar}{4m\omega} \left[\left(\frac{3A}{2} \right)^{1/3} + \frac{3}{2} \right] A. \quad (6.4)$$

Comparing the mean square charge radius of the harmonic oscillator with that of a uniform spherical density distribution, one gets

$$< r^2 >_{uniform} = 3/5(r_0 A^{1/3})^2, \quad (6.5)$$

and the oscillator parameter $\hbar\omega$ is found to be:

$$\hbar\omega \approx \frac{41}{A^{1/3}}. \quad (6.6)$$

A more accurate expression for the oscillator constant is [89]:

$$\hbar\omega \approx \frac{45}{A^{1/3}} - \frac{25}{A^{2/3}}. \tag{6.7}$$

The choice of the oscillator parameter has been found to yield slight changes in effective charges used by shell model calculations, as described in paper III.

The energy of harmonic oscillator wavefunctions is quantized:

$$E_{nlm} = \hbar\omega(2n + l - \frac{1}{2}) \quad n = 1, 2, 3... \tag{6.8}$$

with n the number of nodes of the radial wavefunction and l the orbital quantum number. The Pauli principle limits the number of nucleons in each orbit, producing magic numbers at 2, 8, 20, 40,... Comparing this with observed empirical magic numbers from e.g. two-neutron separation energies, the harmonic oscillator model reproduces the lowest empirical magic numbers, but fails for heavier nuclei. The energy levels are degenerate according to $\Delta l = -2\Delta n$, a degeneracy which is broken when a l^2 term is added to the potential [90]. If also a spin-orbit term, proportional to $\mathbf{l} \cdot \mathbf{s}$, is added to the potential, states with the intrinsic spin aligned parallel with the orbital angular momenta are relatively pushed down in energy. This potential now produces a set of magic numbers which is consistent with empirical observations. Note that $Z, N = 28$ is the first magic number which arises from the spin-orbit coupling, and the $1g_{9/2}$ level is pushed down in energy from the next oscillator shell.

Note that the single particle approximation already predicts the existence of closed shells and produces the correct magic numbers. This model works rather well for nuclei which have one nucleon outside a closed shell, but fails when more particles are added to the core and correlations between the valence nucleons have to be taken into account.

The shell model beyond the independent particle approximation

In order to make theoretical calculations of nuclear structure for the majority of nuclei where correlations between nucleons are important, the second term H_{res} of (6.2) has to be evaluated. The nucleus is assumed to consist of a closed inert core and a valence space where nucleon-nucleon residual interactions are taken into account.

In the simplified case of two identical valence nucleons outside a closed shell, the wave functions are eigenfunctions of [91]

$$H = H_0 + \sum_{i=1}^{2} h_0(i) \tag{6.9}$$

with the energy eigenvalues $E_0 + \epsilon_{j1} + \epsilon_{j2}$. The energy shift due to the residual interaction is given by the so-called two-body matrix elements (TBME):

$$\Delta E(j_1, j_2; J) = \langle j_1 j_2; JM | H_{res}(|\mathbf{r}_1 - \mathbf{r}_2|) | j_1 j_2; JM \rangle \tag{6.10}$$

where j_1, j_2 are the angular momenta of the two orbits coupled to a total angular momentum J. These two-body matrix elements can be evaluated by expanding a central residual interaction in a series of Legendre polynomials [91]. However, before the TBME can be evaluated, an appropriate choice of the nucleon-nucleon interaction has to be made. This will be discussed in the next section.

The evolution of shell structure can be investigated by making a multipole expansion of the residual nucleon-nucleon interaction. The monopole component is given by [6]:

$$V^T_{j_1,j_2} = \frac{\sum_J (2J+1) < j_1 j_2 | V | j_1 j_2 >_{JT}}{\sum_J (2J+1)} \tag{6.11}$$

with $< j_1 j_2 | V | j_1 j_2 >_{JT}$ the diagonal matrix elements coupled to angular momentum J and isospin T. As the angular momentum dependence is averaged out, the mean effect of the other nucleons on a nucleon in a single-particle orbit is investigated. The single-particle energies (SPE) as predicted by the single-particle model, combined with the shift caused by the monopole component of the residual interaction, are referred to as effective single-particle energies (ESPE). The evolution of the ESPE as a function of neutron number can lead to the appearance of new magic numbers, and has attracted a lot of research interest in past years.

Up to now, we have only considered two particles in the same orbit outside a closed shell. In case the particles can move in multiple orbits of a larger valence space, the following hamiltonian has to be diagonalized:

$$\begin{pmatrix} H_{11} & H_{12} & \cdots H_{1n} \\ H_{21} & H_{22} & \cdots H_{2n} \\ \vdots & \ddots & \\ H_{n1} & \cdots & H_{nn} \end{pmatrix}$$

with the H_{lk} given by [91]:

$$H_{lk} \equiv E_k^{(0)\delta_{lk}} + \left\langle \psi_l^{(0)} | H_{res} | \psi_k^{(0)} \right\rangle \tag{6.12}$$

where $E_k^{(0)}$ is the energy of the unperturbed state. For a system of n particles moving in the valence space, projection coefficients called 'coefficients of fractional parentage' (CFP) can be used to write the n-dimensional wavefunctions as a function of the two-particle wavefunctions [91]. These coefficients substantially simplify the shell model calculations. The obtained wavefunctions can be used to calculate various properties of the nucleus such as moments, B(E2) values and so on.

6.1.2 Large-scale shell model calculations

Large-scale shell model calculations are performed by computer codes (like ANTOINE, MSHELL, ...) provided with a given interaction. These interactions are distinguished by their *model space*, which is the valence space where the residual interaction between the nucleons are taken into account. The nucleons in the core (so outside the model space) are assumed to be inert and not contributing to the calculated moments. This simplification gives rise to the concept of *effective* charges. The nuclear charge is overestimated in order to account for the missing excitations due to the limited model space. The more excitations are included in the model space, the closer the effective charges will be to the free nucleon values $e_p = 1e, e_n = 0$. Likewise, the spin g factor is reduced with a factor to overlap theory with experiment.

Another important property of an interaction is the way the two-body matrix elements are determined. This can be done in different ways:
Effective interactions don't attempt to pin down the radial shape of the nucleon-nucleon interaction itself. Instead, the two-body matrix elements and the single-particle energies are taken as free parameters in a

chi square minimization to experimental energy levels and binding energies in that specific region of the nuclear chart.

Realistic interactions start from a potential which is inferred from a fit to the free nucleon-nucleon scattering observables. A G-matrix formalism has been developed to deal with the strong repulsive core of the nucleon-nucleon potential [92]. Often these calculations offer a good starting point for TBME, especially near closed shells. However, experimental single particle energies are influenced by particle-hole excitations across closed shells, which can strongly evolve when nucleons are added/removed from the closed shell. Therefore the single particle energies still have to be determined in an empirical way.

Schematic interactions define a simple radial shape for the nucleon-nucleon interaction leading to a calculation that is numerically less involved and immediately useful for nuclear structure calculations in a given mass region. Often used for the nucleon-nucleon interactions are Gaussian or square well potentials or a δ type interaction.

Interactions used in this work

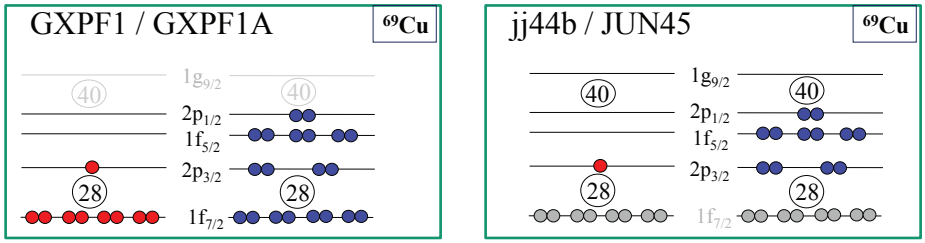

Figure 6.1: The model space of the interactions used in this work. GXPF1 and GXPF1A operate within the pf shell, while JUN45 and jj44b work with a ^{56}Ni core, but include the $g_{9/2}$ orbit.

The experimental results obtained in this work are compared with calculations using four different interactions: The jj44b and JUN45 interactions, and GXPF1 and its modification GXPF1A. In Fig. 6.1, the model space of each of the interactions is given. The GXPF1(A) interactions were designed for the entire pf shell, while jj44b and JUN45 work in the $f5pg9$ model space, including the $g_{9/2}$ orbit, but excluding excitations across $Z, N = 28$.

The GXPF1 interaction can be specified uniquely in terms of four single-particle energies of the $f_{7/2}, p_{3/2}, f_{5/2}$ and $p_{1/2}$ orbits and 195 TBME [59]. Starting values for the TBME were taken from the realistic G-matrix interaction based on the Bonn-C potential [92]. Linear combinations of the initial SPE and TBME were fitted to 699 binding and excitation energies in the region, from ^{47}Ca up to ^{65}Ge, including $^{58-63}$Cu. The fitting procedure is outlined in [93]. The GXPF1 interaction was tested extensively and proved to be very successful in the description of a variety of parameters such as binding energies, magnetic moments, quadrupole moments, 2^+ excitation energies and transition strengths [60]. Some discrepancy in the binding energies for nuclei with $Z \geq 32$ and $N \geq 35$ indicated its limitations towards the end of the pf shell. An increase in the E^{2+} excitation energies for Ca, Ti and Cr isotopes at $N = 32$ was correctly predicted by the GXPF1 interaction. However, for Ca and Ti GXPF1 predicts another increase at $N = 34$, which was found to be in discrepancy with experiment for the case of ^{56}Ti [94]. To improve the description of the excitation energies in ^{56}Ti, a modification of GXPF1 was presented [95]. The two-body matrix elements of the new interaction, GXPF1A, were modified with respect to the GXPF1 interaction in the following way:

$$\Delta V(f_{7/2}f_{7/2}f_{7/2}f_{7/2}; J = 0, T = 1) = +0.2MeV, \tag{6.13}$$
$$\Delta V(f_{5/2}f_{5/2}p_{1/2}p_{1/2}; J = 0, T = 1) = +0.5MeV, \tag{6.14}$$
$$\Delta V(p_{1/2}p_{1/2}p_{1/2}p_{1/2}; J = 0, T = 1) = +0.5MeV. \tag{6.15}$$

The first change decreases the gap between the $f_{5/2}$ and the $f_{7/2}$ orbits slightly. The description of the 2^+ excitation energy in ^{56}Ti could be resolved by reducing this gap only, however this would compromise the excellent agreement for other isotopes such as ^{54}Ti. The third modification changes the ESPE of the $p_{1/2}$ orbit for $N > 32$ and reduces the gap between the $p_{1/2}$ and the $f_{5/2}$ orbits at $N = 34$ by 0.5MeV [A][95].

In addition to these changes, the strength of the quadrupole-quadrupole interaction between the $p_{1/2}$ and $f_{5/2}$ was made stronger:

$$\Delta V(f_{5/2}p_{1/2}f_{5/2}p_{1/2}; J = 2, T = 1) = -0.35MeV, \tag{6.16}$$
$$\Delta V(f_{5/2}p_{1/2}f_{5/2}p_{1/2}; J = 3, T = 1) = +0.25MeV. \tag{6.17}$$

[A] For the elements Ca, Ti, and Cr, the ESPE of the $p_{1/2}$ orbit is still lower than that of the $f_{5/2}$ orbit. For the Cu isotope chain this order is reversed.

This was done in analogy with several nuclei outside a ^{56}Ni core, where an enhanced quadrupole-quadrupole interaction compared to the original G-matrix interaction led to a successful description of 2^+ states [60]. The second modification keeps the monopole centroid unchanged.

The JUN45 interaction was determined in a similar way as the GXPF1 interaction, but then in a different model space consisting of the $p_{3/2}$, $f_{5/2}$, $p_{1/2}$ and $g_{9/2}$ orbits . Starting from a realistic interaction based on the Bonn-C potential, 133 TBME and four SPE were fitted to 400 energy data of 69 isotopes in the region with mass numbers from $A = 63$ to $A = 96$ [8]. As the Ni core already appeared to be rather soft [60] excitations from the $f_{7/2}$ level contribute significantly to the wavefunctions of the low-lying states in the Ni and Cu isotope chains. Therefore, these data were excluded from the fit. The jj44b interaction however, includes the Cu nuclei as well as the $N = 50$ isotones [96].

6.2 Nuclear moments of Cu isotopes compared to calculations in a $f5pg9$ model space

In this section, paper III is inserted.

Nuclear spins, magnetic moments and quadrupole moments of Cu isotopes from $N = 28$ to $N = 46$: probes for core polarization effects

P. Vingerhoets[1], K.T. Flanagan[1,2], M. Avgoulea[1], J. Billowes[3], M.L. Bissell[1], K. Blaum[4], B.A. Brown[5], B. Cheal[3], M. De Rydt[1], D.H. Forest[6], Ch. Geppert[7,10], M. Honma[8], M. Kowalska[9], J. Krämer[10], A. Krieger[10], E. Mané[3], R. Neugart[10], G. Neyens[1], W. Nörtershäuser[7,10], T. Otsuka[11], M. Schug[4], H.H. Stroke[12], G. Tungate[6], D.T. Yordanov[1,41, 2, 3, 4, 5, 6, 7, 8, 9, 10, 11, 12]

[11] *Instituut voor Kern- en Stralingsfysica,*

K.U. Leuven, B-3001 Leuven, Belgium
[22] *IPN Orsay, F-91940 Orsay Cedex, France*
[33] *School of Physics and Astronomy,*
The University of Manchester,
Manchester, M13 9PL, United Kingdom
[44] *Max-Planck-Institut für Kernphysik, D-69117 Heidelberg, Germany*
[55] *National Superconducting Cyclotron Laboratory*
and Department of Physics and Astronomy,
Michigan State University, East Lansing, Michigan 48824-1321, USA
[66] *School of Physics and Astronomy,*
The University of Birmingham,
Birmingham, B15 2TT United Kingdom
[77] *GSI Helmholtzzentrum für Schwerionenforschung GmbH,*
D-64291 Darmstadt, Germany
[88] *Center for Mathematical Sciences,*
University of Aizu, Tsuruga, Ikki-machi,
Aizu-Wakamatsu, Fukushima 965-8580, Japan
[99] *Physics Department, CERN,*
CH-1211 Geneva 23, Switzerland
[1010] *Institut für Kernchemie, Johannes*
Gutenberg-Universität Mainz, D-55128 Mainz, Germany
[1111] *RIKEN, Hirosawa, Wako-shi, Saitama 351-0198, Japan*
[1212] *Department of Physics, New York University,*
New York, New York 10003, USA

Measurements of the ground-state nuclear spins, magnetic and quadrupole moments of the copper isotopes from ^{61}Cu up to ^{75}Cu are reported. The experiments were performed at the ISOLDE facility, using the technique of collinear laser spectroscopy. The trend in the magnetic moments between the $N = 28$ and $N = 50$ shell closures is reasonably reproduced by large-scale shell-model calculations starting from a ^{56}Ni core. The quadrupole moments reveal a strong polarization of the underlying Ni core when the neutron shell is opened, which is however strongly reduced at $N = 40$ due to the parity change between the pf and g orbits. No enhanced core polarization is seen beyond $N = 40$. Deviations between measured and calculated moments are attributed to the softness of the ^{56}Ni core and weakening of the $Z = 28$ and $N = 28$ shell gaps.

PACS: 21.10.Ky; 21.10.Pc; 21.10.Hw; 27.50.+e

I. INTRODUCTION

A key question in nuclear structure research is the persistence of so-called magic numbers when moving away from stability. Nuclei near closed shells are important testing grounds for shell-model theories and have therefore attracted considerable experimental and theoretical research interest. A particularly interesting region is around the magic number of $Z = 28$ protons, as it ranges from the doubly-magic ^{56}Ni on the neutron-deficient side of the nuclear chart towards the neutron-rich doubly magic ^{78}Ni, 14 isotopes away from stability. Furthermore, it includes the semi-magic sub-shell closure at $N = 40$, which is related to the parity change between the pf shell and the $g_{9/2}$ orbital [1–4]. The nickel region has been investigated extensively in the last decade both theoretically and experimentally. On the neutron-deficient side, where protons and neutrons occupy the negative-parity pf orbits, it has been shown experimentally [5, 6] and theoretically [7, 8] that the ^{56}Ni core is rather soft. Excitations of protons and neutrons across the $N = Z = 28$ shell closure from the $f_{7/2}$ orbital into the higher pf orbits are needed to reproduce the magnetic moments of the 2^+ states in the even $^{58-64}$Ni isotopes [5]. Of special interest in the region are the ground-state properties of the copper isotopes, which are dominated by a single proton coupling to the underlying nickel core. Magnetic moment measurements of odd-A Cu isotopes have been performed over a very broad range, from $N = 28$ up to N=46 [6, 9–14]. On the neutron-deficient side, excitations of nucleons from the $f_{7/2}$ orbit across the spin-orbit magic numbers $N = Z = 28$ are needed to reproduce the observed moments for the $\pi p_{3/2}$ ground states [6, 12], as shown by the calculations in the full pf-shell

[8]. On the neutron-rich side, the inversion of the ground-state structure from $\pi p_{3/2}$-dominated to $\pi f_{5/2}$-dominated was established by the measured ground-state spins of ^{73,75}Cu [14]. In this region the strong interaction between the $f_{5/2}$ protons and the $g_{9/2}$ neutrons plays a crucial role [15, 16]. This has been taken into account in two effective shell-model interactions which span the $p_{3/2}\, f_{5/2}\, p_{1/2}\, g_{9/2}$ model space (often abbreviated as the $f5pg9$ model space) based on a ^{56}Ni core [17], and which reproduce the odd $^{69-75}$Cu magnetic moments fairly well [14]. However, an increasing deviation was observed towards ^{73}Cu, which is suggested to be due to missing proton excitations across $Z = 28$. Indeed, calculations starting from a ^{48}Ca core can reproduce nearly perfectly the experimental odd-A Cu magnetic moments beyond $N = 40$ [18].
In this paper, we report on the measured magnetic moments and quadrupole moments of isotopes between ^{61}Cu and ^{75}Cu. The moments and spins of nuclear ground and long-lived isomeric states were determined using high-resolution collinear laser spectroscopy. With this method, each of these observables could be deduced in a model-independent way from the measured hyperfine spectra in the $3d^{10}4s\ ^2S_{1/2} \rightarrow 3d^{10}4p\ ^2P_{3/2}$ transition for atomic copper. A review of recent developments on laser spectroscopy can be found in [19]. In order to extend the measurements towards the neutron-deficient and neutron-rich sides of the valley of stability, the sensitivity of the optical detection has been enhanced by more than two orders of magnitude, by using a bunched ion beam produced with the recently installed gas-filled linear Paul trap (ISCOOL) [20, 21]. The data are compared to shell-model calculations using a ^{56}Ni core.

II. EXPERIMENTAL SET-UP AND PROCEDURE

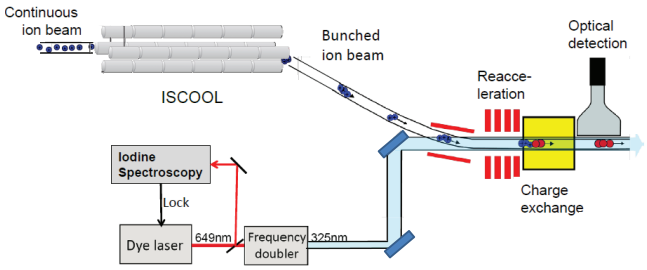

Figure 1: (Color online) Experimental setup of the COLLAPS collinear laser spectroscopy beamline.

The experiment has been performed at the collinear laser spectroscopy setup COLLAPS at ISOLDE, CERN. Radioactive isotopes were produced by 1.4-GeV

Table I: Overview of the isotopes measured during the three COLLAPS beamtimes. The on-line commissioning of the ISCOOL cooler/buncher behind the HRS allowed investigation of more exotic isotopes in 2008.

year	separator	Isotopes addressed
2006	GPS	^{63,64,65,66,67,68g,68m,69,70g}Cu
2007	GPS	^{62,63,65,67,69,70g,71,72}Cu
2008	HRS	^{61,65,68g,68m,70g,70m1,70m2,71,72,73,74,75}Cu

protons impinging on a 45 g/cm^2 thick uranium carbide target. The average proton beam current was 1.8 μA. Radioactive atoms were transported from the heated target through effusion and diffusion processes to a thin capillary tube, where they were step-wise ionized by the Resonance Ionization Laser Ion Source (RILIS). This was achieved in a two-step excitation scheme using the 327.4 nm $3d^{10}4s\ ^2S_{1/2} \rightarrow 3d^{10}4p\ ^2P_{1/2}$ transition, followed by a 287.9 nm transition into an auto-ionizing state [22]. The ions were then accelerated and mass-separated, using either the general purpose isotope separator (GPS) or the high-resolution isotope separator (HRS). The calibration of the acceleration voltage is described in [23]. The copper ions were overlapped with the laser beam in the COLLAPS beam line by electrostatic deflectors (Fig. 1). The ions were neutralized in a sodium charge-exchange cell heated to approximately 220°C. Subsequently, the atom beam could be resonantly excited from the $^2S_{1/2}$ atomic ground state to its $^2P_{3/2}$ state with a transition wavelength of 324.754 nm. The fluorescence was observed with two photomultiplier tubes (PMTs). Instead of scanning the laser frequency, a tunable post-acceleration voltage of ±10kV was applied to the charge-exchange cell to obtain the resonance condition for the neutral copper atoms via Doppler tuning. A summary of the experimental beamtimes is given in Table I. Typical ^{A}Cu beam intensities observed during the three experimental runs are shown in Fig. 2. As for most exotic isotopes the beam current was too small to be recorded with the Faraday cup, the beam intensities were determined from the experimental efficiency as follows. For a stable ^{65}Cu beam, the experimental efficiency was given by:

$$\epsilon_{\mathrm{COLLAPS}} = \frac{N_{\mathrm{COLLAPS}}}{N_{\mathrm{FC}}} \tag{1}$$

with N_{COLLAPS} the amount of resonant photons per second observed in the strongest hyperfine component with the photomultiplier tubes, and N_{FC} the ions per second as observed by a Faraday cup placed after the mass separator. This experimental efficiency, which was typically 1:10000, was then used to calculate the production rate for the other isotopes given in Fig. 2. In the first

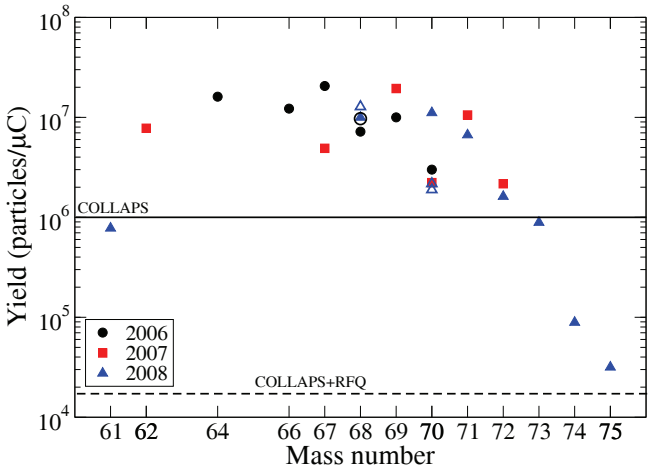

Figure 2: (Color online) Production yield of radioactive ground states (full symbols) and long lived isomers (open symbols) during the experiments using the GPS (circles and squares) and using HRS (triangles). The limit for laser spectroscopy measurements before installation of the ISCOOL device is indicated with a solid line, the current limit is shown by a dashed line.

two runs, the radioactive beam was accelerated to 50 keV and mass separated by the GPS. With a continuous ion beam, the optical detection of the resonant fluorescence was limited to ion beams of several 10^6 pps, due to stray light from the laser beam. After installation of the linear gas-filled Paul trap ISCOOL [20, 21] behind the HRS, measurements could be extended to more exotic isotopes with rates of a few 10^4 pps. With ISCOOL the ions were trapped for typically 100 ms, and then released in a short pulse with a temporal width of $\sim$25 μs. By putting a gate on the PMT photon counting, accepting counts only when a bunch passed in front of the PMT, a reduction of the non-resonant photon background by a factor of 4000 is achieved. This greatly improved the quality of the observed resonances, reduced the scanning time significantly and allowed investigation of more exotic isotopes. An example is given in Fig. 3 for measurements on ^{72}Cu.

The laser system consisted of an Ar ion or Verdi pump laser and a Coherent 699 CW ring dye laser. Two methods have been used to correct for possible drifts in laser frequency during the experiments. In experiments with a continuous beam and the GPS mass separator, a reference isotope was scanned during each scan of a radioactive isotope, by fast switching the mass selection of the GPS magnet. Because the mass change with the HRS magnets is not fast enough, during experiments with the ISCOOL buncher the frequency of the

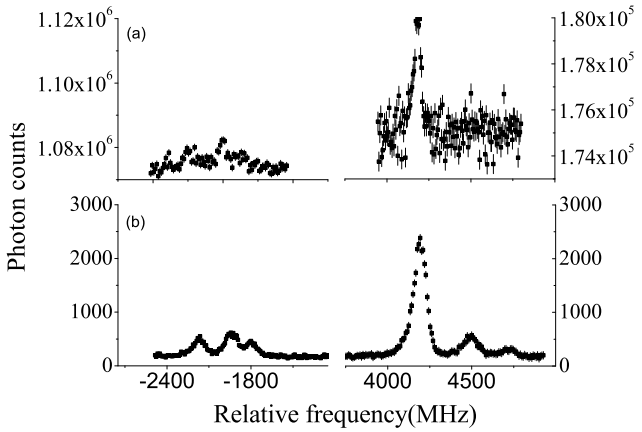

Figure 3: Fluorescence spectra for ^{72}Cu. (a) Before installation of the cooler/buncher, after 10 hours of measurement. (b) With a bunched ion beam and photon gating, all 6 peaks are clearly resolved after 2 hours of measurement.

dye laser was locked to the iodine line at 15406.9373 cm^{-1} using frequency modulation saturation spectroscopy. The exact frequency was measured with a Menlo systems frequency comb, and a frequency drift of less than 500 kHz (or $2{\cdot}10^{-5}$ cm^{-1}) was observed during the experiment. A Spectra-Physics Wavetrain external cavity frequency doubler was used for second harmonic generation. A typical value of the laser power in the beamline was 1-2 mW.

III. RESULTS

Laser spectroscopy allows an accurate determination of magnetic moments and spectroscopic quadrupole moments, as well as isotopic changes in the mean square charge radius. In free atoms, the electronic levels are split with respect to their fine-structure energy by the hyperfine interaction, according to

$$E_F = \frac{1}{2}AC + B\frac{\frac{3}{4}C(C+1) - I(I+1)J(J+1)}{2I(2I-1)J(2J-1)} \tag{2}$$

with the quantum number F given by $\mathbf{F}$=$\mathbf{I}$+$\mathbf{J}$, I being the nuclear and J the electronic angular momentum, and

$$C = F(F+1) - I(I+1) - J(J+1). \tag{3}$$

$A = \frac{\mu B_J}{IJ}$ depends on the nuclear magnetic moment μ, with B_J the magnetic field of the electrons at the position of the nucleus. $B = Q_s V_{zz}$ is related to the spectroscopic quadrupole moment Q_s, with V_{zz} the electric field gradient created by the atomic electrons at the nucleus.
V_{zz} is only non-zero in atomic states with $J > 1/2$. In order to be able to extract the quadrupole moment, the $^2S_{1/2} \rightarrow ^2P_{3/2}$ transition was therefore used in the measurements reported here. This transition is also sensitive to the nuclear spin. The sign of the nuclear moment is determined from the measured hyperfine spectrum, as shown in Fig. 4 for ^{64}Cu and ^{66}Cu. In the case of a nuclear spin 1, five allowed transitions can be induced between the ground state and the excited hyperfine-split levels.

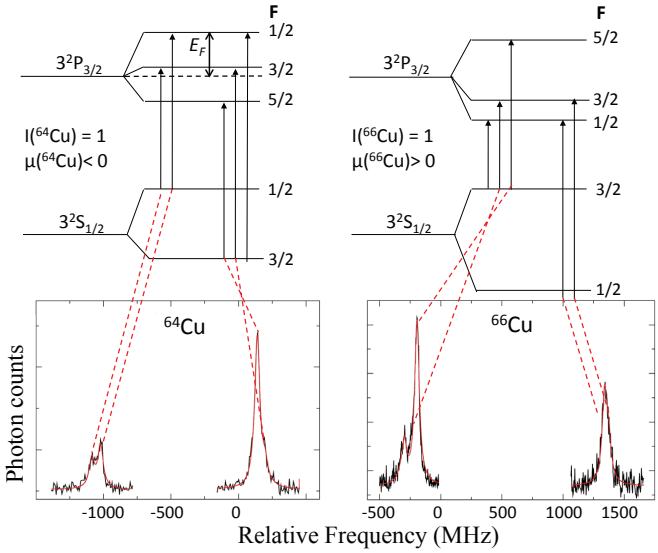

Figure 4: (color online) Top: hyperfine splitting of the $^2S_{1/2}$ and $^2P_{3/2}$ levels for a nuclear spin $I = 1$. The hyperfine energy E_F is given relative to the fine-structure energy. Bottom: hyperfine spectra for ^{64}Cu and ^{66}Cu. The sign of the magnetic and quadrupole moment is unambiguously determined by the positions and relative intensities of the resonances.

Fitting of the spectra was done with Lorentzian functions assuming equal widths and with the peak intensities as free parameters. The relative peak positions were constrained by equation (2). The other fit parameters were the hyperfine parameters A($^2S_{1/2}$), A($^2P_{3/2}$), B($^2P_{3/2}$) and the center of gravity of the hyperfine structure. The fit was performed with an assumed value of the nuclear spin. A ROOT script employing the standard MINUIT fit pack-

Table II: Collinear laser spectroscopy results for copper ground and isomeric states. For the long-lived isomeric states the excitation energies are given [24, 25]. The obtained values for ^{63,65}Cu are in agreement with literature [26, 27]. For ^{62}Cu, ^{64}Cu and ^{66}Cu the ratio of hyperfine parameters was fixed to the literature value 30.13(2)[26, 27]. The results of $^{71-75}$Cu have already been published in [14, 28].

Isotope	I^π	Ex(keV)	$A(^2S_{1/2})$(MHz)	$A(^2P_{3/2})$(MHz)	$B(^2P_{3/2})$(MHz)
^{61}Cu	$3/2^-$	0	+5564(3)	+185.5(10)	-28(3)
^{62}Cu	1^+	0	-1508(5)	FIXED	-1(3)
^{63}Cu	$3/2^-$	0	+5867.1(5)	+194.5(11)	-28.0(6)
^{64}Cu	1^+	0	-856.6(15)	FIXED	+9.6(12)
^{65}Cu	$3/2^-$	0	+6284.0(7)	+208.4(2)	-25.9(4)
^{66}Cu	1^+	0	+1117(3)	FIXED	+7(2)
^{67}Cu	$3/2^-$	0	+6634.1(11)	+220.2(5)	-23.1(9)
^{68g}Cu	1^+	0	+9472.4(19)	+313.0(7)	-11(2)
^{68m}Cu	6^-	722	+761.8(4)	+25.40(16)	-59(2)
^{69}Cu	$3/2^-$	0	+7489(2)	+248.7(15)	-20(2)
^{70g}Cu	6^-	0	+901.5(3)	+30.06(13)	-37.8(14)
^{70m1}Cu	3^-	101	-4438.1(18)	-147.7(7)	-18(6)
^{70m2}Cu	1^+	242	+7037(6)	+234.4(17)	-16(4)
^{71}Cu	$3/2^-$	0	+6002(2)	+199.6(8)	-25.3(14)
^{72}Cu	2^-	0	-2666(2)	-89.8(6)	+10(2)
^{73}Cu	$3/2^-$	0	+4598(2)	+152.4(3)	-26.5(10)
^{74}Cu	2^-	0	-2113(5)	-71.6(11)	+34(4)
^{75}Cu	$5/2^-$	0	+1593(2)	+53.0(9)	-36(2)

age was used to fit the spectra. The fitting uncertainties on the parameters were multiplied by the square root of the reduced chi-squared of the fit. For most isotopes several independent measurements were performed, in which case the weighted average of the individual results was taken, and the error on the weighted average was taken as:

$$\sigma_{\text{total}} = \max(\sigma_{\text{fit}}, \sigma/\sqrt{N}) \tag{4}$$

with σ_{fit} the statistical error on the weighted average due to the fitting un-

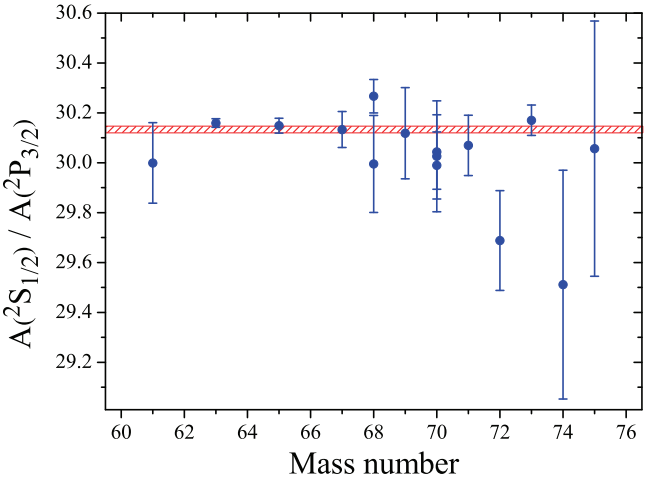

Figure 5: (color online) Ratio of the A-factors obtained from fitting the hyperfine spectra with their assigned nuclear spin. All values are in agreement within 2σ with the literature value of 30.13(2) (horizontal bar).

certainties on the individual spectra, σ the standard deviation of the weighted average and N the number of independent scans. For almost all results, $\sigma_{\rm fit}$ was larger than $\sigma/\sqrt{N}$. A systematic error corresponding to an uncertainty on the acceleration voltage was taken into account, however it was significantly smaller than the statistical error. The results for all isotopes and isomers are listed in Table II. The values for the stable isotopes ^{63,65}Cu are in agreement with the literature values [26, 27].

As the hyperfine anomaly between ^{63}Cu and ^{65}Cu was estimated to be less than $5{\cdot}10^{-5}$ [29], which is an order of magnitude less than our measurement accuracy, the ratio of the hyperfine parameters $A(^2S_{1/2})/A(^2P_{3/2})$ is expected to be constant across the isotope chain, provided the correct nuclear spin has been assumed. This is illustrated in Fig. 5 for the nuclear spins given in Table II. All experimental ratios are in agreement with the literature value of 30.13(2) [26, 27], which is indicated by the horizontal bar. Fitting with a different nuclear spin assumption led to a significant deviation from this average ratio, and allowed to firmly establish the ground-state spins of the exotic isotopes $^{71-75}$Cu [14, 28]. The deduced spins for the other isotopes are in agreement with the literature values [30]. For the odd-odd isotopes ^{62,64,66}Cu, the statistics in the spectra did not allow a fit with a free ratio of A-parameters, and these spectra were fitted with the ratio fixed to 30.13.

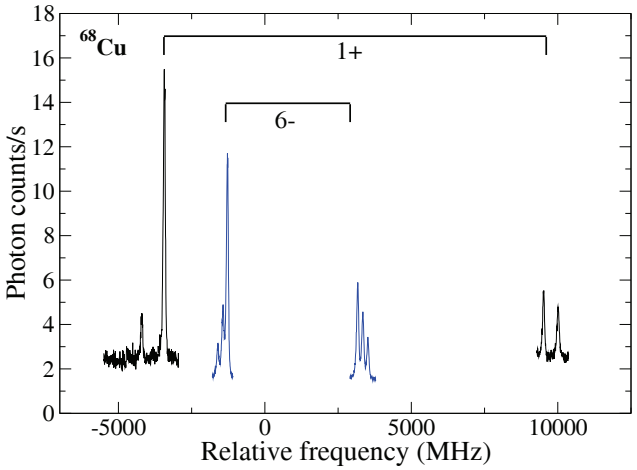

Figure 6: (color online) Hyperfine spectrum for ^{68}Cu. The transition lines for the ground and isomeric state are shown. The zero of the frequency scale corresponds to the center of gravity of the ^{65}Cu hyperfine structure.

From the A and B factors in Table II, we can determine the magnetic dipole and electric quadrupole moments of the isotopes and isomers relative to those of a reference isotope:

$$\mu = \frac{AI}{A_{\rm ref} I_{\rm ref}} \mu_{\rm ref} \tag{5}$$

$$Q = \frac{B}{B_{\rm ref}} Q_{\rm ref}. \tag{6}$$

We used the literature values for the stable ^{65}Cu isotope as a reference, with $A_{\rm ref}$=+6284.405(5) MHz, $B_{\rm ref}$= –25.9(4) MHz, $\mu_{\rm ref}$= +2.3817(3) μ_N and $Q_{\rm ref}$ = −19.5(4) efm^2 [9, 26, 27]. The deduced magnetic dipole and electric quadrupole moments are shown in Table III and compared to earlier results. All values presented here (except for ^{66}Cu) are in agreement with literature, but in most cases the precision has been greatly improved. For ^{66}Cu the sign of the magnetic moment was previously incorrectly assigned, and was found to be positive instead of negative [9]. As shown in Fig. 4 for ^{64,66}Cu, the sign of the magnetic moment determines the ordering of the hyperfine levels, which is observed directly through the intensity and position of the resonances. For ^{68}Cu and ^{70}Cu, low-lying isomers were observed, which were previously identified [24, 31, 32]. Their moments were measured with in-source laser spectroscopy yielding values with very low precision because only the ground-state splitting was resolved [31, 33]. The results of [33] are shown in table III, as the errors in

[31] appear to be underestimated. With the technique of collinear laser spectroscopy all transitions can be resolved (Fig. 6). In that way, the error on the magnetic moments is reduced by three orders of magnitude and the quadrupole moments can be obtained as well.

Table III: Nuclear moments, deduced relative to the stable ^{65}Cu, show an excellent agreement with the literature values.

Isotope	I^π	$\mu_{exp}(\mu_N)$	$\mu_{lit}(\mu_N)$	ref	Q_{exp}(efm^2)	Q_{lit}(efm^2)	ref
^{57}Cu	$3/2^-$		+2.582(7)	[6]			
^{59}Cu	$3/2^-$		+1.910(4)	[6]			
			+1.891(9)	[34]			
^{61}Cu	$3/2^-$	+2.1089(11)	+2.14(4)	[9]	-21(2)		
^{63}Cu	$3/2^-$	+2.2236(4)	+2.22329(18)	[9]	-21.1(7)	-21.1(4)	[9]
^{65}Cu	$3/2^-$		+2.38167(25)	[9]		-19.5(4)	[9]
^{67}Cu	$3/2^-$	+2.5142(6)	+2.54(2)	[11]	-17.4(8)		
^{69}Cu	$3/2^-$	+2.8383(10)	+2.84(1)	[10]	-14.7(16)		
^{71}Cu	$3/2^-$	+2.2747(8)	+2.28(1)	[12]	-19.0(16)		
^{73}Cu	$3/2^-$	+1.7426(8)			-20.0(10)		
^{75}Cu	$5/2^-$	+1.0062(13)			-26.9(16)		
^{58}Cu	1^+		+0.479(13)	[35]			
^{60}Cu	2^+		+1.219(3)	[9]			
^{62}Cu	1^+	-0.3809(12)	-0.380(4)	[9]	0(2)		
^{64}Cu	1^+	-0.2164(4)	-0.217(2)	[9]	+7.2(9)		
^{66}Cu	1^+	+0.2823(8)	-0.282(2)	[9]	+5.6(13)		
^{68g}Cu	1^+	+2.3933(6)	+2.55(8)(19)	[33]	-8.2(13)		
^{68m}Cu	6^-	+1.1548(6)	+1.26(7)(55)	[33]	-44.0(19)		
^{70g}Cu	6^-	+1.3666(5)	+1.58(9)(57)	[33]	-28.5(14)		
^{70m1}Cu	3^-	-3.3641(15)	-3.54(8)(34)	[33]	-13(4)		
^{70m2}Cu	1^+	+1.7779(15)	+1.89(4)(14)	[33]	-12(3)		
^{72}Cu	2^-	-1.3472(10)			+8(2)		
^{74}Cu	2^-	-1.068(3)			+26(3)		

IV. DISCUSSION

The experimental moments over the long chain of copper isotopes from $N = 28$ to $N = 46$ are a good testing ground for theoretical calculations as they span a broad range in neutron number. The most neutron-rich isotopes require the inclusion of the $\nu g_{9/2}$ orbital in the model space for shell-model calculations, increasing drastically the dimensionality of the problem. For the isotopes up to ^{69}Cu, it has been shown that the full pf shell is sufficient to describe their ground-state magnetic moments [6]. That is because a single-particle excitation to the $\nu g_{9/2}$ orbital is forbidden due to the parity change. Several effective shell-model interactions have been developed for the pf shell (see [7] for an overview). The most recent one, GXPF1 and its modifications [7, 8], allows description of the properties of many isotopes in this region from ^{40}Ca up to the heavier isotopes around ^{56}Ni.

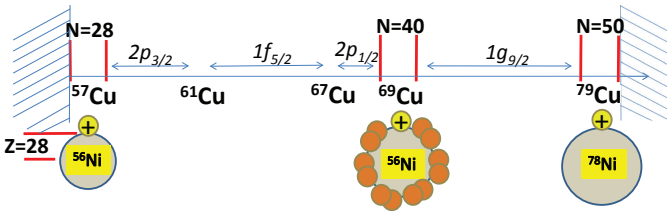

Figure 7: (color online) The model space of the jj44b and JUN45 interactions consists of a ^{56}Ni core, with copper isotopes having one proton outside the magic $Z = 28$ shell. Beyond ^{57}Cu$_{28}$ up to ^{79}Cu$_{50}$, the negative parity neutron orbits $2p_{3/2}$, $1f_{5/2}$, $2p_{1/2}$ and the positive parity $1g_{9/2}$ are filled, from the $N = 28$ to the $N = 50$ shell gap across the $N = 40$ harmonic oscillator sub-shell gap.

Here, we will compare the moments of the full copper chain with calculations in an extended model space including the $g_{9/2}$ orbital. Two effective shell-model interactions have been developed for the $f5pg9$ model space starting from a ^{56}Ni core (Fig. 7), excluding excitations of protons and neutrons across $N = Z = 28$. The jj44b interaction is determined by fitting single particle energies and two-body matrix elements to data from the nickel and copper chain and data along the $N = 50$ isotones [36]. This interaction should thus give rather good results for the copper isotopes presented here. The JUN45 interaction on the other hand, has been fitted to experimental data of 69 nuclei with masses A=63 to A=96 in the upper pf shell, excluding all nickel and copper isotopes [17]. In the latter study its aim was to investigate the effect of the missing $f_{7/2}$ orbital on the calculated nuclear properties in this region. Comparing the calculated magnetic and quadrupole moments, as well as the low-level structure of the

copper isotopes with our experimental data will provide a good test for this study. A recent calculation with an effective interaction in an extended $pfg_{9/2}$ model space, starting from a ^{48}Ca core [18], very well reproduced the experimental magnetic moments of the odd-A Cu isotopes beyond $N = 40$, while the two above models (jj44b, JUN45) based on the ^{56}Ni core overestimated the ^{71,73}Cu magnetic moments [14]. Also, the observed steep lowering of the $1/2^-$ level towards ^{75}Cu was reproduced in [18], while not in [14]. This indeed suggests the need for including proton excitations across $Z = 28$ in order to describe correctly the properties of the neutron-rich Cu isotopes.

In the next section we will discuss the properties of the odd-A Cu isotopes, whose ground-state moments are dominated by the odd proton occupying either the $\pi p_{3/2}$ or $\pi f_{5/2}$ level. The second part of the discussion will focus on the properties of the odd-odd Cu isotopes, which are entirely dependent on the coupling of the single proton to neutrons in the $f5pg9$ space.

1. The odd-A Cu isotopes

The nuclear g-factor is a dimensionless quantity related to the magnetic moment via the nuclear spin:

$$g = \frac{\mu}{I\mu_N} \tag{7}$$

with μ_N the nuclear magneton. The g-factor is very sensitive to the orbital occupation of the unpaired nucleons [37].

In Fig. 8 the odd-A Cu g-factors are compared with the results from both interactions. The experimental g-factors for ^{57}Cu ($N = 28$) and ^{69}Cu ($N = 40$) are closest to the effective single particle value for a $\pi p_{3/2}$ configuration. This suggests magicity at $N = 28$ and $N = 40$. Indeed, in magic nuclei the ground state wave function can be approximated by a pure single particle configuration and so its g-factor will correspond to that of the pure configuration. The fact that $N = 40$ appears here as a magic number, with the properties of a shell closure, is not only related to the magnitude of the energy gap between the $\nu p_{1/2}$ and the $\nu g_{9/2}$ single particle levels. The magic behavior is mostly due to the parity change, which does not allow M1 excitations from the negative parity pf orbits into the positive parity $\nu g_{9/2}$ orbital.

The fact that a rather large reduction of the effective single particle value is needed to reproduce the experimental g-factors is because small contributions of M1-excitations of the type $(f_{7/2}^{-1} f_{5/2})_{1^+}$ have a strong impact on the experimental g-factor. The fact that calculations without such excitations do not reproduce the experimental values towards $N = 28$ (as in Fig. 8) is an indication that the $N = 28$ gap is not very large. This was already known from earlier studies [5, 8]. Indeed, the experimental g-factors of the neutron-deficient

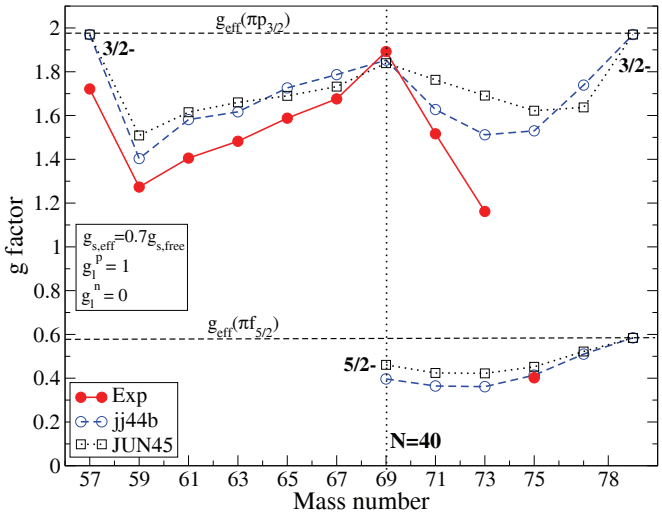

Figure 8: (color online) Experimental g-factors (filled dots) compared with calculations (open symbols) using the jj44b and JUN45 interactions [17]. An effective spin g-factor of $0.7g_{\mathrm{s,free}}$ was adopted.

Cu isotopes are very well reproduced with the GXPF1 shell model interaction in the full pf space [6, 8], which include proton and neutron excitations across $N = 28$. Note that in this pf model space, only a minor reduction of the g_s factor is needed ($0.9g_{\mathrm{s,free}}$) to reproduce the experimental moments.

On the neutron-rich side of $N = 40$, there is an unusually large discrepancy between theory and experiment for ^{73}Cu, but not for ^{75}Cu. This is probably because excitations of protons from the $\pi 1f_{7/2}$ level become increasingly important from $N = 40$ onwards, as the gap between the $\pi 1f_{5/2}$ and the $\pi 1f_{7/2}$ levels decreases under the influence of the tensor force when the $1g_{9/2}$ neutron orbit gets filled [15, 18]. The g-factor of ^{75}Cu is then well reproduced without including such proton excitations, because the $I = 5/2$ ground state of ^{75}Cu is dominated by a single proton in the $1f_{5/2}$ orbit, thus blocking the $(\pi f_{7/2}^{-1} f_{5/2})_{1^+}$ mixing into the wave function.

The experimental energy levels for the odd-A Cu isotopes are compared with jj44b and JUN45 interactions in Fig. 9. The $3/2^-$ state is the ground state for most isotopes, dominated by a proton in the $\pi 2p_{3/2}$ level. The spin inversion of the ground state from $3/2^-$ to $5/2^-$ at ^{75}Cu, dominated by a proton in the $\pi 1f_{5/2}$ level [14], is correctly reproduced by both interactions. The lowering of the $1/2^-$ level however is not so well reproduced, which might be attributed to missing proton excitations from the $\pi f_{7/2}$ level, as illustrated in [18]. Towards

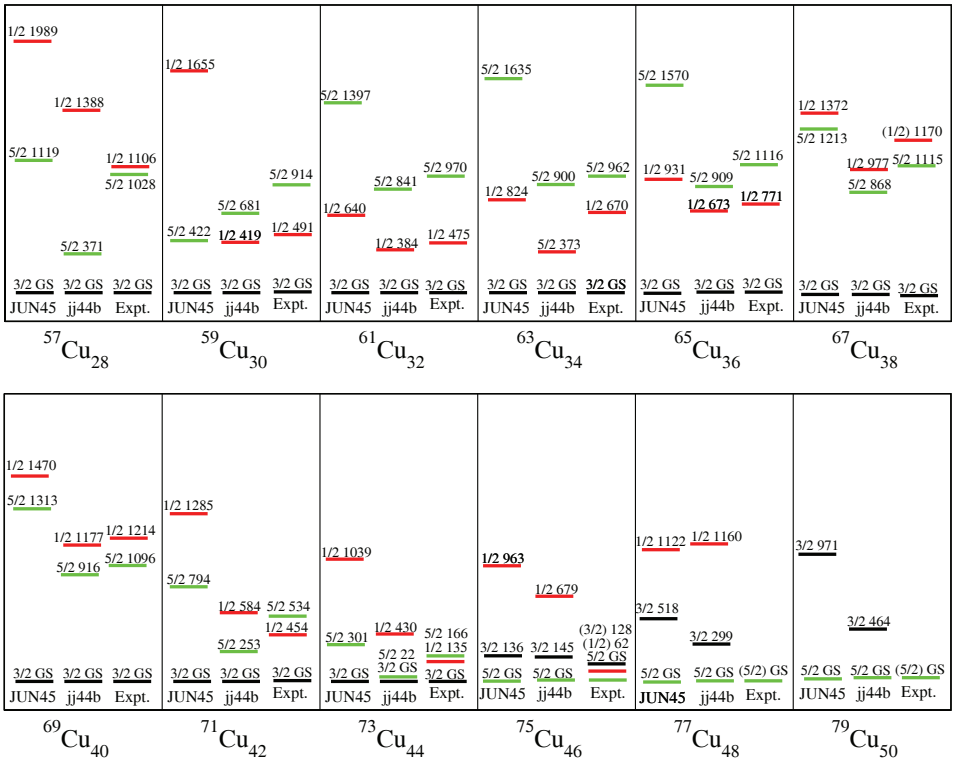

Figure 9: (color online) Experimental and calculated energy levels of odd-A Cu isotopes [30, 38–41]. Only the lowest $1/2^-$, $3/2^-$ and $5/2^-$ states are shown.

^{79}Cu, the calculated energy spacing between the $5/2^-$ gs and the $3/2^-$ first excited state increases. At $N = 50$, where the neutron space is completely filled, this gap is very sensitive to the effective single particle energy between the $\pi 1f_{5/2}$ and $\pi 2p_{3/2}$ orbits. Unfortunately no data are available for ^{79}Cu, but in the ^{81}Ga isotone this $(5/2^- - 3/2^-)$ energy spacing is measured to be 351 keV. Both interactions reproduce this fairly well: 239 and 450 keV for jj44b and JUN45, respectively [42]. Thus we can expect the experimental energy of the $3/2^-$ level in ^{79}Cu between 464 keV and 971 keV. On the other hand, the recent shell-model calculation that takes into account proton excitations across $Z = 28$ [18] predicts this $3/2^-$ level above 1.5 MeV [41]. Clearly, experimental data on the neutron-rich copper level schemes are required to further investigate this.

On the neutron deficient side, the jj44b interaction strongly underestimates the energy of the lowest $5/2^-$ state in ^{57}Cu, but all other $5/2^-$ levels are calculated

within 200-300 keV from the experimental ones. The $1/2^-$ level is fairly well reproduced up to ^{71}Cu, but agreement diminishes for ^{73,75}Cu. The JUN45 interaction on the other hand, overestimates the energy of the $1/2^-$ level in ^{57}Cu by almost 1 MeV, while the agreement is better for the copper isotopes up to ^{69}Cu. However, from ^{71}Cu onwards, the $1/2^-$ level is calculated again about 800 keV too high.

One of the questions raised in this region of the nuclear chart, is related to the onset of collectivity beyond $N = 40$. The spectroscopic quadrupole moment is an ideal parameter to probe collectivity and reveal if the shape of nuclei strongly evolves when the number of available neutron correlations increases towards mid-shell, between $N = 28$ and $N = 50$. As the jj44b and JUN45 interactions assume inert ^{56}Ni and ^{78}Ni cores, proton and neutron effective charges have to be used that take into account these limitations in the model space. Experimental quadrupole moments were used to fit the effective proton and neutron charges (e_π and e_ν), considering that the spectroscopic quadrupole moment is given by:

$$Q_s = e_\pi Q_p + e_\nu Q_n \tag{8}$$

where Q_p and Q_n are the contributions to the calculated spectroscopic quadrupole moments from protons and neutrons, respectively. For the JUN45 interaction, all known quadrupole moments in the model space have been taken into account and the best result was obtained for e_π=+1.5e, e_ν= +1.1e [17]. The same effective charges have been adopted here to calculate quadrupole moments with the jj44b interaction, as the two interactions are active in the same model space.

For both calculations a harmonic oscillator potential was used with a mass dependent energy defined as:

$$\hbar\omega = 41A^{-1/3}. \tag{9}$$

This dependence was also used in [17] to fit the effective proton and neutron charges. If the alternative formula for the oscillator energy is used:

$$\hbar\omega = 45A^{-1/3} - 25A^{-2/3} \tag{10}$$

the calculated quadrupole moments are about 5% larger, and thus the fitted effective charges would be slightly lower. Note that in [42], the calculations with JUN45 and jj44b have both been performed using (10) for the oscillator parameter.

In Fig. 10 the calculated proton and neutron contributions (Q_p and Q_n) to the spectroscopic quadrupole moments are shown for the two interactions (values given in Table IV). From Fig. 10 it is seen that the proton quadrupole moments of configurations dominated by a $\pi p_{3/2}$ proton are rather constant across the

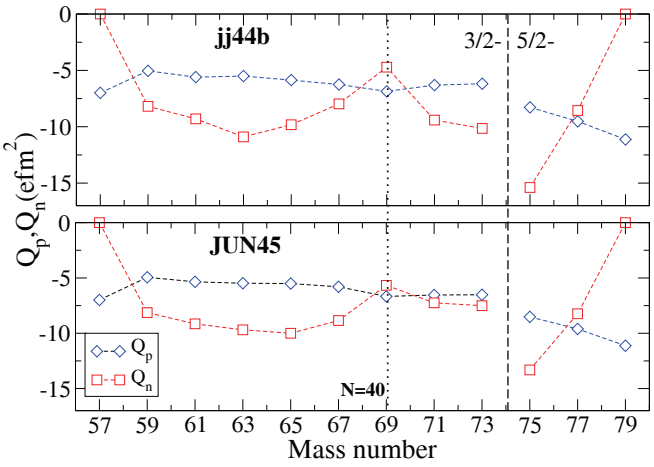

Figure 10: (color online) The contributions to the spectroscopic quadrupole moment due to protons and neutrons separately, as given in Table IV. The neutron contribution is responsible for the observed core polarizing effect when moving away from $N = 40$.

chain, which illustrates that in this case the proton-neutron correlation does not strongly affect Q_p. In the neutron-rich isotopes, dominated by a $\pi f_{5/2}$ ground-state configuration, the proton quadrupole moment is more sensitive to this proton-neutron interaction. The trend is the same for both interactions, though the absolute proton quadrupole moments are slightly larger with jj44b. For the neutron quadrupole moments, a significant difference between the two calculations is seen in the region of the $N = 40$ sub-shell gap. While both calculations show a strong core polarization when adding neutrons to $N = 28$ or removing them from $N = 50$, the reduction at $N = 40$ is more pronounced for the jj44b interaction. The strong increase in core polarization beyond $N = 40$, observed for the jj44b interaction, is missing for the JUN45 interaction. This is an indication that the $N = 40$ gap is too small in the JUN45 effective interaction.

In Fig. 11 the experimental values are compared to calculated spectroscopic quadrupole moments. A reasonable agreement is observed for both calculations. The trend is however better reproduced by the jj44b interaction, which is clearly related to the stronger core-polarizing effect in the neutron quadrupole moments. When neutrons are added or removed from $N = 40$, the experimental moments reveal a strong core-polarization effect. This core polarization is similar on both sides of $N = 40$: the ^{65,67}Cu and ^{71,73}Cu spectroscopic quadrupole moments are the same within error bars. No increased collectivity is observed

Table IV: Experimental and calculated quadrupole moments. The proton and neutron contributions to the theoretical quadrupole moment (Q_p and Q_n) are given separately. Q_{theo} is obtained with effective charges $e_\pi = +1.5e$, $e_\nu = +1.1e$.

		Exp	**jj44b**			**JUN45**		
Isotope	I^π	Q_{exp}(efm^2)	Q_p(efm^2)	Q_n(efm^2)	Q_{theo}(efm^2)	Q_p(efm^2)	Q_n(efm^2)	Q_{theo}(efm^2)
^{57}Cu	$3/2^-$		-6.99	0	-10.49	-6.99	0	-10.49
^{59}Cu	$3/2^-$		-5.04	-8.19	-16.56	-4.94	-8.13	-16.35
^{61}Cu	$3/2^-$	-21(2)	-5.60	-9.30	-18.63	-5.35	-9.15	-18.09
^{63}Cu	$3/2^-$	-21.1(4)	-5.50	-10.90	-20.24	-5.48	-9.69	-18.88
^{65}Cu	$3/2^-$	-19.5(4)	-5.86	-9.82	-19.59	-5.51	-10.00	-19.27
^{67}Cu	$3/2^-$	-17.4(8)	-6.25	-7.97	-18.15	-5.80	-8.85	-18.44
^{69}Cu	$3/2^-$	-14.7(16)	-6.86	-4.71	-15.47	-6.67	-5.67	-16.24
^{71}Cu	$3/2^-$	-19.0(16)	-6.31	-9.41	-19.81	-6.54	-7.25	-17.79
^{73}Cu	$3/2^-$	-20.0(10)	-6.18	-10.15	-20.44	-6.52	-7.51	-18.04
^{75}Cu	$5/2^-$	-26.9(16)	-8.28	-15.39	-29.35	-8.52	-13.32	-27.43
^{77}Cu	$5/2^-$		-9.52	-9.00	-23.70	-8.56	-8.24	-23.48
^{79}Cu	$5/2^-$		-11.13	0	-16.70	-11.13	0	-16.70

on the neutron-rich side, as suggested by recent measurements of the B(E2) transition rates in the underlying nickel isotopes [43, 44]. In order to compare the core polarization in ^{75}Cu to that of the other copper isotopes, we calculate the core quadrupole moment. This is done by taking the difference between the spectroscopic (experimental or calculated) value (Q_s) and the single particle moment ($Q_{\rm s.p.}$) for the odd proton:

$$Q_{\rm core} = Q_{\rm s} - Q_{\rm s.p.}. \tag{11}$$

The single particle quadrupole moment ($Q_{\rm s.p.}$) for the $3/2^-$ states is taken as the calculated effective moment for ^{57}Cu, while the $5/2^-$ single particle moment is the calculated effective value for ^{79}Cu. Indeed, these isotopes have no valence neutrons and thus $Q_{\rm s.p.} = e_\pi Q_p$ (see Table IV for values from jj44b and JUN45). The deduced experimental and calculated core polarizations are shown in Fig. 12. The experimental core polarization in ^{75}Cu is the same as in ^{63}Cu, so again no enhancement of collectivity is observed towards the neutron rich isotopes. The jj44b interaction reproduces very well the trend in the core polarization. It seems to slightly overestimate the core polarization in ^{75}Cu, but data on the more neutron-rich isotopes are needed to confirm this. Towards the neutron-deficient side, the core polarization seems underestimated

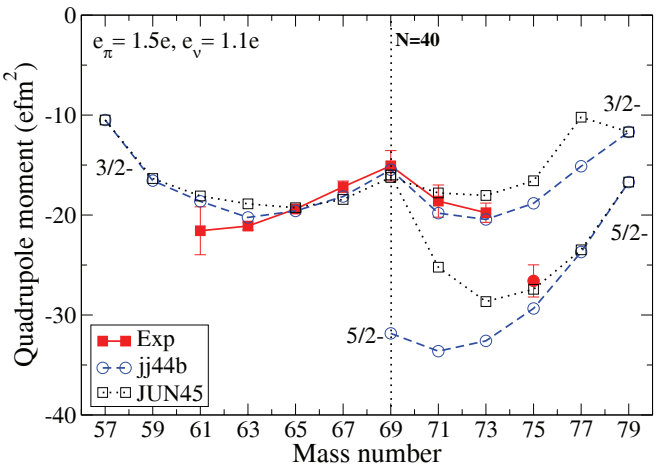

Figure 11: (color online) The measured spectroscopic quadrupole moments compared with shell-model calculations.

in ^{61}Cu. However, a more precise experimental value and more precise determination of the effective proton charge is needed to establish this firmly. For the JUN45 interaction, the core polarization is largely underestimated in all isotopes away from ^{67,69}Cu, both when adding and when removing neutrons from $N = 40$. Adjusting the effective charges does not improve the agreement with experiment.

2. *The even-A Cu isotopes*

The structure of the even-A copper isotopes is dominated by the coupling between the odd proton in one of the $\pi 2p_{3/2}1f_{5/2}2p_{1/2}$ orbits and an unpaired neutron in one of the available neutron orbits. This is illustrated well by comparing the experimental g-factors for the 1^+, 2^+ and 2^- states in $^{58-74}$Cu with empirical values calculated with the additivity relation for moments [37], using experimental g-factors of neighboring even-odd nickel and zinc, and odd-even copper isotopes:

$$g(I) = \frac{g_p + g_n}{2} + \frac{(g_p - g_n)}{2}\frac{j_p(j_p+1) - j_n(j_n+1)}{I(I+1)}. \qquad (12)$$

For example, the possible empirical moments for the 1^+ state in ^{66}Cu for a $\pi p_{3/2}$ coupling to a $\nu p_{1/2}$, $\nu f_{5/2}$ or $\nu p_{3/2}$, are calculated using the experimental g_n factors of the $1/2$, $3/2$ and $5/2$ states in Zn [9] and for g_p the average was taken

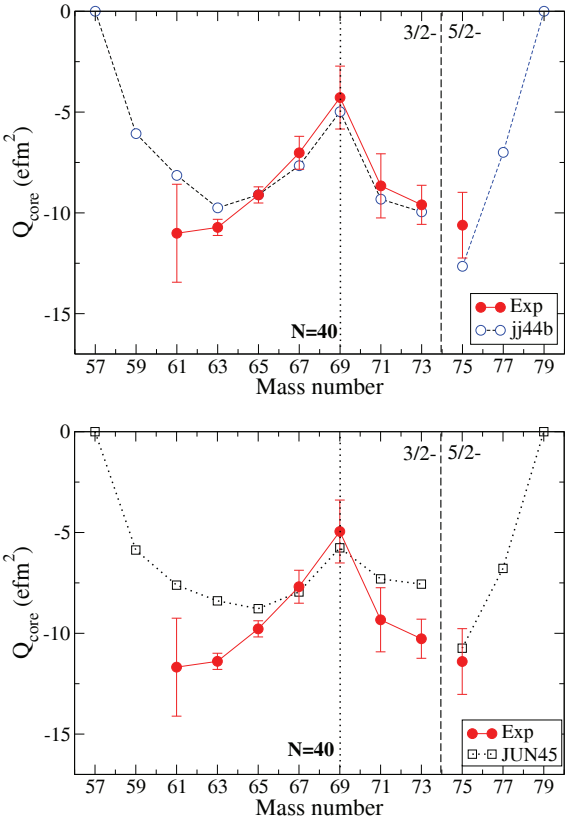

Figure 12: (color online) Experimental core polarization quadrupole moments compared to calculated core polarization moments with jj44b (top) and JUN45 (bottom). See text for details.

between the g-factors of ^{65}Cu and ^{67}Cu. As shown in Fig. 13, the comparison of these empirical g-factors with the experimental values provides an indication for the purity of the state. ^{58}Cu is clearly dominated by a $(\pi p_{3/2} \otimes \nu p_{3/2})$ configuration, while for ^{60}Cu, the empirical g-factors are not separated enough to make a conclusion about the structure. ^{62}Cu and ^{64}Cu have a dominant $(\pi p_{3/2} \otimes \nu f_{5/2})$ structure, as already concluded in [35]. The sign of the ^{66}Cu g-factor was determined to be positive, in contrast to the literature value (see Table III). This illustrates that ^{66}Cu has a strongly mixed ground state, with a significant occupation of the $\nu p_{1/2}$ orbital. The 1^+ states in ^{68}Cu and ^{70}Cu show a $(\pi p_{3/2} \otimes \nu p_{1/2})$ character, as expected. For the neutron-rich isotopes ^{72,74}Cu, the ground-state spin was measured to be $I = 2$ [28], and from the

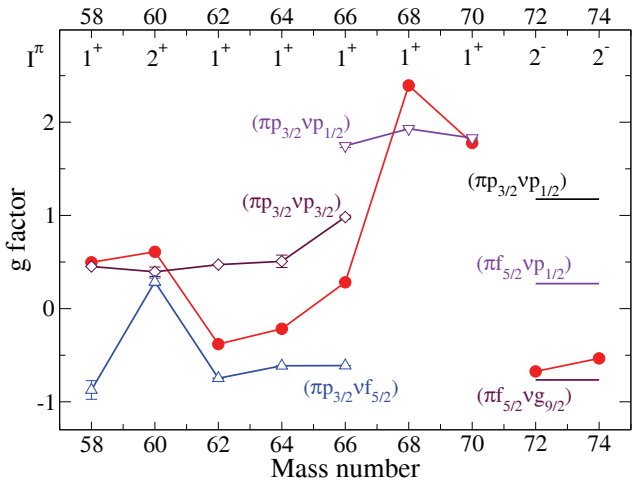

Figure 13: (color online) The experimental g-factors of the ground states of $^{58-74}$Cu (Table III, solid circles) are compared with empirical g-factors using the additivity relation for simple proton-neutron configurations. The positive sign of the ^{66}Cu value reveals a strongly mixed ground-state wave function.

measured negative sign of the magnetic moment it was concluded that the ground state must have a dominant $(\pi f_{5/2} \otimes \nu g_{9/2})$ configuration. Indeed, the empirical magnetic moment of this configuration is in agreement with the observed value (see Fig. 13).

In ^{68,70}Cu the experimental g-factors of the 3^- and 6^- states are consistent with a proton in the $2p_{3/2}$ level coupled to a neutron in the $g_{9/2}$ orbit (compare $\mu_{\rm emp}(3^-) = -2.85$ and $\mu_{\rm emp}(6^-) = +1.44$ to the experimental values in Table III). This configuration gives rise to a $(3,4,5,6)^-$ multiplet, where the 6^- state forms the ground state in ^{70}Cu and is isomeric in $^{64-68}$Cu, due to excitation of a neutron across the $N = 40$ shell gap. The energies of these isomeric states are thus a good probe for the strength of the $N = 40$ shell gap. In Fig. 14 we compare the lowest experimental energy levels with the calculated level schemes for both interactions. Due to the very high level density, especially in the neutron-rich isotopes, only the lowest experimental levels and the relevant calculated ones are shown for clarity.

With the JUN45 interaction, the energy of the 6^- level in ^{68}Cu is calculated about 300 keV below the observed value. In ^{66}Cu this level is calculated even 500 keV below the experimental value (at 661 keV, compared to 1154 keV experimentally (not shown in figure)). This supports the assumption that the $N = 40$ gap is too small in the JUN45 interaction. The energies of the 6^-

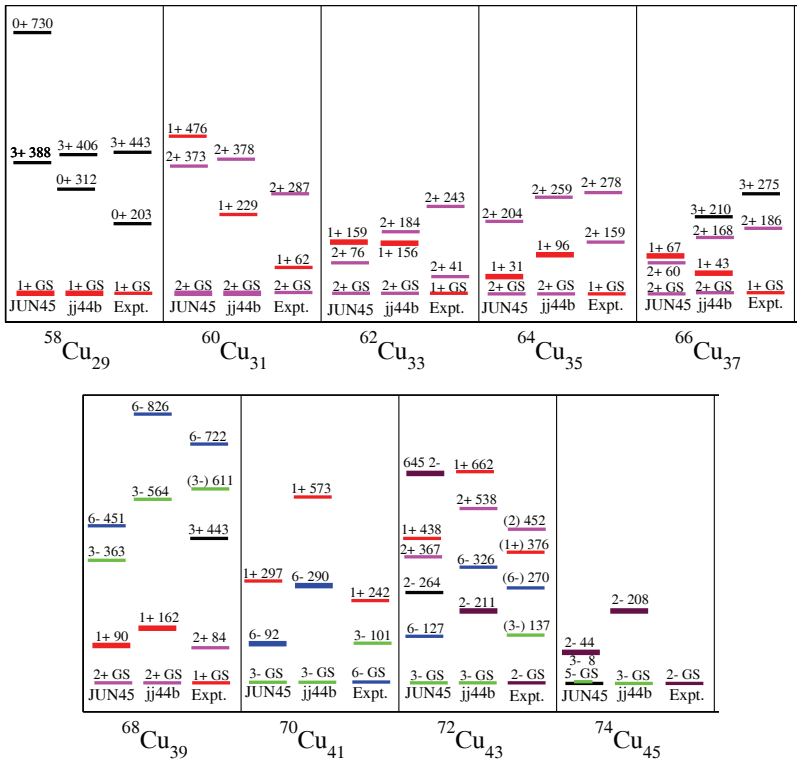

Figure 14: (color online) Experimental and calculated lowest levels in the odd-odd Cu isotopes [24, 25, 30, 45]. Levels in bold have calculated moments in agreement with the experimentally measured magnetic and quadrupole moments of the ground state.

levels calculated with jj44b are respectively 826 and 899 keV, which are 100 keV above and 250 keV below the experimental level energies in ^{68,66}Cu.
Note that for most of the odd-odd isotopes neither theory predicts the correct level to be the ground state. In order to compare the calculated moments to the experimental ones, we have taken the calculated values from the lowest level with the correct spin (indicated by a bold line in Fig. 14). For ^{72}Cu the experimental moments were best reproduced with the JUN45 interaction by the moments for the second 2^- level [28]. This illustrates the strong sensitivity of nuclear moments to the exact composition of the wave function. That level has a dominant $(\pi f_{5/2} \otimes \nu g_{9/2})$ configuration, while the lowest 2^- level has a dominant $(\pi p_{3/2} \otimes \nu g_{9/2}, \sigma = 3)$ configuration, with moments that do not

agree with the observed value [28]. The fact that the 2_2^- level at 645 keV is the real ground state, suggests that in the JUN45 interaction the effective single particle energy of the $\pi f_{5/2}$ level is probably too high in ^{71}Cu.

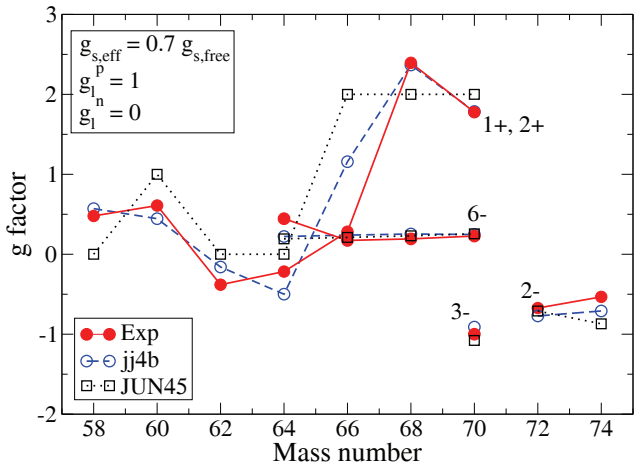

Figure 15: (color online) Experimental g-factors for the odd-odd Cu isotopes (full dots) compared to calculations. The nuclear spin is added to distinguish between the different isomers in $^{64-70}$Cu (experimental values from Table III). Good agreement is obtained, except for the ^{66}Cu 1^+ ground state.

In Fig. 15 the measured g-factors are compared to the results from calculations with the jj44b and JUN45 interactions. The jj44b interaction is very successful in predicting the g-factor trend for the odd-odd Cu isotopes, both for gs and isomeric states. The agreement with the JUN45 results is also reasonable. Only for the ^{66}Cu ground state, the two theories significantly overestimate the observed value. As can be concluded from the empirical g-factors in Fig. 13, this is because a too large $\nu p_{1/2}$ contribution is predicted to occur in the wave function. Such a contribution is certainly present, but not as much as given by the shell-model calculations.

Finally, we compare the quadrupole moments of the odd-odd Cu isotopes with the calculated values from both models, as shown in Fig. 16. The same effective charges have been used as for the odd-A Cu isotopes. The jj44b interaction successfully reproduces all quadrupole moments, except for those of the 2^- levels in ^{72,74}Cu where the deviation is somewhat larger. The JUN45 interaction calculates the quadrupole moments fairly well, but it gives a wrong sign and too large a magnitude for the quadrupole moment of the ^{66}Cu gs. This is in line with the g-factor trend, where it was concluded that the $\nu p_{1/2}$ occupation in ^{66}Cu is overestimated in this calculation. An increased $\nu p_{1/2}$

occupation allows for enhanced neutron pairing correlations in the $\nu p_{3/2} f_{5/2}$ levels and so for extra collectivity, leading to too large a quadrupole moment.

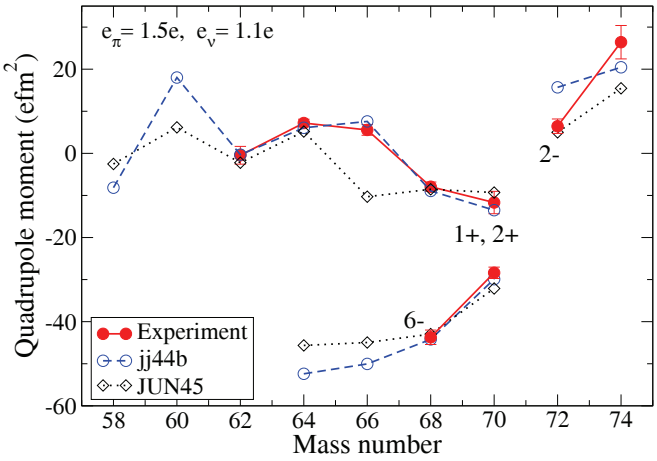

Figure 16: (color online) The experimental quadrupole moments for the odd-odd Cu isotopes compared with calculations [9].

V. SUMMARY

In summary, the technique of collinear laser spectroscopy in combination with the ISCOOL buncher, has been successfully applied to determine the spin, magnetic and quadrupole moments of the ground states and long-lived isomeric states in the $^{61-75}$Cu isotopes with some yields as low as 10^4 pps. The g-factors and quadrupole moments of the odd-A Cu isotopes show an apparent magic behavior at $N = 40$, which is strongly related to the parity change between the pf shell orbits and the $g_{9/2}$ level. Therefore this magic behavior cannot be interpreted only in terms of the energy gap at $N = 40$.

The experimental results have been compared to large-scale shell-model calculations starting from a ^{56}Ni core, using two effective shell-model interactions with protons and neutrons in the $f_{5/2}pg_{9/2}$ model space. On both sides of $N = 40$, the calculations overestimate the measured magnetic moments of the odd-A Cu isotopes. Because spin-flip excitations of the type $(f_{7/2}^{-1} f_{5/2})_{1^+}$ have a very strong influence on the magnetic moment of a state, even if this configuration contributes only one percent to the wave function [13], the overestimated g-factors are an indication that excitations across $Z = 28$ and $N = 28$ should be included in the model space. The collectivity and the onset of core polarization

between $N = 28$ and $N = 50$ has been probed by the quadrupole moments of the odd-A Cu ground states. No sign of an increased collectivity in ^{71,73,75}Cu as compared to ^{63,65,67}Cu has been observed, contrary to what was concluded from B(E2) measurements in the Ni isotopes. Extending quadrupole moment measurements towards ^{57}Cu and ^{79}Cu could provide more information about the softness/stiffness of the ^{56}Ni and ^{78}Ni cores. Comparison of the experimental core quadrupole moments with the calculated ones shows that the jj44b interaction correctly reproduces the observed core polarization when moving away from $N = 40$, while the JUN45 interaction systematically underestimates the onset of collectivity.

The moments of the odd-odd Cu isotopes are very sensitive to the proton-neutron interaction and configuration mixing, and provide a more severe test to the calculations. The jj44b interaction reproduces very well (within a few %) all of the observed magnetic and quadrupole moments of odd-odd Cu isotopes, while for the JUN45 interaction less, but reasonable agreement was found. Only for the ^{66}Cu gs both models fail to reproduce correctly the data. Note, however, that the level with moments agreeing best with experimental values, is the lowest calculated level with the correct spin. This is not always the calculated ground state. In ^{72}Cu it is even the second 2^- level that agrees with the observed gs moments calculated with JUN45. Thus, through the measured moments, a particular configuration can be assigned to the gs wave functions.

This work has been supported by the German Ministry for Education and Research (BMBF) under Contract No. 06MZ9178I, the UK Science and Technology Facilities Council (STFC), the FWO-Vlaanderen (Belgium), EU Sixth Framework through No. Eurons-506065, BriX IAP Research Program No. P6/23 (Belgium), the Max-Planck Society, NSF grant PHY-0758099 and the Helmholtz Association of German Research Centres(VH-NG-037 and VH-NG-148). M. Kowalska was supported by the EU (MEIF-CT-2006-042114). We would like to thank the ISOLDE technical group for their support and assistance during this project.

[1] W.F. Mueller *et al.*, Phys. Rev. Lett **83**, 3613 (1999).
[2] O. Sorlin *et al.*, Phys. Rev. Lett. **88**, 092501 (2002).
[3] K. Langanke *et al.*, Phys. Rev. C **67**, 044314 (2003).
[4] C. Guènaut *et al.*, Phys. Rev. C **75**, 044303 (2007).
[5] O. Kenn *et al.*, Phys. Rev. C **63**, 064306 (2001).
[6] T.E. Cocolios *et al.*, Phys. Rev. Lett. **103**, 102501 (2009).
[7] M. Honma *et al.*, Phys. Rev. C **65**, 061301(R) (2002).

[8] M. Honma *et al.*, Phys. Rev. C **69**, 034355 (2004).
[9] P. Raghavan, At. Data Nucl. Data Tables **42**, 189 (1989).
[10] J. Rikovska *et al.*, Phys. Rev. Lett. **85**, 1392 (2000).
[11] J. Rikovska and N. J. Stone, Hyp. Interact. **129**, 131 (2000).
[12] N.J. Stone *et al.*, Phys. Rev. C **77**, 014315 (2008).
[13] G. Georgiev *et al.*, J. Phys. G **28**, 2993 (2002).
[14] K.T. Flanagan *et al.*, Phys. Rev. Lett. **103**, 142501 (2009).
[15] T. Otsuka *et al.*, Phys. Rev. Lett. **95**, 232502 (2005).
[16] T. Otsuka *et al.*, Phys. Rev. Lett. **104**, 012501 (2010).
[17] M. Honma *et al.*, Phys. Rev. C **80**, 064323 (2009).
[18] K. Sieja and F. Nowacki, Phys. Rev. C **81**, 061303 (2010).
[19] B. Cheal and K.T. Flanagan, J. Phys. G **37**, 113101 (2010).
[20] H. Franberg *et al.*, Nucl. Inst. Meth. B **266**, 4502 (2008).
[21] E. Mané *et al.*, Eur. Phys. J. A. **42**, 503 (2009).
[22] U. Köster *et al.*, Nucl. Instr. Meth. B **160**, 528 (2000).
[23] A. Krieger *et al.*, NIM A (2010), submitted.
[24] J. Van Roosbroeck *et al.*, Phys. Rev. Lett. **92**, 112501 (2004).
[25] I. Stefanescu *et al.*, Phys. Rev. Lett. **98**, 122701 (2007).
[26] Y. Ting and H. Lew, Phys. Rev. **105**, 581 (1957).
[27] J. Ney, Z. Phys. **196**, 53 (1966).
[28] K.T. Flanagan *et al.*, Phys. Rev. C. **82**, 041302 (2010).
[29] P.R. Locher, Phys. Rev. B **10**, 801 (1974).
[30] E. N. S. Data, http://www.nndc.bnl.gov/.
[31] L. Weissman *et al.*, Phys. Rev. C **65**, 024315 (2002).
[32] K. Blaum *et al.*, Europhys. Lett. **67**, 586 (2004).
[33] S. Gheysen *et al.*, Phys. Rev. C **69**, 064310 (2004).
[34] V.V. Golovko *et al.*, Phys. Rev. C **70**, 014312 (2004).
[35] T. E. Cocolios *et al.*, Phys. Rev. C **81**, 014314 (2010).
[36] D. Verney *et al.*, Phys. Rev. C **76**, 054312 (2007).
[37] G. Neyens, Rep. Prog. Phys. **66**, 633 (2003).
[38] S. Franchoo *et al.*, Phys. Rev. C **64**, 054308 (2001).
[39] I. Stefanescu *et al.*, Phys. Rev. Lett. **100**, 112502 (2008).
[40] I. Stefanescu *et al.*, Phys. Rev. C **79**, 044325 (2009).
[41] J. M. Daugas *et al.*, Phys. Rev. C **81**, 034304 (2010).
[42] B. Cheal *et al.*, Phys. Rev. Lett. **104**, 252502 (2010).
[43] O. Perru *et al.*, Phys. Rev. Lett. **96**, 232501 (2006).
[44] N. Aoi *et al.*, Phys. Lett. B **692**, 302 (2010).
[45] J.-C. Thomas *et al.*, Phys. Rev. C **74**, 054309 (2006).

Additional note

For completeness, the table with the quadrupole moment calculations is given as well for the odd-odd Cu isotopes:

Table 6.1: Calculated quadrupole moments using jj44b and JUN45 interactions. The proton and neutron contributions (Q_p and Q_n) are given separately. The theoretical quadrupole moment Q is obtained with effective charges $e_\pi = +1.5e$, $e_\nu = +1.1e$.

		jj44b			**JUN45**		
Isotope	I^π	Q_p(efm^2)	Q_n(efm^2)	Q(efm^2)	Q_p(efm^2)	Q_n(efm^2)	Q(efm^2)
^{58}Cu	1^+	-3.14	-3.14	-8.16	-0.97	-0.97	-2.52
^{60}Cu	2^+	+4.39	+10.39	+18.02	+2.28	+2.51	+6.18
^{62}Cu	1^+	-0.31	+0.14	-0.31	-0.20	-1.75	-2.23
^{64}Cu	1^+	+1.45	+3.55	+6.08	+0.60	+3.89	+5.18
^{66}Cu	1^+	+0.50	+6.21	+7.58	-3.09	-5.15	-10.30
^{66}Cu	6^-	-7.37	-35.44	-50.04	-6.97	-31.36	-44.95
^{68}Cu	1^+	-3.78	-2.97	-8.93	-3.25	-3.33	-8.54
^{68}Cu	6^-	-7.44	-30.03	-44.20	-7.14	-29.31	-42.95
^{70}Cu	6^-	-7.36	-17.14	-29.90	-7.94	-18.36	-21.09
^{70}Cu	3^-	-2.81	-4.96	-9.67	-3.51	-11.67	-18.10
^{70}Cu	1^+	-3.98	-6.84	-13.51	-3.06	-4.29	-9.31
^{72}Cu	2^-	+2.03	+11.50	+15.69	-1.71	-8.64	-6.88
^{74}Cu	2^-	+3.09	+14.37	+20.45	+1.69	+11.75	+15.46

The empirical magnetic moment of the spin 3 state in ^{70}Cu for a proton in the $f_{5/2}$ orbit coupled with a neutron in the $g_{9/2}$ orbit gives a magnetic moment of -1.02μ_N, so in less good agreement with experiment than a proton in the $p_{3/2}$ orbit coupled to a neutron in the $g_{9/2}$ orbit.

6.3 Nuclear moments of neutron-deficient Cu isotopes compared to calculations in a pf model space

In this section g-factors, quadrupole moments and energy level schemes of copper nuclei will be compared to calculations using the GXPF1 and GXPF1A interactions. The properties of these interactions are described in section 6.1.2. The experimental data include results from the latest beamtime in 2010 for the isotopes $^{58-62}$Cu. As the data from this beamtime are still under analysis, the results presented here are preliminary, and a table with the correct values will be given in an upcoming publication. The discussion in this chapter will form the basis of a new article to be published in Physical Review C.

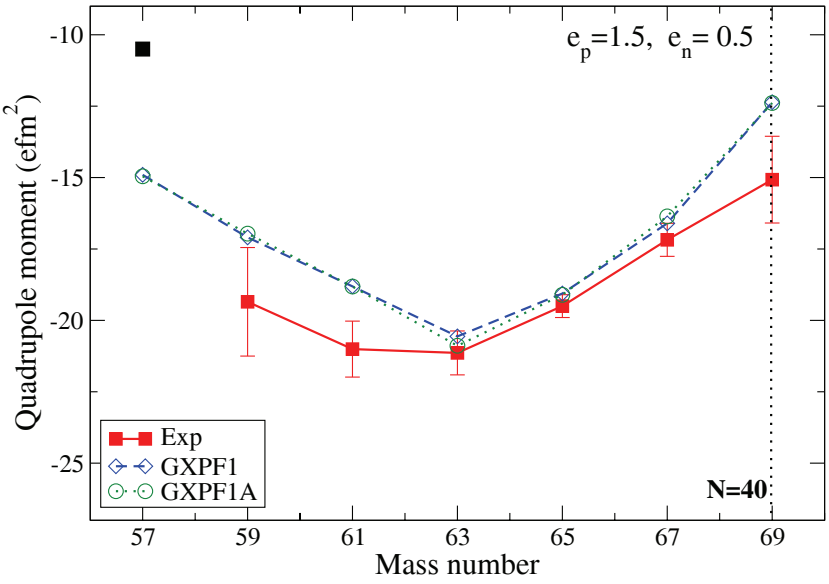

Figure 6.2: The odd-A quadrupole moments are compared with theory. The black point corresponds to the single-particle quadrupole moment of ^{57}Cu, assuming a completely rigid ^{56}Ni core.

In Fig. 6.2 the quadrupole moments are compared with predictions by the GXPF1 and GXPF1A interactions. The black point at ^{57}Cu corresponds to the JUN45 value, assuming a completely rigid ^{56}Ni core and

$e_\pi = 1.5e$. Clearly, a significant amount of core polarization is present in the odd-A Cu isotopes. Furthermore, there seems to be a discrepancy between theory and experiment for the neutron-deficient Cu isotopes. For ^{59,61}Cu, the core polarization is not reproduced theoretically. This suggests that the ^{56}Ni core is even more soft than assumed in the present calculations. The core polarization at ^{69}Cu is underestimated, as neutron excitations across $N = 40$ are not included in the model space.

Although several TBME were changed between the GXPF1 and GXPF1A interactions, the predicted quadrupole moments are very similar. This is because the changes in proton and neutron contribution to the quadrupole moment cancel each other out. The proton quadrupole moment is dominated by the large negative single-particle contribution of the $p_{3/2}$ orbit, which is reduced in the GXPF1A interaction. On the other hand, the changes in TBME 6.14 and 6.15 in section 6.1.2 reduce the pairing interaction between the $p_{1/2}$-$p_{1/2}$ and the $p_{1/2}$-$f_{5/2}$ neutron orbits, relatively suppressing formation of 0^+ pairs in these orbits. This can enhance the neutron collectivity. In addition, the quadrupole-quadrupole interaction for these orbits is made more attractive (see 6.16), which should promote the formation of broken-pair particle-hole components in the wavefunction.

The g-factors of the odd-A copper isotopes are given in Fig. 6.3. The agreement with experiment is very good for the GXPF1 interaction. The discrepancy at ^{69}Cu is due to excitations across $N = 40$ which are not included in the model space. The GXPF1A interaction however underestimates the g-factor trend at $^{63-67}$Cu. The magnetic moment of the odd-A nuclei is dominated by the single-particle contribution of the proton in the $p_{3/2}$ orbit. As the pairing strength within the $f_{7/2}$ orbit is made less attractive (see Eq. 6.13), the single-particle component of the wavefunction is slightly reduced, leading to a reduction of the magnetic moment. For the neutron $\nu p_{1/2}$ and $\nu f_{5/2}$ orbits, the collectivity is enhanced for GXPF1A. This reduces the positive neutron single-particle contribution and brings the magnetic moment closer to the (smaller) values of the underlying even-even Ni core. This is seen in Fig. 6.3, where the g-factor is less positive than the GXPF1 value from ^{63}Cu, where the $\nu p_{1/2}$ and $\nu f_{5/2}$ orbits start to get filled.

In Fig. 6.4 the energy levels for the odd-A isotopes are shown. The energy levels predicted by the GXPF1A interaction are consistently lower

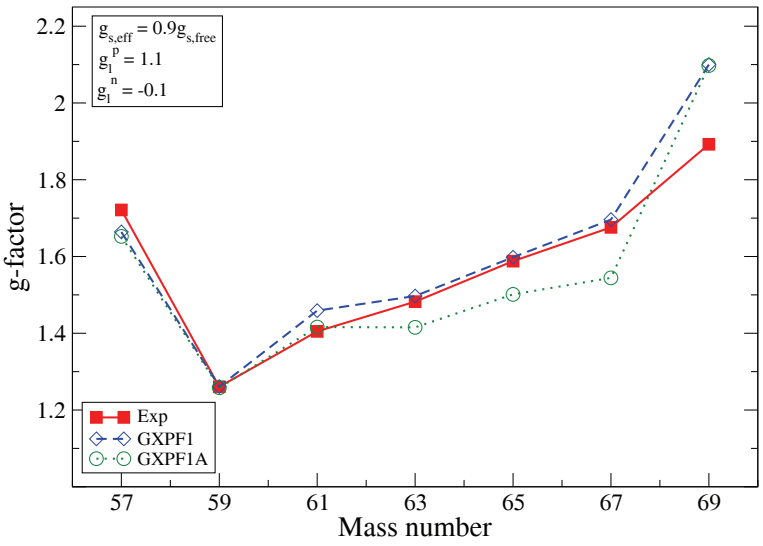

Figure 6.3: The experimental odd-A g-factors (squares) are compared with calculations for the GXPF1(open diamonds) and GXPF1A(open circles). The data point at ^{57}Cu is taken from [45].

than the GXPF1 levels. This is in line with the reduction of the pairing strength within the $f_{7/2}$ orbit for the GXPF1A interaction. Pair scattering into the $p_{3/2}$ orbit is enhanced, making it more favorable for the single proton to excite to the $f_{5/2}$ or the $p_{1/2}$ orbit than with a more rigid ^{56}Ni core. The combination of the g-factor trend with the energy levels for the odd-A isotopes clearly indicates that a change in TBME can be made to achieve better description of experimental data, but the agreement with experiment is not necessarily true for every parameter. In this case, the excitation energies of the $5/2^-$ and the $3/2^-$ states are better described by the GXPF1A interaction, however the g-factor trend clearly shows that there is still a structural problem with the modification of the TBME. This again illustrates the sensitivity of the magnetic moments to the detailed composition of the wavefunction.

The g-factors of the odd-odd copper isotopes are given in Fig. 6.5. Clearly, the structure of the ^{64}Cu and ^{66}Cu nuclei is not correct for the GXPF1A interaction. This is due to incorrect admixture between the 1^+ ground state and a low-lying 1^+ excited state. In Fig. 6.6 a

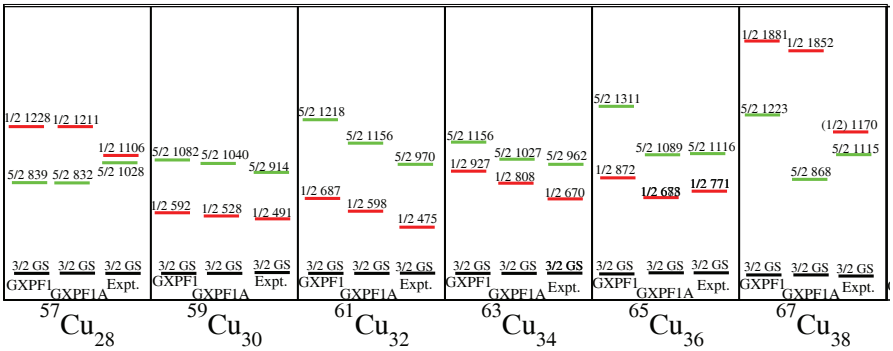

Figure 6.4: The low-lying energy levels for the neutron-deficient odd-A Cu isotopes.

selection of levels and their excitation energy is shown. Overall, the ground state is not always predicted correctly by the theory. The state which is used in the g-factor plot is indicated with a thick line. As in the case of the odd-A copper isotopes, we see that the GXPF1A better reproduces the experimental energy levels, but the g-factor trend reveals that the composition of the wavefunction of the ground state is not correct. The combination of magnetic moments and energy levels again provides different viewpoints to evaluate large-scale shell model calculations.

Finally, the even-A quadrupole moments are given in Fig. 6.7 to probe the core polarization of the neutron-deficient copper nuclei. The sign of the quadrupole moment of ^{64}Cu is reversed for the GXPF1A interaction, again due to incorrect mixing with a low-lying 1^+ state.

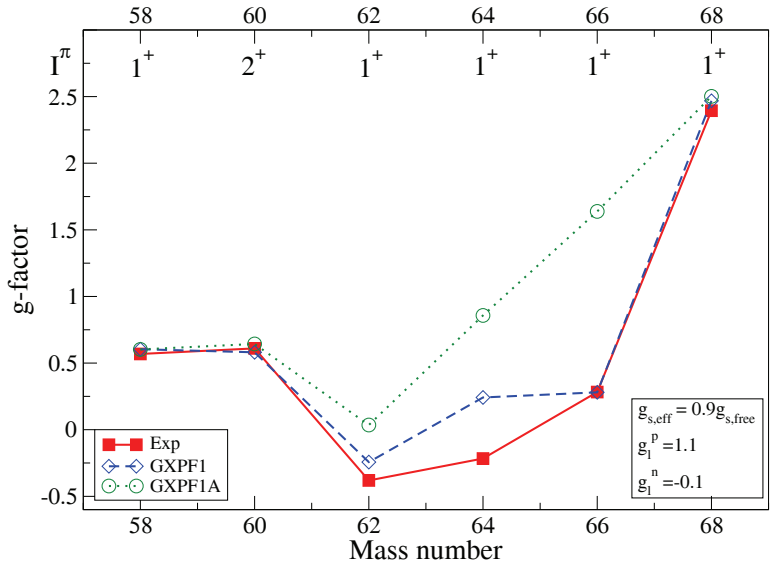

Figure 6.5: The g-factors for the neutron-deficient even-A Cu isotopes. Incorrect mixing between the ground state and a low-lying 1^+ state is the cause of the discrepancy between the GXPF1A calculations and experiment at ^{64}Cu and ^{66}Cu.

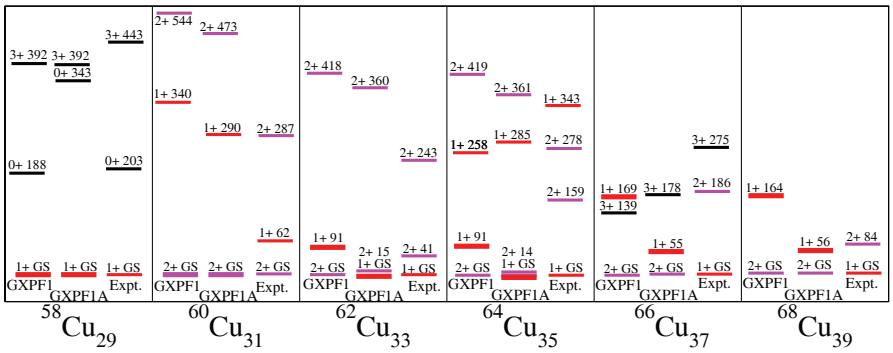

Figure 6.6: The GXPF1A and especially the GXPF1 interaction predicts the wrong ground state for several even-A isotopes. The states used in the g-factor plot are indicated with a thick line.

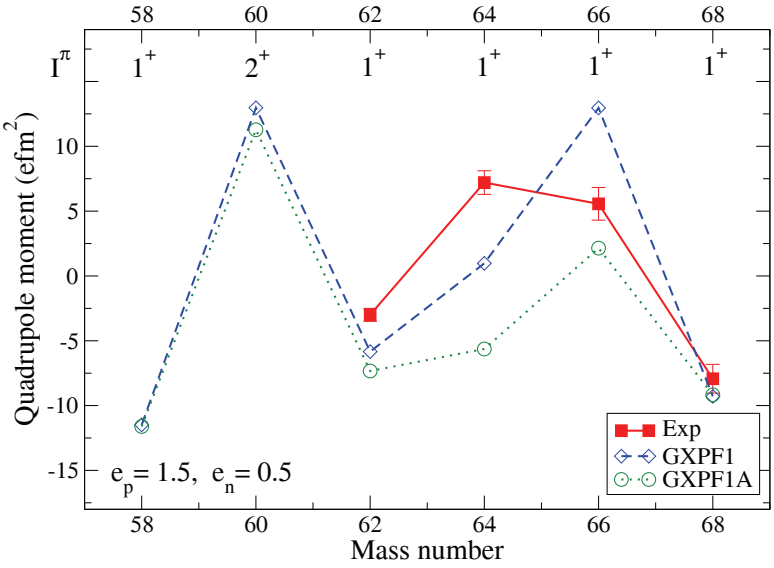

Figure 6.7: The even-A quadrupole moments compared with theory. Again, the deviations for the GXPF1 and GXPF1A interactions are due to incorrect mixing of 1^+ states.

6.4 The Cu isotopes: from isotope shifts to charge radii

In this section, the procedure of extracting differences in mean square charge radii from the measured isotope shifts will be discussed. Two different empirical methods will be followed to calculate the field shift constant, after which an estimation of the specific mass shift can be made. These results will be compared to ab initio Dirac-Fock calculations. In order to calculate the differences in mean square charge radius between the different isotopes, three different contributions have to be calculated (see section 3.6):

$$\delta\nu^{A,A'} = \delta\nu^{A,A'}_{NMS} + \delta\nu^{A,A'}_{SMS} + \delta\nu^{A,A'}_{FS}. \tag{6.18}$$

with the field shift given by equation 3.44.

6.4.1 The normal mass shift

The normal mass shift is determined in a straightforward way by equation 3.40, which yields:

$$\delta\nu^{A,A'}_{NMS} = \frac{A'-A}{AA'}K_{NMS} = \frac{A'-A}{AA'}m_e\nu_A. \tag{6.19}$$

With the transition wavelength $\nu_A = 324.848$ nm [97] the factor K_{NMS} becomes:

$$K_{NMS} = 506.27\text{Ghz} \cdot \text{u}. \tag{6.20}$$

Calculating this expression explicitly for the stable isotope pair ^{63,65}Cu yields:

$$\delta\nu^{63,65}_{NMS} = 247.26\text{MHz} \tag{6.21}$$

The specific mass shift cannot be calculated in an analytical way and will be estimated by determining the other contributions to the isotope shift [70].

6.4.2 The field shift

The field shift constant can be factorized in the following way [73, 74]:

$$F = \frac{\pi a_0^3}{Z}\Delta|\Psi(0)|^2 Z f(Z) \tag{6.22}$$

with a_0 the Bohr radius, $\Delta|\psi(0)|$ the change of non-relativistic electronic probability density at the position of the nucleus, and $f(Z)$ a relativistic correction factor. This factor is given for the stable pair of isotopes ^{63,65}Cu [73]:

$$f(29,^{63,65}\,\mathrm{Cu}) = 1786.78\mathrm{MHz/fm}^2. \tag{6.23}$$

This factor is sligthly isotope dependent [74], however this dependence is negligible compared to other sources of error in determining the field factor. The change in non-relativistic probability density at the position of the nucleus can be expressed as:

$$\Delta|\Psi(0)|^2 = \beta|\Psi(0)|^2 \tag{6.24}$$

where the screening factor β takes into account the change in the screening of inner closed-shell electrons from the nuclear charge by the valence electron as it changes from the ns to the np configuration. This factor has been calculated by non-relativistic Hartree-Fock calculations for different nuclei, but not for Cu [74, 98]. A compilation of elements with a similar atomic structure as the Cu isotopes is given in Table 6.2. The screening ratio is taken as $\beta = 1.12(5)$ for Cu.

Table 6.2: Screening ratios for elements with a similar atomic structure as Cu. $\beta = 1.12(5)$ was adopted for Cu.

Element	β
Ag I	1.13
Cd II	1.09
Ba II	1.12
Cs I	1.13

Two empirical methods exist to calculate the non-relativistic probability density $|\Psi(0)|$ at the position of the nucleus. The first one makes use of the relation of $|\Psi(0)|^2$ with the hyperfine parameter for the S state in alkali-like isotopes[99]:

$$A_S = \frac{8}{3}R_\infty\alpha^2\frac{m_e}{m_p}g_I\pi a_0^3|\Psi(0)|^2 \tag{6.25}$$

with R_∞ the Rydberg constant, g_I the nuclear g-factor, α the fine structure constant.

Using the values $A(^2S_{1/2}) = 5866.915(5)$MHz for 63Cu and $A(^2S_{1/2}) = 6284.504(5)$MHz for ^{65}Cu one gets:

$$|\Psi(0)|^2_{A-factor} = 3.3445 \cdot 10^{31} m^{-3} \quad \text{for } ^{63}\text{Cu} \tag{6.26}$$

$$|\Psi(0)|^2_{A-factor} = 3.3443 \cdot 10^{31} m^{-3} \quad \text{for } ^{65}\text{Cu}. \tag{6.27}$$

$$\tag{6.28}$$

The difference between the isotopes is negligible, so the non-relativistic probability density at the position of the nucleus can be considered as isotope independent.

A second way of determining $\Delta|\Psi(0)|$ is via the so-called Landé-Goudsmit-Fermi-Segré (LGFS) formula, given by:

$$|\Psi(0)|^2 = \frac{Z_i Z_a^2}{\pi a_0^3 n^{*3}} \left(1 - \frac{d\Delta}{dn}\right) F_r(1-\delta)(1-\epsilon) \tag{6.29}$$

where for S states, Z_i and Z_a have to be taken as Z and 1, respectively [100]. $(1-\epsilon)$ is a correction factor to take into account the distribution of the magnetic moment over the nuclear volume [101]. However, the value of ϵ is calculated to be smaller than 10^{-3}, which is negligible compared to other sources of error in this procedure. F_r is a relativistic correction factor and δ a correction accounting for the finite electrostatic volume of the nucleus. The most recent calculation of the factor $F_r(1-\delta)$ yields 1.0824 [102]. Δ is defined as the 'quantum defect', which is related to the principal quantum number n:

$$\Delta = n - n* \tag{6.30}$$

where n^* is a quantity known as the 'effective principal quantum number', given by [100]:

$$n^* = n - \alpha(l) - \frac{\beta(l)}{n^2} \tag{6.31}$$

The parameters $\alpha(l)$ and $\beta(l)$ can be obtained by a fit of the energies of the ns states as a function of quantum number. The resulting fit is given in Fig. 6.8. The values of the parameters α and β were determined to be 2.506(5) and 2.68(8), respectively. This yields $n^* = 1.33(5)$ for the effective principal quantum number.

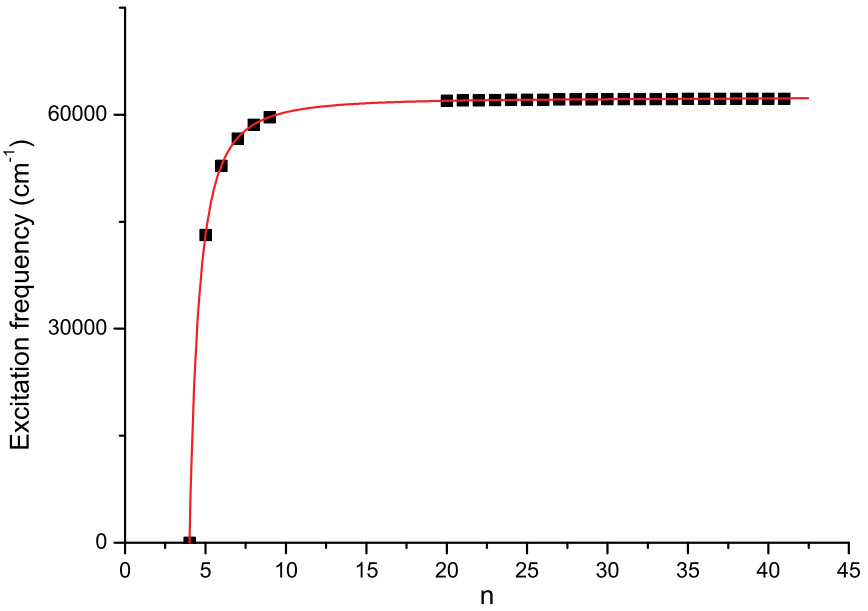

Figure 6.8: A fit of the excitation frequencies as a function of principal quantum number yields the parameters $\alpha(l)$=2.506(5) and $\beta(l)$ = 2.68(8) of equation 6.31.

$$\frac{d\Delta}{dn} = \frac{-2\beta}{n^3} = -0.0838 \tag{6.32}$$

Filling this information in the LGFS formula (6.29) yields:

$$|\Psi(0)|^2_{LGFS} = 3.309 \cdot 10^{31}\ \mathrm{m}^{-3} \tag{6.33}$$

The values of the non-relativistic probability density obtained with the two empirical methods of equations (6.29) and (6.25) differ by 1%. This agreement is very good. The error on the average is usually taken as 10% [100]:

$$|\Psi(0)|^2 = 3.32(33) \cdot 10^{31}\ \mathrm{m}^{-3} \tag{6.34}$$

Using the value of the screening ratio β=1.12(5) obtained from table 6.2 the change in probability density at the position of the nucleus becomes:

$$\Delta\,|\Psi(0)|^2 = 3.73(41) \cdot 10^{31} m^{-3} \tag{6.35}$$

and calculating the field factor with (6.22) yields:

$$F = -952(95)\ \mathrm{MHz/fm}^2 \tag{6.36}$$

For the estimation of the specific mass shift, an evaluation of the mean square charge radius is required. A summary of muonic and elastic scattering (ES) experiments is given in [103]. The ES results are not useable, as the three different experiments are in complete disagreement. The muonic data however can be used to determine the mean square charge radius in a model-dependent way [104, 105]. For the stable copper isotope pair we get:

$$\left\langle r^2 \right\rangle (^{63}\mathrm{Cu}) = 15.117(27)\ \mathrm{fm}^2 \tag{6.37}$$
$$\left\langle r^2 \right\rangle (^{65}\mathrm{Cu}) = 15.272(28)\ \mathrm{fm}^2 \tag{6.38}$$

and the difference in mean square charge radius becomes

$$\delta \left\langle r^2 \right\rangle (^{63-65}\mathrm{Cu}) = 0.16(4)\ \mathrm{fm}^2 \tag{6.39}$$

The field shift between ^{63}Cu and ^{65}Cu can then be calculated as:

$$\delta\nu_{FS}(^{63-65}\mathrm{Cu}) = \mathrm{F}\delta \left\langle \mathrm{r}^2 \right\rangle (^{63-65}\mathrm{Cu}) = -152(53)\ \mathrm{MHz}. \tag{6.40}$$

6.4.3 The specific mass shift

Once the field shift and the normal mass shift are calculated, the specific mass shift can be estimated as well:

$$\delta\nu_{SMS}^{63-65} = \frac{A' - A}{AA'} K_{SMS} = 481(41) \text{ MHz}. \tag{6.41}$$

from which we can deduce that

$$K_{SMS} = 984(83)\text{GHz} \cdot \text{u} \tag{6.42}$$

Note that the specific mass shift is almost twice as large as the normal mass shift, which is at variance with the empirical rule given in expression 3.41. This could be an indication that the 'closed' $3d$ electron shell is far from inactive. However, the value of the specific mass shift is not determined to be as large as in earlier work [106], where the liquid drop model was used to evaluate the difference in mean square charge radius between $^{63-65}$Cu.

Another method to calculate the field factor and the specific mass shift, other than the semi-empirical approaches presented above, is an atomic ab-initio calculation. Dirac-Fock calculations have been carried out using the Ratip program [107]. The comparison between semi-empirical and ab-initio methods is given in Table 6.3. Clearly, there is a large discrepancy between the ab initio calculations and the semi-empirical approach. The specific mass shift is more than a factor of two larger for the semi-empirical approach.

Table 6.3: Field factor and specific mass shift (constant) caclulated semi-empirically and ab initio. Ab initio values [108] were calculated using the Ratip program [107].

	F (Mhz/fm^2)	K_{SMS}(GHz $\cdot$ u)	$\delta\nu_{SMS}^{63-65}$(MHz)
Semi-empirical	-952(95)	+984(83)	+481(41)
Ab initio	-671	+460	+225

6.4.4 Extraction of mean square charge radii

Using the abovementioned results, and the relation:

$$\delta\left\langle r^2\right\rangle(^{65,A}\mathrm{Cu}) = \frac{\delta\nu_{\mathrm{IS}}^{65,\mathrm{A}}}{\mathrm{F}} - \frac{\mathrm{A}-65}{\mathrm{F}\cdot\mathrm{A}\cdot 65}(\mathrm{K_{NMS}}+\mathrm{K_{SMS}}) \tag{6.43}$$

the mean square charge radii can be extracted from the experimental isotope shifts. The results are given in Table 6.4.

Table 6.4: Isotope shifts (IS) and differences in mean square charge radii extracted using the semi-empirical (SE) approach and ab initio calculations (AI).

Isotope	I^π	IS (MHz)	$\delta < r^2 >_{SE}$ (fm^2)	$\delta < r^2 >_{AI}$ (fm^2)
^{58}Cu	1^+	-1975(10)	-0.830(10)	0.270(15)
^{59}Cu	$3/2^-$	-1717(7)	-0.645(7)	0.306(11)
^{60}Cu	2^+	-1415(6)	-0.520(6)	0.262(9)
^{61}Cu	$3/2^-$	-1188(7)	-0.374(5)	0.257(8)
^{62}Cu	1^+	-825(4)	-0.299(4)	0.157(6)
^{63}Cu	$3/2^-$	-576.1(11)	-0.1601(12)	0.1544(17)
^{64}Cu	1^+	-249(2)	-0.114(2)	0.025(3)
^{65}Cu	$3/2^-$			
^{66}Cu	1^+	305(3)	0.046(4)	-0.118(5)
^{67}Cu	$3/2^-$	561(4)	0.131(4)	-0.174(5)
^{68}Cu	1^+	859(4)	0.163(4)	-0.300(6)
^{68}Cu	6^-	813(3)	0.212(3)	-0.231(4)
^{69}Cu	$3/2^-$	1079(2)	0.266(2)	-0.321(3)
^{70}Cu	1^+	1307(8)	0.352(9)	-0.361(13)
^{70}Cu	3^-	1335(8)	0.323(9)	-0.402(13)
^{70}Cu	6^-	1347(2)	0.310(2)	-0.420(4)
^{71}Cu	$3/2^-$	1526(9)	0.437(10)	0.-0.397(14)
^{72}Cu	2^-	1787(4)	0.471(4)	-0.503(6)
^{73}Cu	$3/2^-$	1984(12)	0.563(13)	-0.521(18)
^{74}Cu	2^-	2260(14)	0.563(15)	-0.67(2)
^{75}Cu	$5/2^-$	2484(16)	0.611(17)	-0.74(2)

In Fig. 6.9, the $\delta < r^2 >$ trend is shown for the semi-empricical method. The error on the points corresponds to the experimental error on the isotope shifts, and is smaller than the points. The shades indicate the uncertainty due to the evaluation of the field factor and the specific mass shift. Odd-even staggering is clearly observed. The isomers observed in ^{68,70}Cu have a slightly larger mean square charge radius than

their ground states. The MSCR are compared with the prediction of the droplet model for arbitrary shapes [109]. The overall slope of the charge radii curve is in agreement with what we would expect from the droplet model. Note that the intercept of the droplet model line is quite arbitrary. In this case we fixed the $\langle\beta^2\rangle^{1/2} = 0$ line to the most spherical nucleus in the trend, ^{75}Cu. The comparison with the other droplet model lines indicates significant collectivity in the copper isotope chain. Most nuclei appear as dynamically deformed with $\langle\beta^2\rangle^{1/2} = 0.2$. Note however, that this does not imply that the copper nuclei are deformed in a rigid way ($\beta \approx 0.2$).

In Fig. 6.9 (b), the $\delta < r^2 >$ trend is shown with the field factor and specific mass shift extracted from ab initio calculations. No shades are applied, as there are no error bars given on the extracted values (see Table 6.3). Clearly, the volume contribution is opposite to what would be expected from the droplet model. Therefore the semi-empirical approach is considered to be more reliable at the present time.

In Fig. 6.10, the $\delta < r^2 >$ trend for the odd-A Cu isotopes is shown. Clearly, the increase in MSCR is less pronounced at ^{75}Cu, which indicates that this nucleus shows less collectivity. This is in agreement with the B(E2) measurements, which concluded that the $5/2^-$ state in ^{71,73}Cu has a single-particle like structure as well [5]. However, a spectacular increase in collectivity beyond $N = 40$ cannot be observed from the MSCR trend. The MSCR curve seems to be composed of two parabola, with a slight minimum around $N = 40$, which can be considered as a weak subshell effect.

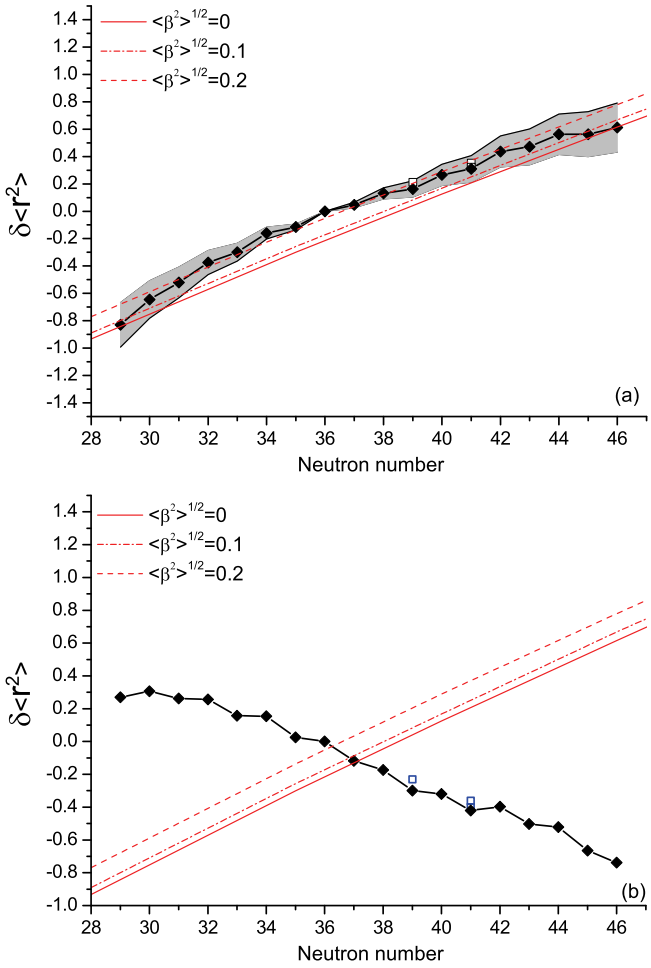

Figure 6.9: (a) The MSCR of the Cu isotopes (black diamonds) determined with the semi-empirical approach are compared with the droplet model predictions for different deformation parameters (red lines). The isomers observed in ^{68,70}Cu (open squares) have a slightly larger mean square charge radius than their ground states. The grey shades correspond to the error on the slope due to the estimation of the field factor and specific mass shift. (b) The MSCR with the field factor and specific mass shift determined from ab initio calculation [107].

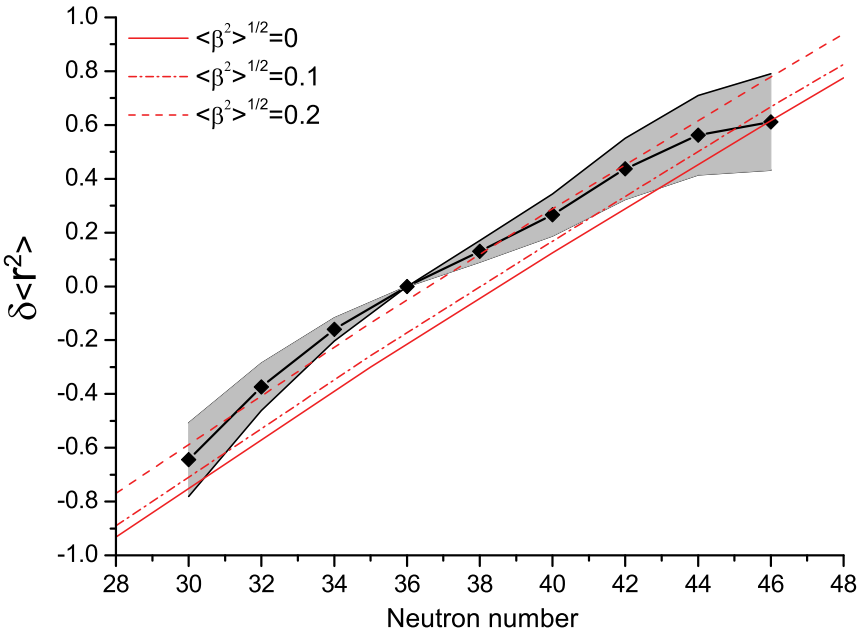

Figure 6.10: The differences in MSCR for the odd-A Cu isotopes, extracted using the semi-empirical approach, are compared with the droplet model prediction.

Chapter 7

Conclusions

This PhD thesis discusses the fascinating features of nuclear structure in the region around the $Z = 28$ shell closure. The copper isotopes, which have only one proton outside the semi-magic Ni nuclei, are probed from neutron number 29 to 46. The nuclear spins, magnetic moments, quadrupole moments, and differences in mean square charge radii were measured using the technique of collinear laser spectroscopy. The results reveal crucial information on the evolution of single-particle energies and provide stringent tests for recent large-scale shell model theories.

The well known technique of collinear laser spectroscopy and its analysis procedure is described in this thesis. The latest technical development, the installation of the ISCOOL buncher, has allowed measurements to be extended toward more exotic isotopes. The nuclear spin of $^{58-75}$Cu is determined in a model-independent way. The ground-state spin inversion for the odd-A Cu isotopes from $3/2^-$ to $5/2^-$ is firmly established to occur at ^{75}Cu. This result presents a breakthrough for effective shell-model interactions, as they rely on experimental data to determine the evolution of effective single-particle energies. Likewise, the newly assigned ground-state spin of 2^- for ^{72,74}Cu provides a new challenge for shell model calculations. Also upcoming experimental studies on higher excited levels of copper isotopes benefit from the ground-state spin assignments. Magnetic moments are very sensitive to the exact composition of the wavefunction, while quadrupole moments are well suited parameters to probe collectivity. For both magnetic and quadrupole moments, a stabilizing effect of the $N = 40$ subshell gap is found,

which is related to the parity change between the pf and $g_{9/2}$ orbits. A comparison of the measured moments with four effective shell model theories is made: jj44b and JUN45, which are active in the $f_{5/2}pg_{9/2}$ model space, and GXPF1 and GXPF1A, active in the full pf shell. The magnetic moment trend is not correctly reproduced by the interactions employing a ^{56}Ni core, stressing the importance of excitations across the $N, Z = 28$ shell gaps. For neutron-deficient Cu isotopes, the GXPF1 interaction reproduces the magnetic moments very well, while its modification GXPF1A underestimates the magnetic moments. The ground-state quadrupole moments do not reveal any indication of increased collectivity beyond $N = 40$. The mean square charge radii show a significant collectivity in the entire copper isotope chain with only a small structural effect at $N = 40$. The core polarization is clearly underestimated by the interactions employing a ^{56}Ni core, indicating the softness of this core.

This work not only resolves pending questions in the field of nuclear physics, it also motivates further investigations in this region. More data can be recorded for other isotopes to improve the input for effective interactions. Technical improvements could provide crucial information in the region around $Z = 28$ and $N = 50$, which is currently out of reach due to the high neutron-to-proton ratio. On the theoretical side, the model space of the theories discussed in this work can be expanded in order to describe parameters like moments, energies and transition rates in the full $pfg_{9/2}d_{5/2}$ space. The ultimate goal, the development of a theory which has a high descriptive and predictive power in the entire nuclear chart, is challenged by the enormous complexity of the nuclear many-body problem. However, more and more of the peculiar behavior of nuclei is currently unraveled, and this work, as many other contributions in the field of nuclear physics, brings us closer to that goal.

Chapter 8

Appendix

In this section, a hyperfine spectrum of the $^2S_{1/2}$-$^2P_{3/2}$ transition is shown for every measured copper isotope in this work. The fit is performed as explained in section 5. The frequency scale in the X-axis is given relative to the center of gravity of ^{65}Cu.

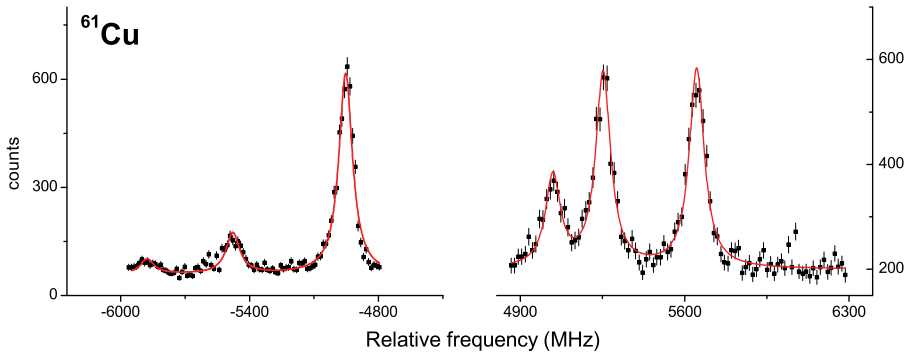

Figure 8.1: Hyperfine spectrum of the $3/2^-$ ground state of ^{61}Cu.

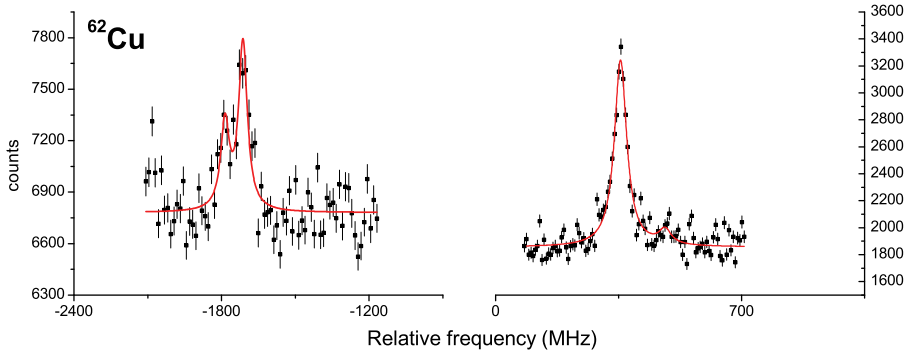

Figure 8.2: Hyperfine spectrum of the 1^+ ground state of ^{62}Cu.

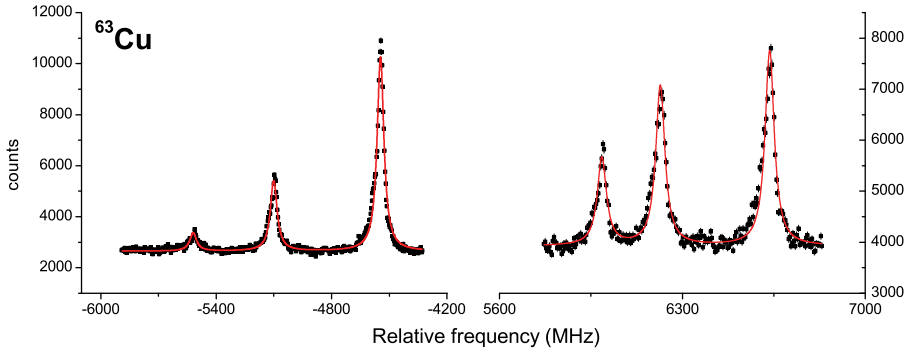

Figure 8.3: Hyperfine spectrum of the $3/2^-$ ground state of ^{63}Cu.

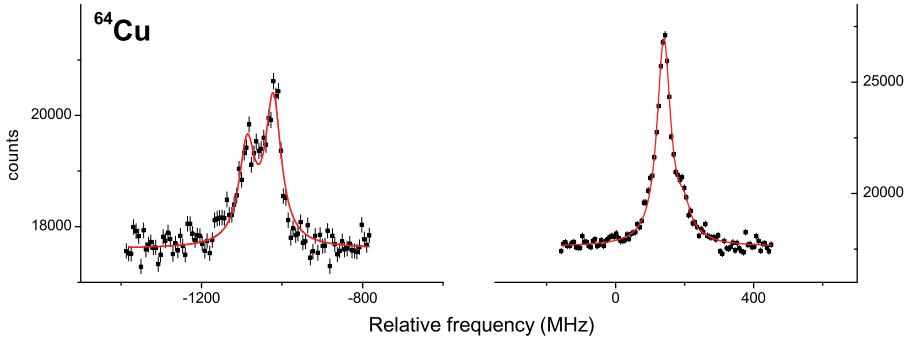

Figure 8.4: Hyperfine spectrum of the 1^+ ground state of ^{64}Cu.

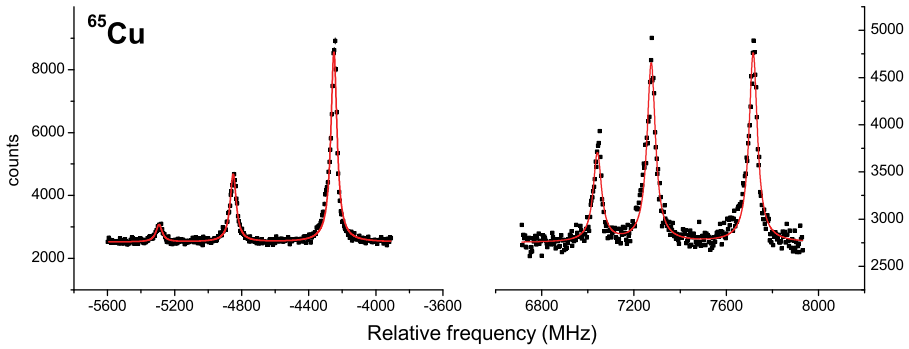

Figure 8.5: Hyperfine spectrum of the $3/2^-$ ground state of ^{65}Cu.

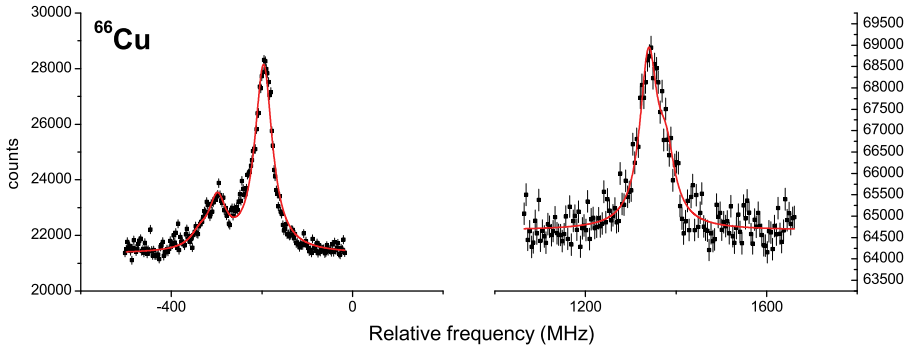

Figure 8.6: Hyperfine spectrum of the 1^+ ground state of ^{66}Cu.

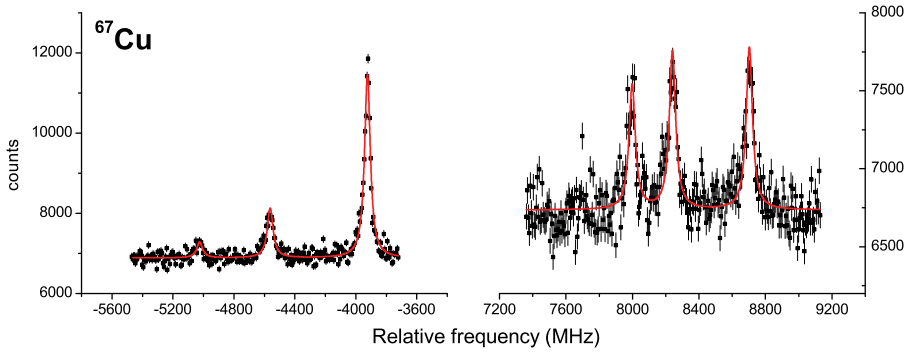

Figure 8.7: Hyperfine spectrum of the $3/2^-$ ground state of ^{67}Cu.

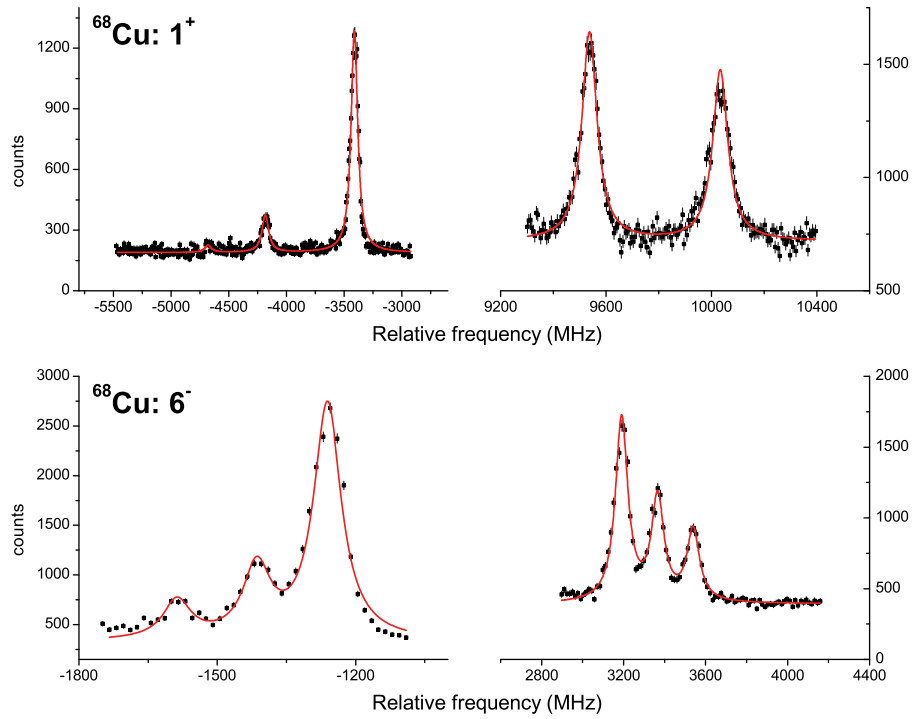

Figure 8.8: Hyperfine spectra of ^{68}Cu for the 1+ ground state and the 6^- excited state.

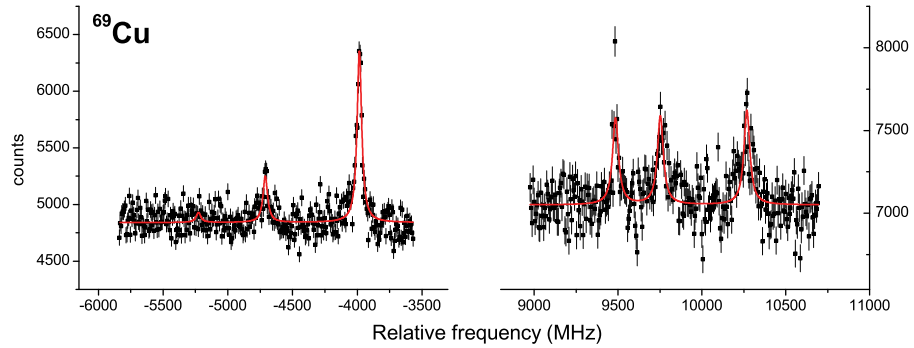

Figure 8.9: Hyperfine spectrum of the $3/2^-$ ground state of ^{69}Cu.

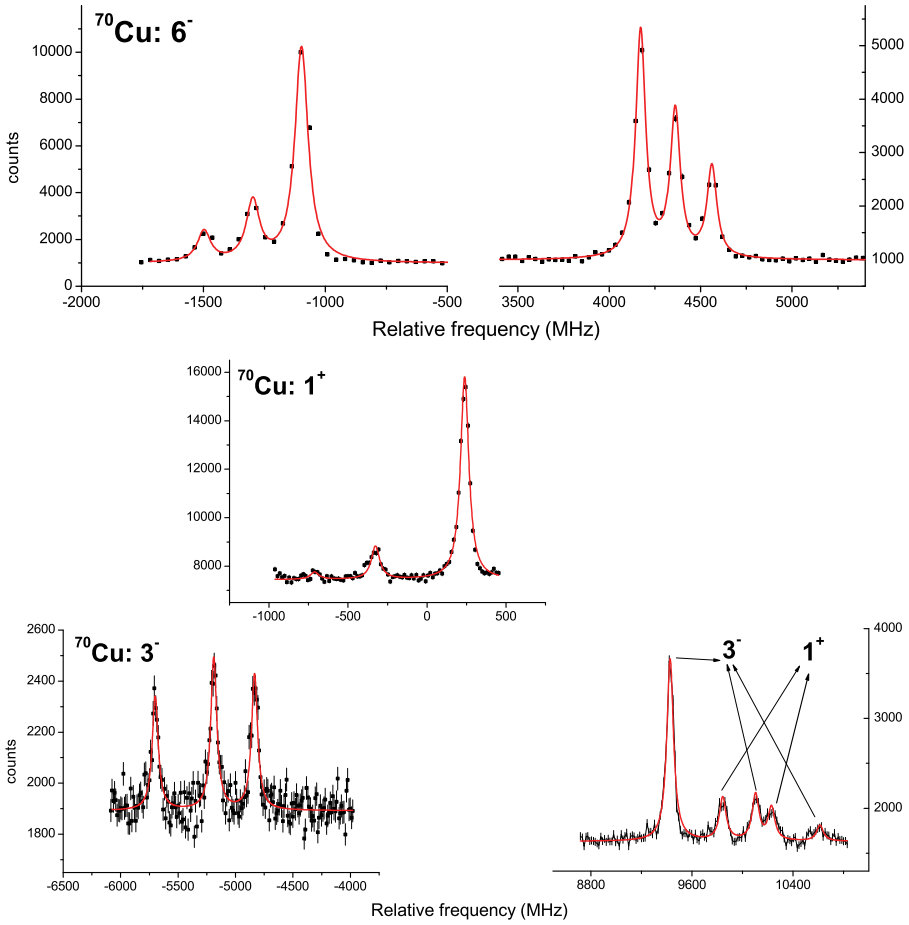

Figure 8.10: Hyperfine spectrum of ^{70}Cu for the 6^- ground state, and a simultaneous fit performed for the 1^+ and 3^- excited states.

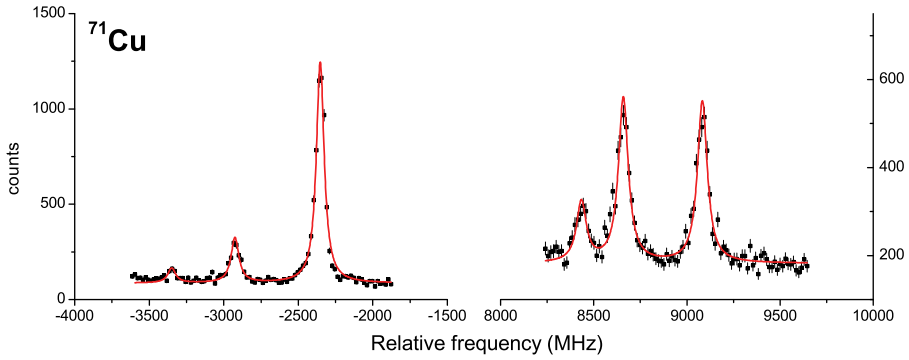

Figure 8.11: Hyperfine spectrum of the $3/2^-$ ground state of ^{71}Cu.

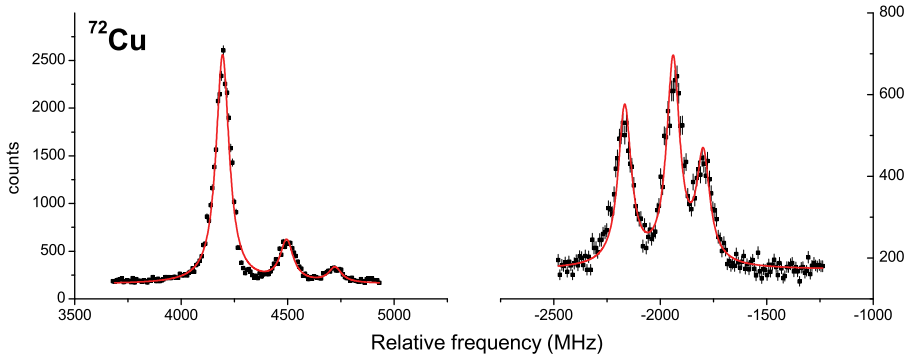

Figure 8.12: Hyperfine spectrum of the 2^- ground state of ^{72}Cu.

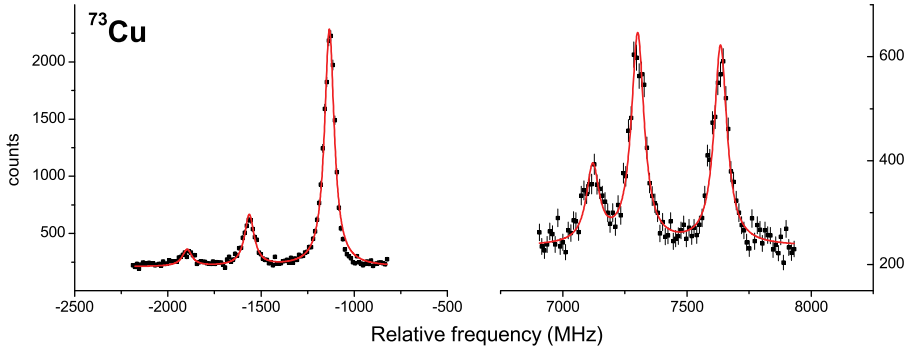

Figure 8.13: Hyperfine spectrum of the $3/2^-$ ground state of ^{73}Cu.

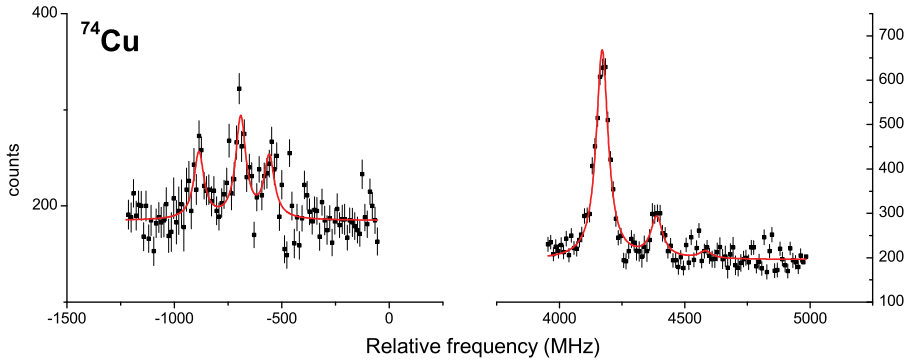

Figure 8.14: Hyperfine spectrum of the 2^- ground state of ^{74}Cu.

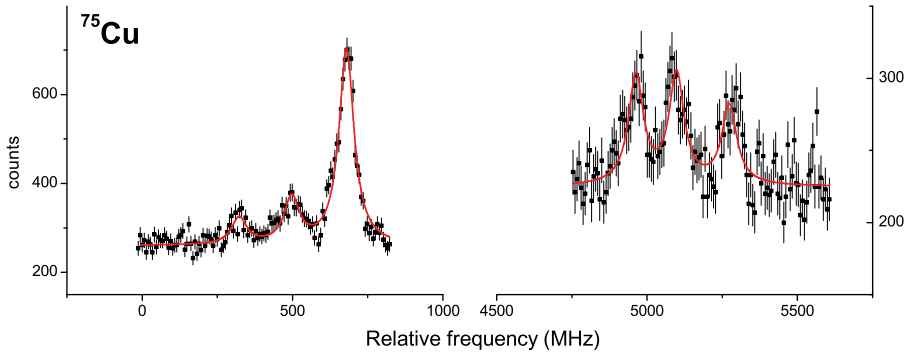

Figure 8.15: Hyperfine spectrum of the $5/2^-$ ground state of ^{75}Cu.

Bibliography

[1] T. Otsuka *et al.*, Phys. Rev. Lett. **95**, 232502 (2005).

[2] S. Franchoo *et al.*, Phys. Rev. Lett. **81**, 3100 (1998).

[3] S. Franchoo *et al.*, Phys. Rev. C **64**, 054308 (2001).

[4] A. M. Oros-Peusquens and P. F. Mantica, Nucl. Phys. A **669**, 81 (1998).

[5] I. Stefanescu *et al.*, Phys. Rev. Lett. **100**, 112502 (2008).

[6] T. Otsuka, R. Fujimoto, Y. Utsuno, B.A. Brown, M. Honma and T. Mizusaki, Phys. Rev. Lett. **87**, 082502 (2001).

[7] T. Otsuka *et al.*, Phys. Rev. Lett. **104**, 012501 (2010).

[8] M. Honma *et al.*, Phys. Rev. C **80**, 064323 (2009).

[9] N. A. Smirnova *et al.*, Phys. Rev. C **69**, 044306 (2004).

[10] A. F. Lisetskiy *et al.*, Phys. Rev. C **70**, 044314 (2004).

[11] A. F. Lisetskiy *et al.*, Eur. Phys. J. A **25**, 95 (2005).

[12] K.T. Flanagan *et al.*, Phys. Rev. Lett. **103**, 142501 (2009).

[13] E. N. S. Data, http://www.nndc.bnl.gov/.

[14] S. Raman *et al.*, At. Data Nucl. Data Tables **78**, 1 (2001).

[15] P. Adrich *et al.*, Phys. Rev. C **77**, 054306 (2008).

[16] J. Ljungvall *et al.*, Phys. Rev. C **81**, 061301 (2010).

[17] J. Van de Walle *et al.*, Phys. Rev. C **79**, 014309 (2009).

[18] E. Padilla-Rodal *et al.*, Phys. Rev. Lett. **94**, 122501 (2005).

[19] O. Perru *et al.*, Phys. Rev. Lett. **96**, 232501 (2006).

[20] O. Sorlin *et al.*, Phys. Rev. Lett. **88**, 092501 (2002).

[21] W. Rother *et al.*, Phys. Rev. Lett. **106**, 022502 (2011).

[22] C. Guènaut *et al.*, Phys. Rev. C **75**, 044303 (2007).

[23] S. Rahaman *et al.*, Eur. Phys. J. A **34**, 5 (2007).

[24] R. Ferrer *et al.*, Phys. Rev. C **81**, 044318 (2010).

[25] M. Bernas *et al.*, Phys. Lett. **113B**, 279 (1982).

[26] R. Grzywacz *et al.*, Phys. Rev. Lett. **81**, 766 (1998).

[27] J. Van Roosbroeck *et al.*, Phys. Rev. Lett. **92**, 112501 (2004).

[28] J. Van Roosbroeck *et al.*, Phys. Rev. C **71**, 054307 (2005).

[29] K. Langanke *et al.*, Phys. Rev. C **67**, 044314 (2003).

[30] M. Hannawald *et al.*, Phys. Rev. Lett. **82**, 1391 (1999).

[31] D. Pauwels *et al.*, Phys. Rev. C **82 pages** = (2010).

[32] K. Kaneko *et al.*, Phys. Rev. C **74**, 024321 (2006).

[33] R. Broda *et al.*, Phys. Rev. Lett. **75**, 868 (1995).

[34] W.F. Mueller *et al.*, Phys. Rev. Lett. **83**, 3613 (1999).

[35] J. Van Roosbroeck *et al.*, Phys. Rev. C **69**, 034313 (2004).

[36] D. Pauwels *et al.*, Phys. Rev. C **78**, 041307 (2008).

[37] A. Gade *et al.*, Phys. Rev. C **81**, 051304 (2010).

[38] T. Ishii *et al.*, Phys. Rev. Lett. **84**, 39 (2000).

[39] D. Pauwels *et al.*, Phys. Rev. C **79**, 044309 (2009).

[40] M. Hasegawa *et al.*, Nucl. Phys. A **789**, 46 (2007).

[41] I. Stefanescu *et al.*, Phys. Rev. Lett. **98**, 122701 (2007).

[42] N. Bree *et al.*, Phys. Rev. C **78**, 047301 (2008).

[43] D. Mücher *et al.*, Phys. Rev. C **79**, 054310 (2009).

[44] O. Kenn *et al.*, Phys. Rev. C **65**, 034308 (2002).

[45] T.E. Cocolios *et al.*, Phys. Rev. Lett. **103**, 102501 (2009).

[46] J. Rikovska *et al.*, Phys. Rev. Lett. **85**, 1392 (2000).

[47] J. Rikovska and N. J. Stone, Hyp. Interact. **129**, 131 (2000).

[48] N.J. Stone, Phys. Rev. C **77**, 014315 (2008).

[49] T. E. Cocolios *et al.*, Phys. Rev. C **81**, 014314 (2010).

[50] B. Cheal *et al.*, Phys. Rev. Lett. **104**, 252502 (2010).

[51] G. Kraus *et al.*, Phys. Rev. Lett. **73**, 1773 (1994).

[52] O. Sorlin *et al.*, Prog. Part. Nucl. Phys. **61**, 602 (2008).

[53] D. Rudolph *et al.*, Phys. Rev. Lett. **82**, 3763 (1999).

[54] O. Kenn *et al.*, Phys. Rev. C **63**, 064306 (2001).

[55] T. Otsuka *et al.*, Phys. Rev. Lett. **81**, 1588 (1998).

[56] J.S. Berryman *et al.*, Phys. Rev. C **79**, 064305 (2009).

[57] A.F. Lisetskiy *et al.*, Phys. Rev. C **68**, 034316 (2003).

[58] V.V. Golovko *et al.*, Phys. Rev. C **70**, 014312 (2004).

[59] M. Honma *et al.*, Phys. Rev. C **65**, 061301(R) (2002).

[60] M. Honma *et al.*, Phys. Rev. C **69**, 034355 (2004).

[61] J. Hakala *et al.*, Phys. Rev. Lett. **101**, 052502 (2008).

[62] C. Mazzocchi *et al.*, Phys. Lett. B **622**, 45 (2005).

[63] O. Sorlin *et al.*, Eur. Phys. J. A **16**, 55 (2003).

[64] N. Hoteling *et al.*, Phys. Rev. C **82**, 044305 (2010).

[65] S.M. Lenzi *et al.*, Phys. Rev. C **82**, 054301 (2010).

[66] K. S. Krane, *Introductory nuclear physics* (John Wiley and Sons, 1988).

[67] G. Fricke *et al.*, At. Datat Nucl. Data Tables **60**, 177 (1995).

[68] B. Castel and I.S. Towner, *Modern Theories of Nuclear Moments* (Oxford, 1990).

[69] G. Neyens, Rep. Prog. Phys. **66**, 633 (2003).

[70] I.I. Sobel'man, *Introduction to the Theory of Atomic Spectra* (Pergamon Press, 1972).

[71] S. Cottenier and M. Rots, *Hyperfine Interactions and their Applications in Nuclear Condensed Matter Physics: a Microscopic Introduction* (unpublished lecture notes Katholieke Universiteit Leuven, 2005).

[72] W.H. King, *Isotope Shifts in Atomic Spectra* (Plenum Press (New York), 1984).

[73] P. Aufmuth, K. Heilig and A. Steudel, At. Datat Nucl. Data Tables **37**, 455 (1987).

[74] K. Heilig and A. Steudel, At. Datat Nucl. Data Tables **14**, 613 (1974).

[75] E.C. Seltzer, Phys. Rev. **188**, 1916 (1969).

[76] S.A. Blundell *et al.*, J. Phys. B: At. Mol. Phys. **20**, 3663 (1987).

[77] U. Köster *et al.*, Nucl. Instr. Meth. B **160**, 528 (2000).

[78] H. Franberg *et al.*, Nucl. Inst. Meth. B **266**, 4502 (2008).

[79] E. Mané *et al.*, Eur. Phys. J. A. **42**, 503 (2009).

[80] A. Nieminen *et al.*, Nucl. Instrum. Methods A **469**, 244 (2001).

[81] A. Nieminen *et al.*, Phys. Rev. Lett. **88**, 094801 (2002).

[82] E. Mané, PhD in Physics, School of Physics and Astronomy, University of Manchester (2009), unpublished.

[83] A. Krieger *et al.*, NIM A (2010), submitted.

[84] Chr. Geppert, private communication.

[85] G.Audi *et al.*, Nucl. Phys. A **729**, 337 (2003).

[86] Y. Ting and H. Lew, Phys. Rev. **105**, 581 (1957).

[87] J. Ney, Z. Phys. **196**, 53 (1966).

[88] P.R. Locher, Phys. Rev. B **10**, 801 (1974).

[89] G.F. Bertsch, *The Practitioner's Shell Model* (North-Holland, 1972).

[90] R. Casten, *Nuclear Structure from a Simple Perspective* (Oxford University Press, 1990).

[91] K. Heyde, *The Nuclear Shell Model* (Springer-Verlag, 1990).

[92] M. Hjorth-Jensen *et al.*, Phys. Rep. **261**, 125 (1995).

[93] M. Honma *et al.*, Nucl. Phys. A **704**, 134c (2002).

[94] S.N. Liddick *et al.*, Phys. Rev. Lett **92**, 072502 (2004).

[95] M. Honma *et al.*, Eur. Phys. J. A **25**, 499 (2005).

[96] A. Brown and A. F. Lisetskiy, private communication.

[97] Yu. Ralchenko, A.E. Kramida, J. Reader, and NIST ASD Team, NIST Atomic Spectra Database **4.0.1** (2010).

[98] U. Dinger *et al.*, Nucl. Phys. A **503**, 331 (1989).

[99] H. Kopfermann, *Nuclear Moments* (Academic Press INC, 1958).

[100] H.G. Kuhn, *Atomic Spectra* (Longmans, 1969).

[101] A. Bohr and V.F. Weisskopf, Physical Review **77**, 94 (1950).

[102] S.A. Blundell and C.W.P. Palmer, J. Phys. B: At. Mol. Opt. Phys **21**, 3809 (1988).

[103] G. Fricke *et al.*, At. Nucl. Data Tables **88**, 1 (2004).

[104] E.B. Shera *et al.*, Phys. Rev. C **14**, 731 (1976).

[105] H.D. Wohlfahrt *et al.*, Phys. Rev. C **22**, 264 (1980).

[106] S. Gheysen *et al.*, Phys. Rev. C **69**, 064310 (2004).

[107] S. Fritzsche, C. Z. Dong, F. Koike, Hyp. interact. **196**, 25 (2010).

[108] S. Fritzsche, private communication.

[109] W.D. Myers and W.J. Swiatecki, Annals of Physics **84**, 186 (1974).